Robin Rajamäki

Vacuum arc localization in CLIC prototype radio frequency accelerating structures

School of Electrical Engineering

Thesis submitted for examination for the degree of Master of Science in Technology.

Helsinki 14.03.2016

Thesis supervisor:

Prof. Visa Koivunen

Thesis advisor:

PhD. Walter Wuensch

Aalto University
School of Electrical
Engineering

AALTO UNIVERSITY
SCHOOL OF ELECTRICAL ENGINEERING

ABSTRACT OF THE
MASTER'S THESIS

Author: Robin Rajamäki

Title: Vacuum arc localization in CLIC prototype radio frequency accelerating structures

Date: 14.03.2016 Language: English Number of pages: 9+72

Department of Signal Processing and Acoustics

Professorship: Signal Processing

Supervisor: Prof. Visa Koivunen

Advisor: PhD. Walter Wuensch

A future linear collider capable of reaching TeV collision energies should support accelerating gradients beyond 100 MV/m. At such high fields, the occurrence of vacuum arcs have to be mitigated through conditioning, during which an accelerating structure's resilience against breakdowns is slowly increased through repeated radio frequency pulsing. Conditioning is very time and resource consuming, which is why developing more efficient procedures is desirable. At CERN, conditioning related research is conducted at the CLIC high-power X-band test stands.

Breakdown localization is an important diagnostic tool of accelerating structure tests. Abnormal position distributions highlight issues in structure design, manufacturing or operation and may consequently help improve these processes. Additionally, positioning can provide insight into the physics of vacuum arcs.

In this work, two established positioning methods based on the time-difference-of-arrival of radio frequency waves are extended. The first method is based on signal edge detection and the second on cross-correlation. The methods are parametrized and a bias model for the edge method is developed. The localization precision of the methods is also quantified. Under certain conditions, the correlation method is demonstrated to achieve a precision of less than one accelerating cell.

The methods are applied to data collected from four CLIC prototype structures: three constant gradient accelerating structures, the T24, T24 open and TD26CC, and one constant impedance deflecting structure, the CLIC Crab Cavity. The TD26CC and Crab Cavity operated as expected, whereas the T24 and T24 open developed hot cells close to the RF input. The T24 open continued conditioning despite the hot cell.

Furthermore, evidence of breakdown migration was found when comparing the two positioning methods. It was also discovered that consecutive breakdowns occurring close to each other in time also occur close to each other in space.

Keywords: Electrical breakdown, positioning, time-difference-of-arrival, radio frequency, linear accelerator, hot cell, cross-correlation

AALTO-YLIOPISTO
SÄHKÖTEKNIIKAN KORKEAKOULU

DIPLOMITYÖN
TIIVISTELMÄ

Tekijä: Robin Rajamäki

Työn nimi: Sähköisten tyhjiöläpilyöntien paikannus CLIC-prototyyppiradiotaajuuskiihdytinrakenteissa

Päivämäärä: 14.03.2016 Kieli: Englanti Sivumäärä: 9+72

Signaalinkäsittelyn ja akustiikan laitos

Professuuri: Signaalinkäsittely

Työn valvoja: Prof. Visa Koivunen

Työn ohjaaja: FT Walter Wuensch

Jotta TeV törmäysenergia voitaisiin saavuttaa tulevaisuuden lineaarikiihdyttimessä, on kiihdyttävän sähkökentän voimakkuuden oltava noin 100 MV/m. Näin suurilla kentänvoimakkuuksilla kiihdyttimen normaalia toimintaa haittaavien sähköisten tyhjiöläpilyöntien esiintymistodennäköisyyttä voidaan pienentää prosessilla, jossa kiihdytinrakenne altistetaan toistuvalle radiotaajuuspulssitukselle. Prosessi on kuitenkin hidas ja kallis, minkä vuoksi sitä halutaan tehostaa. Muun muassa näitä tehostamismenetelmiä tutkitaan CERNin CLIC-kiihdytinrakenteiden suurtehomittauksissa.

Läpilyöntien paikantaminen on tärkeä kiihdytinrakenteiden diagnostiikkatyökalu. Epätavallinen paikkajakauma auttaa havaitsemaan ongelmia suunnittelu-, valmistus- tai mittausprosessissa. Paikannus edesauttaa myös läpilyöntien fysiikkan ymmärtämistä.

Tässä työssä tarkastellaan kahta vakiintunutta, radioaaltojen aikaviive-eroon perustuvaa paikannusmenetelmää. Ensimmäinen menetelmä perustuu signaalireunojen havaitsemiseen ja toinen ristikorrelaatioon. Metodeja laajennetaan parametrisoimalla molemmat menetelmät ja johtamalla lauseke reunamenetelmän estimointiharhalle. Lisäksi menetelmien tarkkuus määritellään. Korrelaatiomenetelmän osoitetaan tietyillä ehdoilla yltävän alle yhden kiihdytinsolun resoluutioon.

Läpilyöntejä paikannettiin neljässä eri CLIC-prototyyppikiihdytinrakenteessa: T24:ssä, T24 open:ssa, TD26CC:ssä ja CLIC Crab Cavity:ssä. Läpilyöntien paikkajakaumat olivat odotetunlaiset TD26CC:ssä ja CLIC Crab Cavity:ssä. T24:ssä ja T24 open:ssa läpilyönnit kasaantuivat rakenteiden etuosiin. Läpilyöntitodennäköisyys T24 open:ssa laski tästä huolimatta tasaisesti.

Vaeltavista läpilyönneistä löydettiin todisteita, kun paikannusmenetelmiä vertailtiin. Peräkkäisten läpilyöntien saapumisaikojen ja esiintymispaikkojen välillä havaittiin myös selkeä korrelaatio.

Avainsanat: Sähköinen läpilyönti, tyhjiö, paikannus, aikaviive-ero, radiotaajuus, lineaarikiihdytin, ristikorrelaatio

AALTO-UNIVERSITETET
HÖGSKOLAN FÖR ELEKTROTEKNIK

SAMMANDRAG AV
DIPLOMARBETET

Författare: Robin Rajamäki

Titel: Lokalisering av elektriska vakuumgenomslag i radiofrekvens accelererande strukturprototyper för CLIC

Datum: 14.03.2016 Språk: Engelska Sidantal: 9+72

Institutionen för signalbehandling och akustik

Professur: Signalbehandling

Övervakare: Prof. Visa Koivunen

Handledare: Fil.dr Walter Wuensch

För att en framtida linjärkolliderare kunde nå kollisionsenergier på TeV, bör den accelererande gradienten vara omkring 100 MV/m. Förekomstsannolikheten av elektriska genomslag i vakuum vid dessa höga fältstyrkor kan minskas genom att utsätta de accelererande strukturerna för radiofrekevenspulser upprepade gånger. Denna process är dock långsam och dyr, vilket gör utvecklingen av effektivare metoder lockande. Bland annat dessa alternativa metoder undersöks i högeffektmätningar av CLIC-acceleratorstrukturer vid CERN.

Lokaliseringen av genomslag är ett viktigt diagnostikverktyg i testningen av acceleratorstrukturer. En oförväntad lokationsdistribution hjälper indentifiera problem i design, tillverknings eller testningsprocesserna. Lokalisering bidrar också till en ökad förståelse av den grundläggande fysiken bakom genomslag i vakuum.

I detta arbete granskas två etablerade lokaliseringsmetoder, som använder sig av tidsfördöjningsskillnaden mellan radiovågor. Den första metoden grundar sig på detektionen av signalkanter, medan den andra baserar sig på korskorrelation. Metoderna utvidgas genom att parametrisera dem och härleda ett uttryck för det systematiska felet i kantmetoden. Ytterligare utvärderas precisionen av metoderna. Korrelationsmetoden demonstreras under vissa förutsättningar uppnå en resolution på under en accelererande cell.

Genomslag lokaliserades i fyra olika CLIC-prototyp accelererande strukturer: T24, T24 open, TD26CC och CLIC Crab Cavity. Positionsdistributionerna hade den förväntade formen i TD26CC och CLIC Crab Cavity. I T24 och T24 open ackumulerades genomslagen i början på strukturerna. Trots detta sjönk genomslagsfrekvensen i T24 open.

Det hittades bevis på migrerande genomslag, då lokaliseringsmetoderna jämfördes. Dessutom observerades det en tydlig korrelation mellan ankomsttiden och förekomstplatsen av påföljande genomslag.

Nyckelord: Elektrisk genomslag, vakuum, lokalisering, tidsfördröjningsskillnad, radiofrekvens, linjäraccelerator, korskorrelation

Preface

I would especially like to thank Wilfrid Farabolini and Alberto Degiovanni, whose work this thesis is a continuation to. Additional thanks go to my supervisor at CERN, Walter Wuensch and my professor at Aalto university, Visa Koivunen. Also, many thanks to Ben Woolley, Jorge Giner Navarro, Luis Navarro, Frank Tecker, Theodoros Argyropoulos, Anastasiya Solodko, Enrique Rodriguez Castro, Anders Korsbäck, Hao Zha, Aleksej Grudiev and Igor Syrachev for their help and many suggestions. Lastly, I would like to collectively thank all of my colleagues for making my stay at CERN so enjoyable!

Geneva, 19.02.2016

Robin Rajamäki

Contents

Abstract ii

Abstract (in Finnish) iii

Abstract (in Swedish) iv

Preface v

Contents vi

Symbols and abbreviations viii

1 Introduction 1
- 1.1 Background . . . 1
- 1.2 Scope and outline of thesis . . . 1
- 1.3 Goals and contributions of thesis . . . 2
- 1.4 Notation . . . 3

2 Relevant signal processing concepts 4
- 2.1 Statistical signal processing . . . 4
- 2.2 Localization . . . 5
- 2.3 Cross-correlation . . . 6

3 Radio frequency linear accelerators 9
- 3.1 Electromagnetic waves . . . 9
- 3.2 Waveguides and cavities . . . 10
- 3.3 Phase and group velocity . . . 12
- 3.4 Periodic accelerating structures . . . 13
- 3.5 Vacuum arcs . . . 15

4 Experimental setup 17
- 4.1 High-power test stands . . . 17
- 4.2 Structures under test . . . 19
  - 4.2.1 T24 . . . 19
  - 4.2.2 T24 open . . . 19
  - 4.2.3 TD26CC . . . 20
  - 4.2.4 CLIC Crab Cavity . . . 20

5 Methods of vacuum arc localization 22
- 5.1 Overview of existing localization methods . . . 22
- 5.2 RF power and phase methods . . . 23
  - 5.2.1 Edge method . . . 24
  - 5.2.2 Correlation method . . . 26
  - 5.2.3 Phase . . . 27
- 5.3 Pre-processing . . . 29

5.3.1 Discarding non-breakdown events . . . 29
5.3.2 Filtering interfering reflections . . . 32
5.3.3 Upsampling . . . 32
5.4 Post-processing . . . 32
5.4.1 Discarding uncertain estimates . . . 33
5.4.2 Time delay to position conversion . . . 35

6 Results **36**
6.1 Structure diagnostics . . . 36
6.1.1 TD26CC . . . 36
6.1.2 CLIC Crab Cavity . . . 39
6.1.3 T24 . . . 41
6.1.4 T24 open . . . 43
6.1.5 Summary . . . 45
6.2 Localization precision . . . 45
6.3 Vacuum arc studies . . . 47
6.3.1 Breakdown migration . . . 48
6.3.2 Spatio-temporal correlation of breakdowns . . . 52

7 Conclusions **55**
7.1 Summary . . . 55
7.2 Future work . . . 56
7.2.1 RF power and phase methods . . . 56
7.2.2 Other localization methods . . . 56
7.2.3 Vacuum arc studies . . . 57

References **60**

Appendix A Edge method parameter **66**

Appendix B Correlation method parameters **68**

Appendix C Time delay distribution of a constant gradient structure **70**

Appendix D Group velocity profiles **72**

Symbols and abbreviations

Symbols

a	scaling factor
α	attenuation coefficient
$\mathbf{B}$	magnetic field (T)
c	speed of light ($\approx$ 299 792 458 m/s)
C	cost function
$\mathbf{E}$	electric field (V/m)
ϵ	electric permittivity (F/m)
f	frequency (Hz)
φ	RF phase advance per cell (rad.)
G	Accelerating gradient (V/m)
$\mathbf{J}$	displacement current density (A/m^2)
λ	wavelength (m)
m	filtering criterion (arb. units)
μ	magnetic permeability (H/m)
$n,\ k$	sequence index ($\in \mathbb{Z}$)
$N,\ K$	sequence length ($\in \mathbb{Z}^+$)
ω	angular frequency (1/s)
p	edge method parameter
ρ	charge density (C/m^3)
$\mathbf{S_c}$	modified Poynting vector (W/m^2)
t	time (s)
T	time segment (s)
τ	time delay (s)
θ	phase (rad.)
U	signal energy (J)
v	speed (m/s)

Operators

$\mathbb{E}[x]$	expectation of random variable x
$\nabla \cdot \mathbf{a}$	divergence of vector $\mathbf{a}$
$\nabla \times \mathbf{a}$	curl of vector $\mathbf{a}$
$\mathbf{a} \times \mathbf{b}$	cross product of vectors $\mathbf{a}$ and $\mathbf{b}$

Abbreviations

BDR	Breakdown rate
CDF	Cumulative distribution function
CERN	European Organization for Nuclear Research (Conseil Européen pour la Recherche Nucléaire)
CLIC	Compact Linear Collider
CRLB	Cramér-Rao lower bound
DC	Direct current
INC	Incident RF power
LHC	Large Hadron Collider
LINAC	Linear acclerator
MSE	Mean squared error
MVUE	Minimum variance unbiased estimator
PDF	Probability density function
REF	Reflected RF power
RF	Radio frequency
RMSE	Root mean squared error
RSS	Received signal strength
Rx	Receiver
SNR	Signal-to-noise ratio
TDOA	Time difference of arrival
TeV	Teraelectron volt (or 10^{12} eV, where 1 eV $\approx 1.602176565 \cdot 10^{-19}$ J)
TRA	Transmitted RF power
Tx	Transmitter

1 Introduction

1.1 Background

The *Compact Linear Collider* (CLIC) is an international collaboration aiming to develop a next generation electron-positron particle accelerator capable of reaching TeV collision energies [1]. CLIC is primarily developed at CERN, the *European Organization for Nuclear Reseach*, which is located close to Geneva, on the border of France and Switzerland. The goal of CLIC is to complement the high-energy physics studies of the world's largest particle accelerator: the 24 km long *Large Hadron Collider* (LHC). The LHC is a *circular collider*, designed to accelerate hadrons (usually protons). Hadrons are composite particles that have a wealth of collision products. Therefore, hadron colliders are useful for discovering new physics. However, they are not as well suited for precision physics as elementary particle (lepton) colliders.

Energy losses in *synchrotron radiation* is a leading argument for *linear accelerators* (LINACs). Synchrotron radiation is emitted when a charged particle travels along a curved trajectory. The losses due to synchrotron radiation are inversely proportional to the 4^{th} power of the accelerated particle's mass. Since electrons have $\mathcal{O}(10^{-3})$ smaller mass than protons, synchrotron radiation losses for electrons become impractically large in a circular collider.

Reaching TeV collision energies requires strong electric and magnetic fields. The average accelerating gradient of CLIC is required to reach 100 MV/m [1], which poses serious technical challenges. One of the foremost issues are *vacuum arcs*, i.e. *electrical discharges* between the conducting surfaces in the accelerator. These discharges, also known as *breakdowns*, damage the accelerator, cause energy losses and destabilize the particle beam [21, 22]. Consequently, it is important to keep the *breakdown rate* (BRD) in the accelerator sufficiently low. High-gradient tests on CLIC prototype accelerating structures have already demonstrated that this can be achieved, but only after a lengthy process called *conditioning* [2]. During conditioning the structure is subjected to up to billions of *radio frequency* (RF) pulses, which gradually increase the structure's resilience against breakdown. A better understanding of the physics of vacuum arcs could lead to more efficient conditioning strategies, which would reduce the costs and time required for producing RF accelerating structures [3].

Breakdown *localization* or *positioning* is a useful tool for understanding fundamental vacuum arc mechanisms like conditioning. Furthermore, localization is important from an RF design and operation point of view. For example, position information can be used to diagnose abnormal structure behavior [4, 5] and pinpoint potential trouble spots in the structure design, manufacturing and testing.

1.2 Scope and outline of thesis

In this thesis, methods for localizing vacuum arcs in room temperature traveling-wave RF linear accelerating structures are studied. The emphasis is on extending

RF power based localization methods and applying these methods to experimental data, for the purposes of structure diagnostics and fundamental vacuum arc studies. It should be mentioned that although breakdown *detection* is an essential pre-processing step to localization, it is not treated in detail here in order to limit the scope of the work. For similar reasons, recent progress on acoustical breakdown positioning is not fully detailed, but only briefly mentioned in section 7.2.2.

The thesis is structured as follows: In sections 2 and 3, relevant signal processing and RF LINAC concepts are introduced. The experimental setup is described in section 4. Section 5 presents the positioning methods. Experimental results are shown in section 6. Finally, the work is summarized and future research topics are discussed in section 7.

1.3 Goals and contributions of thesis

This thesis contributes to the ongoing research on vacuum arcs in RF LINACs. In particular, the focus is on breakdown localization in four CLIC prototype RF accelerating/deflecting structures. The work builds on two existing RF power and phase based positioning methods, the *edge* and the *correlation method*, which are standard tools in the field (see e.g. [6, 7]). However, to the author's knowledge, an in-depth analysis, comparison and documentation of the methods is still lacking. Therefore, the main goals of this thesis are

1. Reviewing different methods used for breakdown localization in RF accelerating structures
2. Extending existing RF power and phase based methods
3. Quantifying the localization accuracy of the used methods
4. Applying the methods to real-world measurement data from prototype RF accelerating structures in order to perform structure diagnostics as well as study vacuum arcs.

In the process of accomplishing these goals, novel contributions were made. In particular, the central achievements of this work are

- Parametrizing and comparing the edge and correlation methods
- Exploring the assumptions of the edge method and deriving an expression for its bias
- Quantifying the positioning precision of the edge and correlation methods in two different structures during hot cell periods
- Providing breakdown position information from some of the high-power test stands at CERN, as support for operational decisions
- Finding new evidence supporting the breakdown migration hypothesis
- Discovering a correlation of between the inter-arrival times and positions of consecutive breakdowns.

1.4 Notation

Scalars are referred to by unbold letters (e.g. a, A) and vectors by bold letters ($\mathbf{a}$, $\mathbf{A}$). Estimators are denoted by a hat. For example, $\hat{a}$ is an estimator of the scalar a.

The standard signal processing convention of denoting matrices by bold uppercase letters is neglected, firstly because of the widespread use of $\mathbf{E}$ and $\mathbf{B}$ as the electric and magnetic field vectors in the literature and secondly because of the lack of matrices in this work.

2 Relevant signal processing concepts

This section introduces the signal processing background necessary for understanding the discussion in later sections. In particular, the fundamentals of *statistical signal processing* and *estimation* in the context of localization are outlined. This sets a framework within which positioning algorithms can later be analyzed (section 5). Additionally, the use of *cross-correlation* in localization is described. Cross-correlation can be used to estimate the delay between two signals, which makes it a useful tool in positioning.

For a more thorough treatment of the aforementioned topics see e.g. [8–10].

2.1 Statistical signal processing

Statistical signal processing is concerned with detecting signals embedded in noise and estimating their statistical properties. The latter of the two, i.e. estimation, is of main interest in this work.

Estimation is the procedure of inferring the value of a variable or parameter of interest from observed data. For example, one may be interested in estimating the mean of a probability distribution. The estimation algorithm is called an *estimator* and the output of the estimator is referred to as the *estimate*. The data used by the estimator may consist of direct or indirect observations of the quantity to be estimated. In the non-trivial case of indirect observations, the variable of interest is often a parameter of a model, which is fit to the data. Typically, the goal of estimation is to find an estimator which is

1. *Unbiased*, i.e. there is no systematic error
2. *Precise*, i.e. estimates have a small variance.

The concepts of unbiasedness and precision are illustrated next. Let x be a variable of interest (unobservable), which is indirectly embedded in the data d (observable) of the random process D. Additionally, let $\hat{x}$ be an estimator of x. It follows that $\hat{x}$ is a random variable (although x is not necessarily), since real-world data always contains noise. The estimator is said to be unbiased if

$$\text{Bias}(\hat{x}) = \mathbb{E}[x - \hat{x}] = 0. \tag{1}$$

The precision of an estimator is determined by its variance: the smaller the variance, the more precise the estimator. Due to finite sample size and noise, there exists a theoretical lower bound for the achievable variance of an unbiased estimator called the *Cramér-Rao lower bound* (CRLB). An unbiased estimator that achieves the CRLB for any sample size is considered optimal and called the *minimum variance unbiased estimator* (MVUE). Quite often, the MVUE is too difficult to obtain and one must settle for an asymptotically optimal or a sub-optimal estimator [8].

The CRLB is defined as the inverse of the *Fisher information*, which is a measure of the information that observations d of the random process D contain about the

unknown variable x. Therefore, the variance of an unbiased estimator must fulfill [8]

$$\mathrm{Var}(\hat{x}) = \mathbb{E}[(\hat{x} - \mathbb{E}[\hat{x}])^2] \geq I(x)^{-1}, \tag{2}$$

where $I(x)$ is the Fisher information

$$I(x) = \mathbb{E}[(\frac{\partial \ell(x)}{\partial x})^2] = -\mathbb{E}[\frac{\partial^2 \ell(x)}{\partial x^2}] \tag{3}$$

and $\ell(x)$ is the log-likelihood function based on the conditional *probability density function* (PDF) $f(d|x)$:

$$\ell(x) = \ln(f(d|x)). \tag{4}$$

2.2 Localization

Localization is an estimation problem where one has a finite set of indirect and noisy observations, into which a set of coordinates specifying a location are encoded. The problems of an unknown *transmitter* (Tx) or *receiver* (Rx) position are mathematically equivalent. Consequently, the case of an unknown Tx position and known Rx positions is considered next.

To illustrate how position information may be encoded into a signal, consider a sine wave of a known angular frequency ω:

$$x(t) = \sin(\omega t). \tag{5}$$

Now, imagine that $x(t)$ is transmitted and

$$y(t) = a \sin(\omega t - \theta) \tag{6}$$

is received somewhere. Since the signal is attenuated and delayed by the transmission channel, its amplitude and phase change. If the functional relationship between attenuation/phase and propagation distance is known, then the location information (in this example: distance between Tx and Rx) can be decoded from the amplitude or phase information. A typical model for a signal propagating distance z at speed v in a linear channel with attenuation factor α is

$$y(t) = e^{-\alpha z} \sin(\omega t + \omega \frac{z}{v}). \tag{7}$$

Eq. 7 shows an explicit relationship between amplitude, phase and distance. It is worth noting that if exclusively phase information is used, only distances below one wavelength may be resolved unambiguously. Generally, the resolution of time-based localization methods depends on the signal bandwidth.

Localization techniques that utilize amplitude information are referred to as *received signal strength* (RSS) methods. Techniques that use the relative phase or timing between different Rx are called *time-difference-of-arrival* (TDOA) methods. *Time-of-arrival* (TOA) refers to methods that use timing information relative to a common clock, to which all Rx are synchronized. *Angle-of-arrival* (AOA) methods

measure the direction (angle) to the Tx. Typically, a multiantenna array or steerable directional antenna is needed for AOA estimation. [9]

The solution to the mathematical problem of localization is called *triangulation*, *trilateration* or *multilateration*, depending on the measured variables and available a priori information [11]. The three solutions in 2D are illustrated in Fig. 1. Triangulation refers to positioning using intersecting lines obtained through AOA estimates (β_1,β_2). In trilateration, the distances (d_1, d_2, d_3) between Tx and Rx is estimated using RSS or TOA. Similarly, mulitlateriation uses the difference in distance (i.e. TDOA) between Tx and Rx pairs. In principle, N dimensional localization requires at least $N+1$ signals, unless additional information is available. For example, when $N = 1$ and the direction to the source is known, only one signal is sufficient for TOA and RSS (TDOA still requires two). However, because real-world data always contains noise, an overdetermined system of equations is usually solved using *least squares* techniques [9].

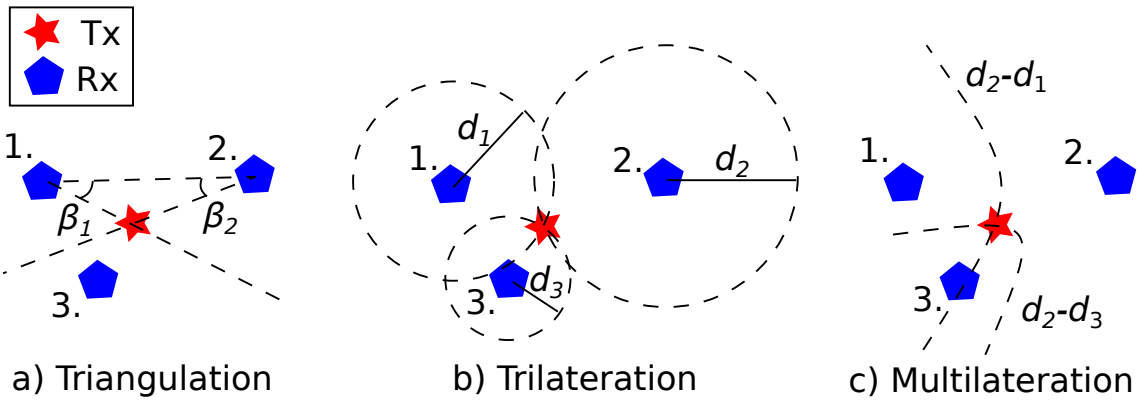

Figure 1: Solutions to the 2D localization problem using a) angle b) distance c) distance difference estimates.

2.3 Cross-correlation

Cross-correlation is a well established [10] tool for determining the similarity of two signals. Cross-correlation is often used to estimate the time delay of a signal of interest embedded in noise, as is the case in e.g. radar [8]. In radar, a *matched filter* correlates a known transmitted signal with a noisy received signal. The matched filter maximizes the *signal-to-noise ratio* (SNR) at the receiver and consequently allows for the distance to the reflecting object (e.g. an aircraft) to be estimated.

The continuous-time model traditionally used in time delay estimation using cross-correlation is presented next. Consider a measurement x, which consists of the signal of interest s scaled by a factor a, delayed by time τ_d and embedded in white noise w [10]:

$$x(t) = as(t - \tau_d) + w(t). \tag{8}$$

The cross-correlation between (real) signals x and s is

$$r_{sx}(\tau) = \int_{-\infty}^{\infty} s(t)x(t+\tau)\,\mathrm{d}t = a\int_{-\infty}^{\infty} s(t)s(t-\tau_d+\tau)\,\mathrm{d}t, \tag{9}$$

if w is uncorrelated with s and the argument of the integral is square integrable (i.e. s is an *energy signal*). The cross-correlation is maximized for $\tau = \tau_d$, as Eq. 9 reduces to the power of s, P_s, rescaled by factor a:

$$\max\, r_{sx}(\tau) = r_{sx}(\tau_d) = a\int_{-\infty}^{\infty} s^2(t)\,\mathrm{d}t = aP_s. \tag{10}$$

In practice, one has a discrete-time sample of finite length and the data are processed with a digital computer. Hence, the cross-correlation has to be estimated. An unbiased estimator for two sequences of equal length N is

$$\hat{r}_{sx}(k) = \frac{1}{N-|k|}\sum_{n=0}^{N-1} s(n)x(n+k),\ k = -(N-1),\ \ldots\ N-1. \tag{11}$$

The problem with Eq. 11 is that fewer samples are included in the calculation as one approaches the edges of the finite data record. In fact, when $k = -(N-1)$ or $k = (N-1)$, only one non-zero sample of x is used, which results in a noisy estimate. However, if signals x and s are of different length and certain limits on the possible delays can be imposed (see Appendix B), one may choose to evaluate the cross-correlation only within a window where the signals fully overlap. Consequently, bias is avoided at the edges and compensation as in Eq. 11 is unnecessary. Assuming $N_s < N_x$ and $0 \le n_d \le N_x - N_s$, the cross-correlation estimate is given by:

$$\hat{r}_{sx}(k) = \sum_{n=0}^{N_s-1} s(n)x(n+k),\ k = 0,\ \ldots\ , N_x - N_s. \tag{12}$$

The procedure of calculating the cross-correlation between two finite-length signals using Eq. 12 is illustrated in Fig. 2.

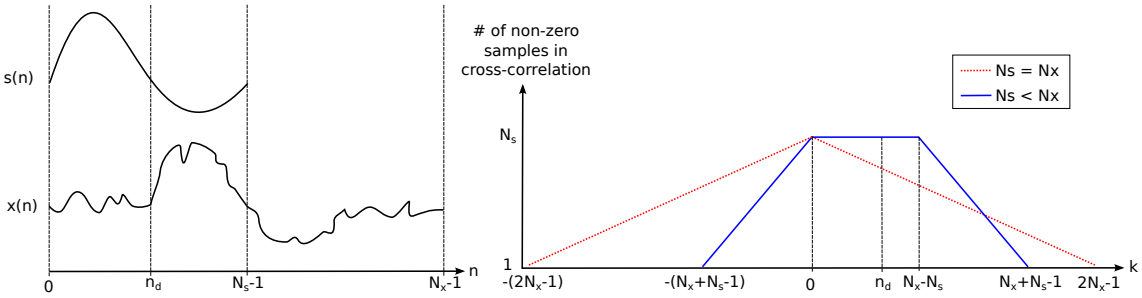

Figure 2: Cross-correlation of finite-length signals. Left: signals s and x. Right: the overlap of the two signals in the correlation sum when they are of equal and different length. Note that in Eq. 12 the cross-correlation is only evaluated for $0 \le k \le N_x - N_s$, which is the region where x and s fully overlap.

In certain situations, the *mean squared error* (MSE) criterion can provide a more robust measure of correlation than the classical cross-correlation (Eq. 9). This is the case when the linear signal in uncorrelated noise model of Eq. 8 does not exactly hold. For example, in the presence of non-linearities in the transmission channel, estimating the correlation for different scalings of s may be necessary. This is possible with a statistical criterion such as the MSE that uses a difference (estimation error) instead of a product as a measure of signal similarity.

3 Radio frequency linear accelerators

The working principle of *radio frequency linear accelerators* (RF LINACs) is described in this section. The term radio frequency is often used in a broad sense to refer to both radio and microwaves in the frequency range of $\mathcal{O}$ (0.1 - 100 GHz) [12].

The origins of RF LINACs can be traced back to the 1920s when Rolf Wideroe experimentally demonstrated the concept of a linear particle accelerator using time varying electromagnetic fields [13]. It was discovered that RF accelerators could achieve significantly higher collision energies than their electrostatic counterparts, which were fundamentally limited by electrical breakdown at high voltages.

RF acceleration is based on the synchronicity between the particles and the accelerating field. In order to maximize the net energy gain, the particles are exposed to the crest of the accelerating field and hidden from the decelerating field. In the classical Wideroe design (Fig. 3), the latter is achieved by drift-tubes, in which the particles reside, while the external field has decelerating polarity. These tubes get progressively longer towards the beam output, since the distance traveled by the particles in a given time increases as they gain energy. Fig. 3 shows a drift-tube LINAC prototype from Linac4 at CERN. For a thorough treatment on RF LINACs, the interested reader is referred to [14].

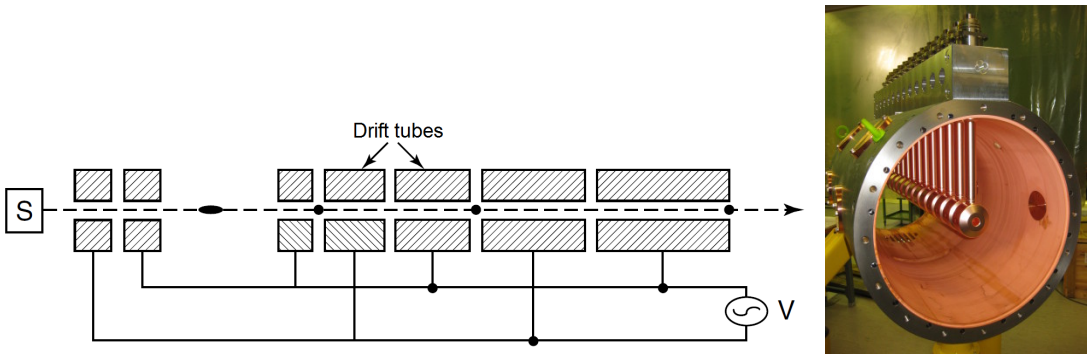

Figure 3: Drawing of a Wideroe drift-tube LINAC [14] and picture of a prototype drift-tube LINAC from Linac4 at CERN [15].

3.1 Electromagnetic waves

The foundation of modern *electromagnetic* theory was laid by 19^{th} century scientist James Clerk Maxwell [16]. Maxwell's four fundamental equations describe the electromagnetic phenomenon in terms of an electric and magnetic field, which interact with each other and propagate in a wavelike manner. In differential form, Maxwell's

equations read [17]

$$\nabla \cdot \mathbf{E} = \frac{1}{\epsilon}\rho \tag{13}$$

$$\nabla \cdot \mathbf{B} = 0 \tag{14}$$

$$\nabla \times \mathbf{E} = -\frac{\partial \mathbf{B}}{\partial t} \tag{15}$$

$$\nabla \times \mathbf{B} = \mu(\mathbf{J} + \epsilon\frac{\partial \mathbf{E}}{\partial t}). \tag{16}$$

Here ϵ and μ are medium dependent parameters (electric permittivity and magnetic permeability), $\mathbf{E}$ and $\mathbf{B}$ are the electric and magnetic fields and $\mathbf{J}$ is the displacement current. Qualitatively, Maxwell's equations describe how the electric field depends on the distribution of charge ρ (Eq. 13), that there are no magnetic monopoles (Eq. 14) and that a change in either the electric or magnetic field induces a change in the other (Eq. 15 and 16). For a thorough introduction to electrodynamics the interested reader is referred to [17].

By imposing appropriate boundary conditions, Maxwell's equations can be solved for arbitrary geometries. Actually, the solution in free space under vacuum shows that electromagnetic waves propagate at the speed of light. This fact eventually led Maxwell to conjecture that light itself is an electromagnetic wave [16].

3.2 Waveguides and cavities

When electromagnetic waves are confined to propagate in an enclosed region, standing waves occur due to reflections at the boundaries. Consequently, certain distributions of the electromagnetic fields are preferred over others. Formally, these spatial distributions are referred to as the *eigenmodes* of the geometry.

Maxwell's equations can be analytically solved for simple geometries such as waveguides and cavities with a rectangular or circular cross-section. Consequently, their properties are well understood and they are frequently used in real-world RF applications.

A waveguide is essentially a hollow tube with electrically conducting inner surfaces used to transfer electromagnetic power in a controlled manner. The useful frequency band of a uniform waveguide is determined by its cross-section. Most importantly, the cross sectional dimensions fix the cut-off frequencies of the eigenmodes. Frequencies below the cut-off do not propagate in the waveguide, but decay exponentially.

Resonant RF cavities are another important electromagnetic geometry. A resonant RF cavity is a closed waveguide, in which the fields build up and store energy at the *eigenfrequencies*. For example, a circular waveguide closed at both ends is called a cylindrical cavity. A cylindrical cavity driven at its fundamental eigenmode is depicted in Fig. 4.

The boundary conditions at a lossless conducting surface is [18]

$$\mathbf{E}_t = \mathbf{B}_n = 0. \tag{17}$$

In Eq. 17, $\mathbf{E}_t$ is the tangential and $\mathbf{B}_n$ the normal component of the electric and respectively, the magnetic field. Combining Eq. 17 with the appropriate boundary conditions of an arbitrary geometry yields solutions to Maxwell's equations (Eq. 13 - Eq. 16) in the form of *spatial harmonics* (eigenmodes). The standard shorthand for referring to these modes specifies

(a) which field component (electric, magnetic or both) is transverse to the propagation direction of the wave

(b) how many spatial half periods the mode has in the chosen coordinate system.

For example, light in free space travels as a TEM wave [18], which means that both the electric and magnetic fields are transverse to the direction of propagation (i.e. both have a zero field component in that direction). The TEM mode is not supported by the boundary conditions of hollow rectangular and circular waveguides or cavities [12]. Instead, only TM (transverse magnetic) and TE (transverse electric) modes may exist.

For circular waveguides, the number of half periods of the mode are specified in

(i) the angular direction

(ii) the radial direction.

For rectangular waveguides, (i) and (ii) are replaced by the transverse horizontal and transverse vertical directions. Modes in circular and rectangular cavities can also have half period variations in the longitudinal direction. For example, the fields of the TM_{010} mode in a circular cavity are constant in the angular and longitudinal directions, but have one half period variation in the radial direction (Fig. 4).

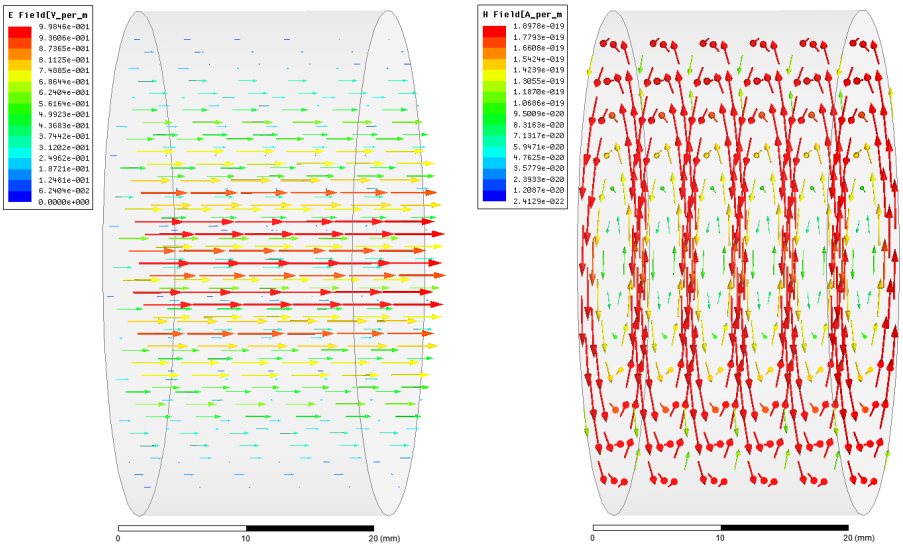

Figure 4: TM_{010} eigenmode of a cylindrical cavity simulated in HFSS [19]. Left: electric field. Right: magnetic field.

3.3 Phase and group velocity

It is necessary to make a distinction between two different propagation speeds of guided waves. *Phase velocity* refers to the propagation speed of a monochromatic wave, that is

$$v_p = \frac{\mathrm{d}\phi}{\mathrm{d}t} = f\lambda, \tag{18}$$

where f is the frequency and λ the wavelength of the wave. As real world signals are never truly monochromatic, there is always some inter-frequency modulation present in the signal. The propagation speed of this modulation is called the *group velocity* and is defined

$$v_g = \frac{\mathrm{d}f}{\mathrm{d}\lambda^{-1}}. \tag{19}$$

The difference between phase and group velocity is illustrated in Fig. 5. As the two sinusoidal waves propagate at their respective phase velocities $v_{p,1}$ and $v_{p,2}$, the envelope of their sum propagates at the velocity v_g, i.e. the group velocity.

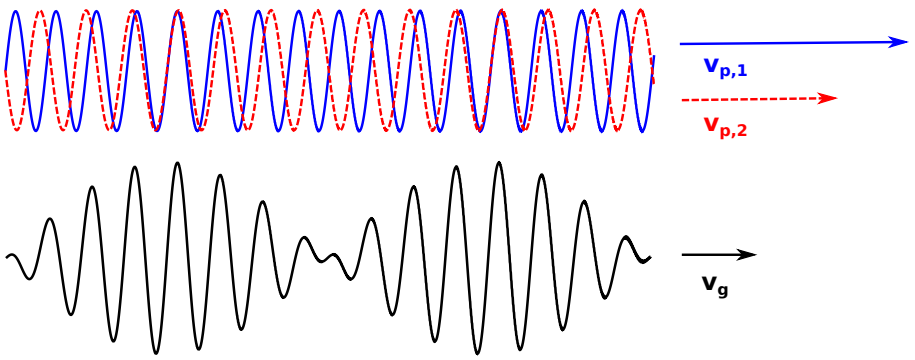

Figure 5: Phase and group velocity. The interference pattern of two sinusoidal signals with different phase velocities ($v_{p,1}$ and $v_{p,2}$) travels at group velocity v_g. Adapted from [14].

It can be shown that the phase velocity is always greater than the speed of light for waves propagating in a uniform waveguide [14]. Conversely, the group velocity is always less than the speed of light, since it is the speed at which information and energy travel [17]. The reason $v_p > c$ can be illustrated as follows: a monochromatic plane wave traveling at the speed of light c, is reflected off the inner walls of a waveguide, which causes the wave to interfere with itself (Fig. 6). The resulting wavefront has a larger wavelength in direction z than the original wave, that is $\lambda_z > \lambda$. Since the temporal frequency of the wave remains unchanged, the propagation speed in direction z must be larger than that of the incident wave:

$$f = f_z \Rightarrow \frac{c}{\lambda} = \frac{v_z}{\lambda_z} \Rightarrow v_z = \frac{\lambda_z}{\lambda}c > c. \tag{20}$$

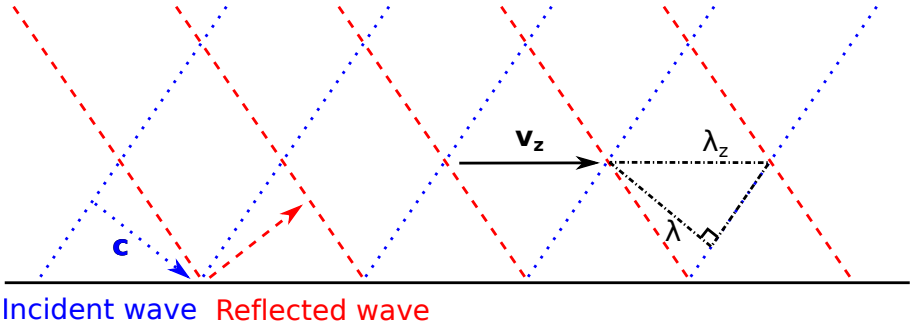

Figure 6: Reflection of wavefront from wall. The interference pattern between the incident and reflected waves always results in a wave with an increased wavelength and propagation velocity in a certain direction. Adapted from [18].

3.4 Periodic accelerating structures

For acceleration to be possible, the phase velocity of the accelerating field must be equal to the particle speed in the direction of motion. Consequently, uniform waveguides are unsuited for particle acceleration. However, the phase velocity of a waveguide can be reduced by introducing obstacles in the propagation path of the wave. Reflections from these non-uniformities cause an interference pattern, which reduces the phase velocity [18]. In the case of electron LINACs, the phase velocity at the accelerating frequency is usually close to the speed of light.

A typical accelerating RF structure can be approximated as a circular waveguide with periodically spaced discs (Fig. 7), which determine the phase velocity and electrical field distribution along the structure. Each pair of disks separates an almost closed cavity, called a *cell*. Since each cell has an *iris* for the beam and RF power to pass through, the accelerating structure can be viewed as a bunch of resonant cavities connected in series. Therefore, the overall structure operates in a specific mode called the *structue* or *normal mode* [14, 18]. Actually each cavity mode, such as the TM_{010} (Fig. 4), are associated with a set of structure modes [14]. Basically all cavities oscillate in the same mode, but in different phases. Therefore, the structure mode is defined by the spatial phase distribution along the structure.

A central theoretical result called *Floquet's theorem* states that for an infinite periodic structure, the fields at two positions placed one period apartl differ by a constant complex factor [14]. For a lossless structure this means that the fields of two adjacent cells differ only by a constant phase factor. Consequently, the structure mode is given as a phase advance per cell.

An accelerating structure has several narrow pass-bands around its eigenfrequencies, of which typically the lowest is used for acceleration. Consequently, an incident signal with frequency content outside the pass-bands will be partially reflected at points of impedance mismatch, like the input of the structure.

Periodic accelerating structures can roughly be divided into two classes according to their working principle: *standing-wave* and *traveling-wave*. In a standing-wave structure, the accelerating field is built up in the whole structure simultaneously and

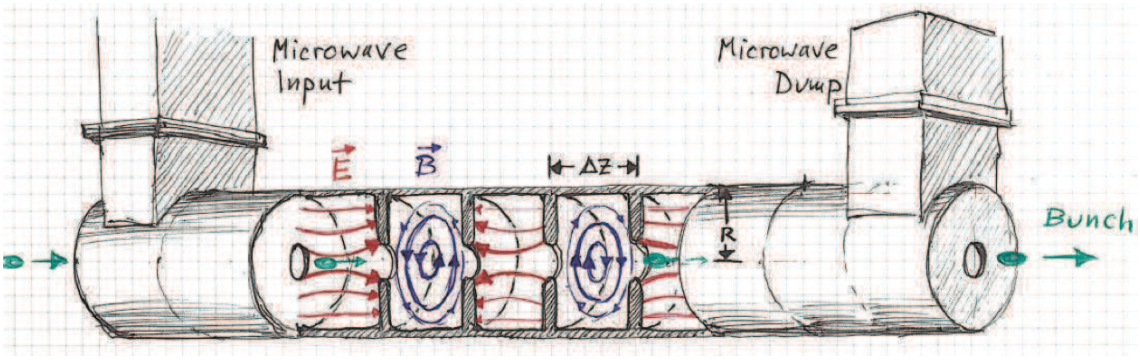

Figure 7: Conceptual drawing of a traveling-wave structure, with electric field (**E**) in red, magnetic field (**B**) in blue and accelerated particle bunch in green [20].

there is no propagation of energy. In a traveling-wave structure, the accelerating field and energy both propagate through the structure. In the former case, the standing wave is achieved by shorting the output end of the structure. In the latter case, the RF power at the output is dissipated into a resistive load. Exclusively traveling-wave structures are treated in this thesis, since the structures examined in section 4 are of this type. Fig. 7 shows a conceptual drawing of a traveling-wave structure operating in TM_{010} with a phase advance per cell of $\pi/2$.

It is convenient to further divide traveling-wave structures into *constant-impedance* and *constant-gradient* structures. Constant-impedance structures have a uniform cell geometry, which results in a constant power decay along the length of the structure. As a consequence, the power P and accelerating gradient G of the traveling wave decay exponentially as a function of longitudinal position z [14]:

$$P(z) = P_0 e^{-2\alpha z} \tag{21}$$

$$G_z(z) = G_0 e^{-\alpha z}. \tag{22}$$

P_0 in Eq. 21 is the power and G_0 in Eq. 22 is the gradient at the input of the structure, i.e. $z = 0$. The attenuation constant α is a function of the structure geometry and accelerating frequency.

In a constant-gradient structure the accelerating field does not vary along the length of the structure. This is achieved by decreasing the aperture of the irises towards the RF output, which is referred to as *tapering*. Tapering changes the group velocity and attenuation factor, which are both strong functions of the aperture size [14]. Consequently, the power of the traveling wave decays linearly, whereas the average accelerating gradient remains constant along the length L of the structure [14]:

$$P(z) = P_0\left(1 - \frac{z}{L}\left(1 - e^{-2\int_0^L \alpha(z)\,\mathrm{d}z}\right)\right) \tag{23}$$

$$G_z(z) = G_0. \tag{24}$$

3.5 Vacuum arcs

Vacuum arcs limit the achievable accelerating gradient in RF LINACs. Beam loss [21] and structure degradaton [22] are the main undesirable effects of breakdowns. The demand for ever larger collision energies translates to higher surface fields in the accelerating structures, which in turn increases the likelihood of electrical breakdown. A thorough understanding of the process leading to breakdown could be used mitigate their occurrence and harmful effects.

Conceptually, vacuum arcs are similar to gas discharges, of which lightning and static discharge are the most commonplace examples. Lighting occurs when the potential difference between a charged storm cloud and a grounded object (such as a tree), exceeds the dielectric resilience of air. Consequently, the insulating property of air breaks down and electrical current starts flowing between the potential gap. Similarly, a vacuum arc is an electrical discharge between two or more electrodes under vacuum [23]. The essential difference between gas discharges and vacuum arcs is that in perfect vacuum there is initially no conducting medium.

The modern understanding of vacuum arcs is largely based on the theory of electron field emission from the 1920's [24, 25]. The current picture of vacuum arc development in DC conditions can roughly be summarized as follows [23]:

1. Slight protrusions on the conductor surfaces cause local enhancement of the electrical field (up to $\mathcal{O}(10^2)$ [23])

2. The high local electrical fields cause electrons to tunnel out from the cathode into the vacuum. The free electrons then travel to the anode across the potential gap. This is called *electron field emission*.

3. The electron emission is associated with thermal field emission of neutral copper. The field emission current ionizes the the neutral copper atoms and causes them to travel back to the cathode.

4. Once a critical amount of matter is exceeded, a large current starts flowing between the gap. This ionizes the remaining neutral atoms and forms a plasma. A vacuum arc has formed.

5. The arc forms a crater and deforms the electrode surface, which can lead to new local field enhancement spots and a restarting of the process.

It has been observed that the maximum gradient in RF accelerating structures is limited, not by local surface magnetic or electric fields, but by local power flow [26]. In [26], a limiting field quantity called the modified Poynting vector ($\mathbf{S_c}$) is suggested and defined:

$$\mathbf{S_c} = \Re(\mathbf{S}) + g_c \Im(\mathbf{S}), \tag{25}$$

where g_c is a scaling factor that depends on the local electric field and $\mathbf{S}$ is the complex Poynting vector

$$\mathbf{S} = \frac{1}{\mu}\mathbf{E} \times \mathbf{B}. \tag{26}$$

A practical reason for studying breakdown is to better understand and eventually control the conditioning process. Conditioning is observed through the decreasing proneness of RF structures to break down, as a function of the number of experienced RF pulses [3]. It is hypothesized that the pulses lower the breakdown probability by e.g. destroying surface inhomogeneities, which could otherwise lead to a runaway process [27]. An important result from past conditioning studies is an empirical scaling law, which states that the probability of a breakdown follows a power law [27]. The law relates the accelerating gradient G and RF pulse length T_{pulse} to the breakdown rate as [26]

$$\text{BDR} \propto G^{30} T_{\text{pulse}}^{5}. \tag{27}$$

Eq. 27 allows normalization of the BDR to pulse length and gradient:

$$\text{BDR}* = \frac{\text{BDR}}{G^{30} T_{\text{pulse}}^{5}}. \tag{28}$$

Conditioning is essentially a desirable effect, but it is also slow and costly. It takes months for a virgin CLIC structure to condition to the nominal CLIC operating point ($T_{\text{pulse}} \approx 250$ ns, $G \approx 100$ MV/m [1]), whilst maintaining a sufficiently low breakdown rate (BDR $< 3 \cdot 10^{-7}$ 1/pulse/m [1]) [28]. At a repetition rate of 50 Hz this translates to $\mathcal{O}(10^8 - 10^9)$ pulses. It is therefore of considerable interest to find a way to speed up the process.

At CERN, breakdowns and conditioning are also studied in a DC setting [29]. This not only simplifies the experiments, but also provides a means to study conditioning faster by using higher repetition rates (up to 1 kHz) [29]. These experiments have given valuable insight into some of the fundamental similarities and differences between DC and RF breakdowns [30, 31].

4 Experimental setup

In this section, an overview of the experimental setup is given. The setup consists of two high-power tests stands, in which two RF structures (one each) can be tested simultaneously. The structures under test are pulsed at 50 Hz with $\mathcal{O}(100$ ns) long RF pulses reaching a peak power of tens of MW. Analysis signals used for breakdown localization are obtained through directional couplers placed at the inputs and outputs of the structures. In total, data from four structures was gathered and analyzed.

4.1 High-power test stands

High-gradient tests of prototype accelerating structures for CLIC are conducted in three klystron-based X-band (12 GHz) test stands called Xbox-1, 2 and 3 [32]. The Xboxes allow for rapid parallel high-power testing of accelerating structures and RF-components. Fig. 8 shows a birds-eye view of Xbox-2 and an accelerating structure installed inside a radiation shielded bunker.

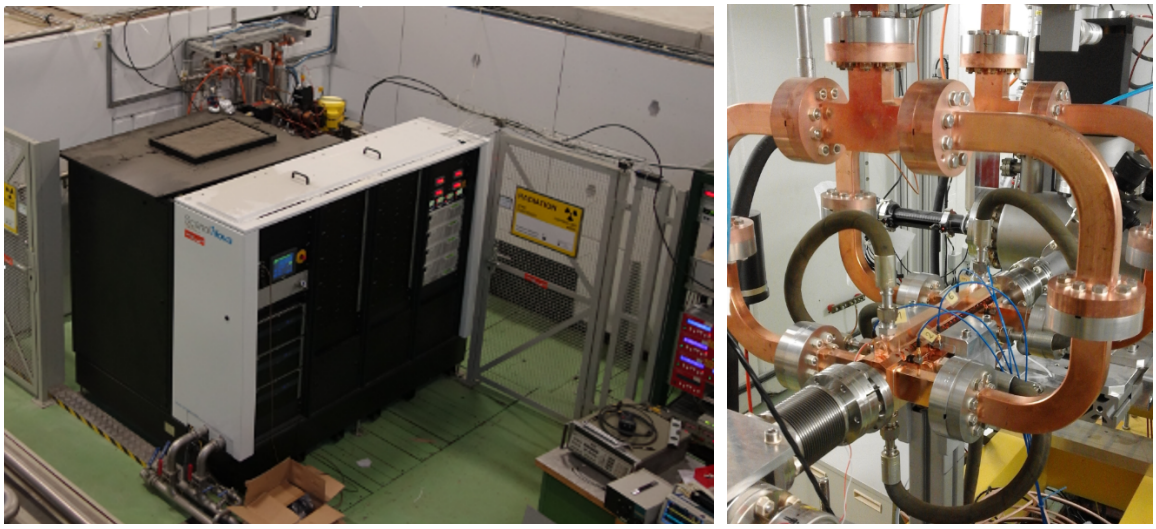

Figure 8: Left: Klystron-based test stand Xbox-2 [33]. Right: Accelerating structure (T24 open) installed inside the bunker of Xbox-2.

A simplified diagram of a high-power test stand is shown in Fig. 9. In the first stage, the 12 GHz RF wave generated by the low-level RF is amplified by a traveling-wave tube (TWT) to a few kW. The RF pulse is further amplified by a pulsed klystron and compressed by a pulse compressor (compression ratio, CR ≈ 3) in order to achieve the nominal CLIC pulse length and flat-top (constant envelope) power. After compression, the pulse travels though the accelerating structure, where it can be used for acceleration. Any remaining power after the structure is dissipated into an RF load. Weakly coupling directional couplers (50-60 dBm of attenuation) before and after the structure provide diagnostic signals for breakdown analysis. In Xbox-1 and 2, the high-power RF is produced by a Scandinova K2-3 solid state

modulator (50 Hz pulse repetition rate, 1.5 μs pulse length) [34] together with a 50 MW CPI VKX-8311A klystron [35].

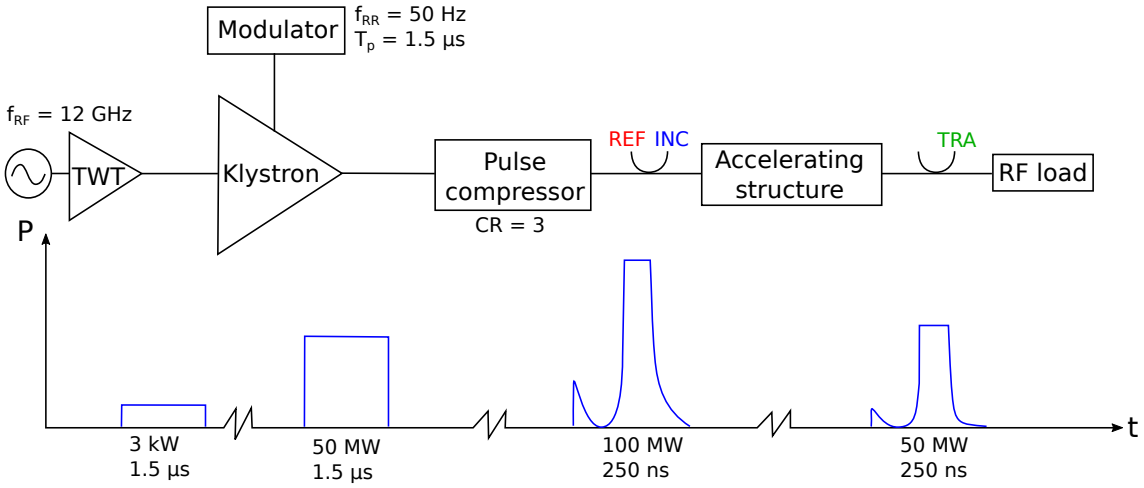

Figure 9: Block diagram of a high-power test stand and the typical RF pulse at different stages. Adapted from [32, 36].

The test stands are usually operated without the presence of beam in the accelerating structure, due to the need for conditioning and the high cost of beam time. In this *unloaded* mode of operation, all power not lost in the RF-network and structure walls is dissipated in the RF load. Conversely, during *loaded* operation, part of the injected RF energy is transferred to the beam during acceleration.

The main RF power signals used for breakdown analysis in Xbox-1 come from a *log-detector* attached to a 14-bit, 250 MHz analog-to-digital converter. The log-detector is essentially a logarithmical amplifier, whose wide dynamic range enables resolving even the most heavily attenuated signals from the structure. The log-detector also converts the 12 GHz RF pulse into a baseband signal, effectively extracting the signal envelope. Additionally, power and phase signals from an *IQ-demodulator* (8-bit, 1 GHz) are saved for offline processing. Furthermore, *accelerometers* were recently added for sensing mechanical vibrations caused by breakdowns. More details on Xbox-1 can be found in [37].

Xbox-1 is connected to a side branch of the probe beam line of the *CLIC Experimental area* called the *Dogleg*. The Dogleg allows for beam loading experiments, where the main objective is to observe how the presence of beam and the loading of the fields affect the breakdown statistics of structures [38].

Apart for the lack of beam test capability, Xbox-2 is mostly a copy of Xbox-1. As a minor difference to Xbox-1, in Xbox-2 mainly IQ-signals (12 bit, 1.6 GHz) are used fore breakdown analysis. Additionally, Xbox-2 has a *Faraday cup* installed at the beam input and output of the structure under test.

4.2 Structures under test

Four different structures were tested in Xbox-1 and 2: the T24 (Xbox-1), T24 open (Xbox-2), TD26CC (Xbox-1) and CLIC Crab Cavity (Xbox-2). The structures are made of copper and operated at a frequency of 11.9942 GHz in room temperature. Relevant unloaded structure parameters are given in Table 1. Group velocity profiles of the structures and the RF network up to the directional couplers are given in Fig. 60 - 63 of Appendix D.

4.2.1 T24

The T24 [39] is a constant gradient structure with 24 regular accelerating cells and input/output couplers for impedance matching to the the RF network. The tapering of the irises decreases the group velocity towards the output of the structure, as is shown in Fig. 60 of Appendix D. Fig. 10 shows a model of a disk of the T24 and the accelerating structure itself.

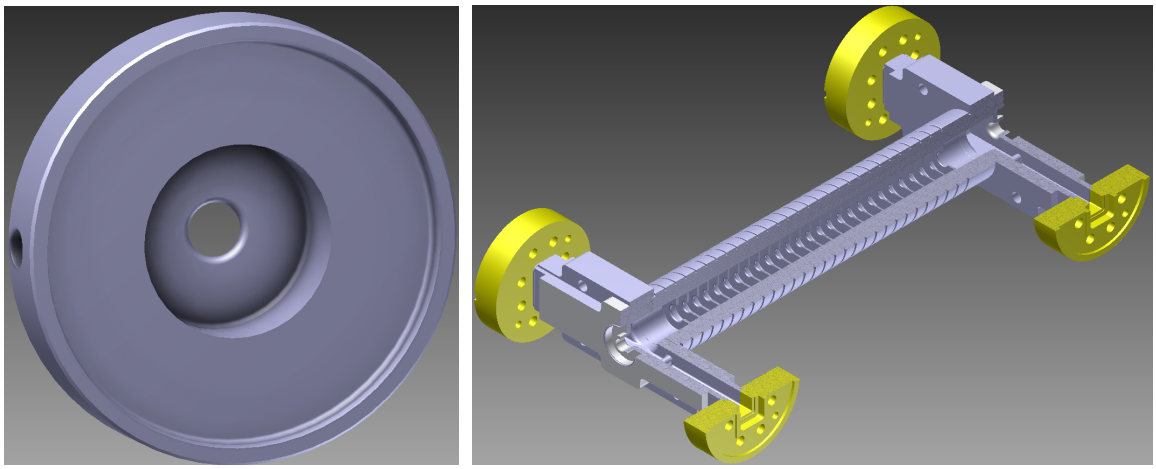

Figure 10: T24 cell and accelerating structure.

4.2.2 T24 open

The T24 open [40], is 24 cell prototype structure manufactured from two milled halves. The fabrication and assembly process is considerably simplified compared to the typical stacked disk structure used in the T24, TD26CC and CLIC Crab Cavity. A cross-section of the T24 open is shown in Fig. 11.

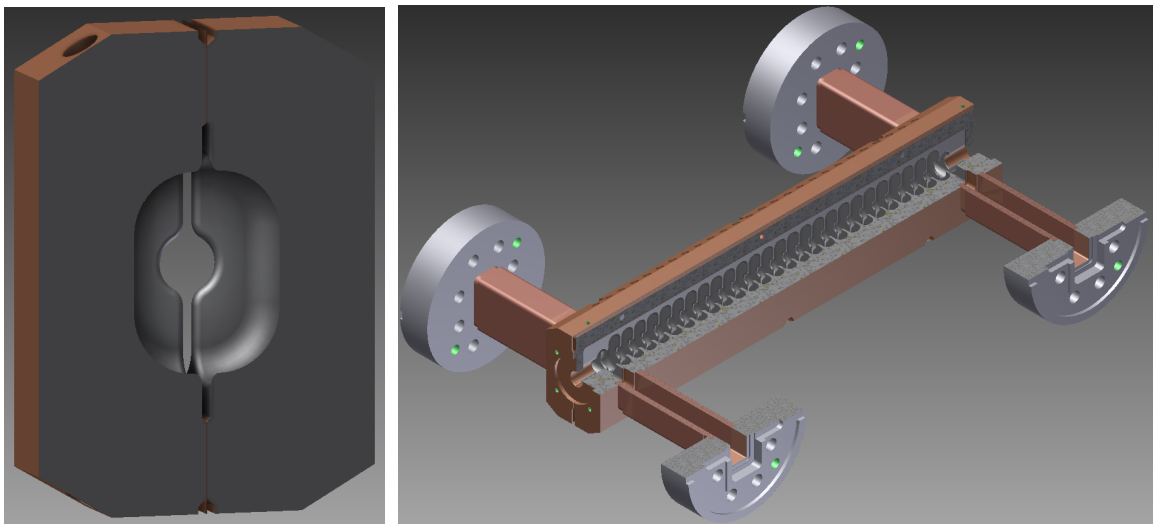

Figure 11: T24 open cell and accelerating structure.

4.2.3 TD26CC

The TD26CC [41] is a constant gradient accelerating structure, with 26 standard accelerating cells plus compact input and output couplers. Each cell of the TD26CC has four slotted waveguides for higher-order mode damping (Fig. 12).

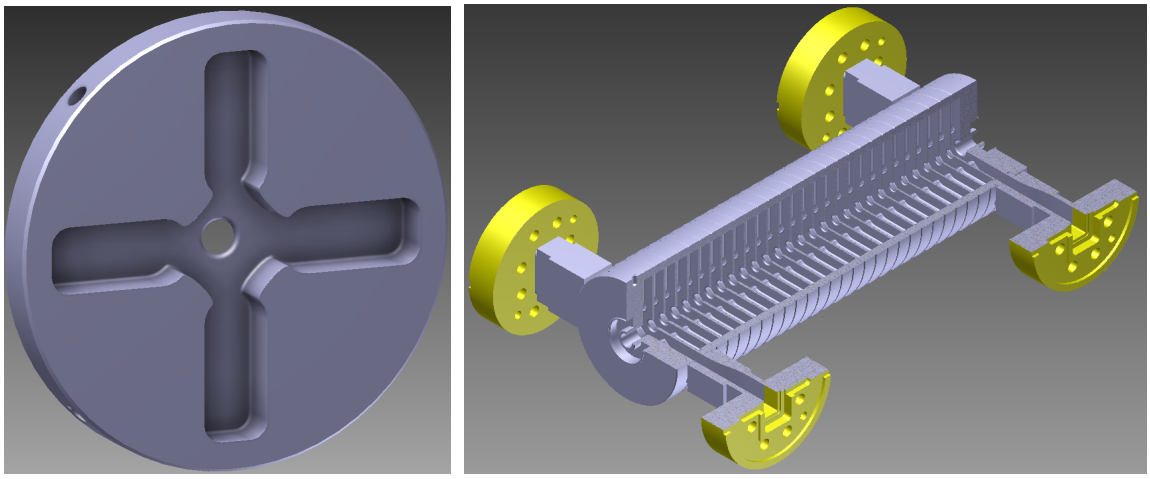

Figure 12: TD26CC cell and accelerating structure.

4.2.4 CLIC Crab Cavity

The CLIC Crab Cavity [32, 42] is a constant-impedance structure designed for transverse beam deflection. The structure operates in backward wave mode, i.e. the RF input is on the opposite side of the beam input. The Crab Cavity is shorter and has a higher group velocity than the other tested structures. Consequently, the group delay is small, which makes breakdown localization challenging.

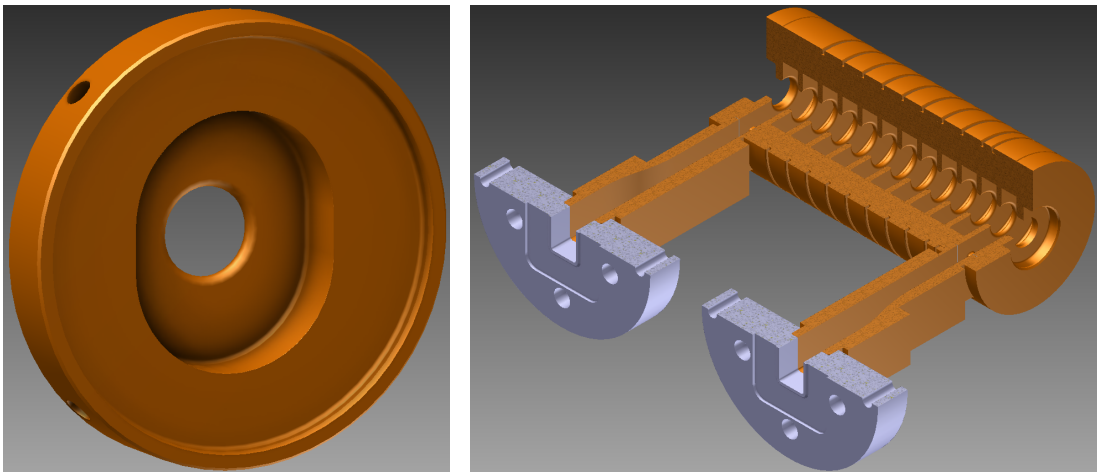

Figure 13: CLIC Crab Cavity cell and deflecting structure.

	T24	T24 open	TD26CC	Crab Cavity
No. of cells (regular, total)	24, 26	24, 26	26, 28	10, 12
Structure length (regular, total) [mm]	200, 228	200, 217	217, 233	83, 98
Attenuation [dB]	2.75	2.26	3.88	0.61
Group velocity, v_g (first, last cell) [% of c]	1.8, 0.9	2.0, 1.1	1.7, 0.8	2.9, 2.9
Group delay (first, last cell) [ns]	3.1, 6.0	2.8, 5.0	3.4, 6.7	2.0, 2.0
Filling time, τ_{fill} [ns]	59	50	67	11
RF phase advance per cell, φ [rad]	$2\pi/3$	$2\pi/3$	$2\pi/3$	$2\pi/3$
Input power [MW]	37.2	44.4	43.0	13.4
Peak surface E [MV/m]	219	313	230	89
Peak S_c [MW/mm^2]	3.4	5.3	3.9	1.8

Table 1: Nominal unloaded parameters of the four structures under test [32, 39–41].

5 Methods of vacuum arc localization

In this section, the most commonly used vacuum arc localization methods are presented. Two RF power based methods, the *edge* and *correlation* method, are described in detail. The use of RF phase as a complement to the aforementioned methods is explained. Finally, some data pre and post-processing steps that are necessary for accurate localization are outlined.

5.1 Overview of existing localization methods

Fig. 14 illustrates examples of signals used in breakdown positioning. In most cases, RF power and phase are monitored, since they are the main diagnostic tools of structure testing [7, 28]. Additonally, accelerometers are sometimes placed on the outer shell of a structure to pick up vibrations in the range of $\mathcal{O}(10^4$–10^6 Hz), induced by breakdowns and pulsed surface heating [5, 43]. The high frequency content is due to the fast breakdown turn-on time ($\mathcal{O}(10$ ns) [44]) and short RF pulse length ($\mathcal{O}(100$ ns)).

Furthermore, breakdowns radiate electromagnetic energy over a wide frequency range. This enables X-ray [7, 45] and visible light [46] arc imaging. It has even been proposed to fit optical fibres inside the structure in order to see the breakdown cell [47].

RF pulses and breakdowns also pull off electrons from the surface of the bulk copper. These electrons are accelerated by the electromagnetic fields in the structure before being ejected through the beam pipe. In [48], an electron spectrometer [49] is used to image the angular breakdown position. Additionally, currents picked up by Faraday cups are regularly used to determine the absolute timing of breakdowns [6]. Moreover, the longitudinal and angular breakdown distributions are routinely studied in post-mortem analyses, in which structures are dissected and inspected using e.g. optical and scanning electron microscopes [50, 51].

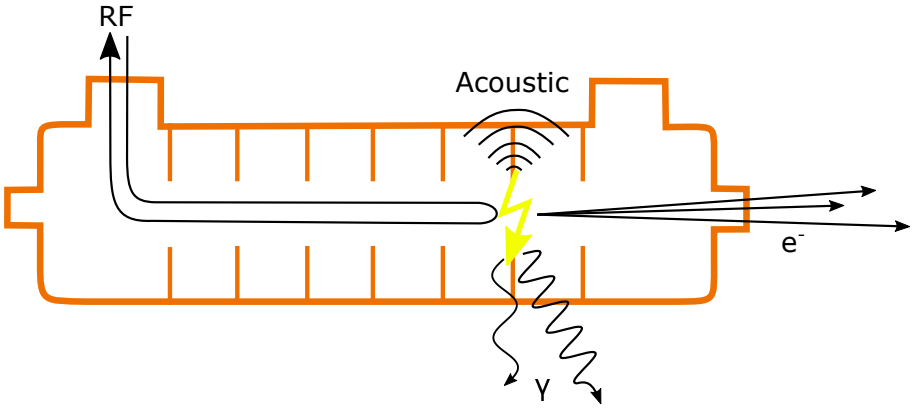

Figure 14: Examples of signals carrying breakdown position information.

5.2 RF power and phase methods

In traveling-wave structures, three signals are typically recorded: RF power *incident* on the structure (INC), power *reflected* from the structure (REF) and power *transmitted* through the structure (TRA). If the accelerating structure is well matched to the rest of the RF network, reflections from the structure should be minimal, which means that during normal operation only the incident and transmitted RF power are nonzero.

A breakdown acts as a short circuit, which causes reflection and loss of transmission (Fig. 16). The transmitted and reflected signals are delayed and attenuated by the propagation in the structure and RF network. These signals can be used to determine the location of the breakdown using TDOA or RSS. Since the precise reflection/absorption characteristics of the breakdown are unknown, a TDOA approach is often more robust. Therefore, the round-trip time of REF (τ_{RT} in Fig. 15) is estimated. In practice, the time taken by the incident signal to travel from the directional coupler to the breakdown cell and back is measured ($\tau_{d,\mathrm{REF}}$ in Fig. 15).

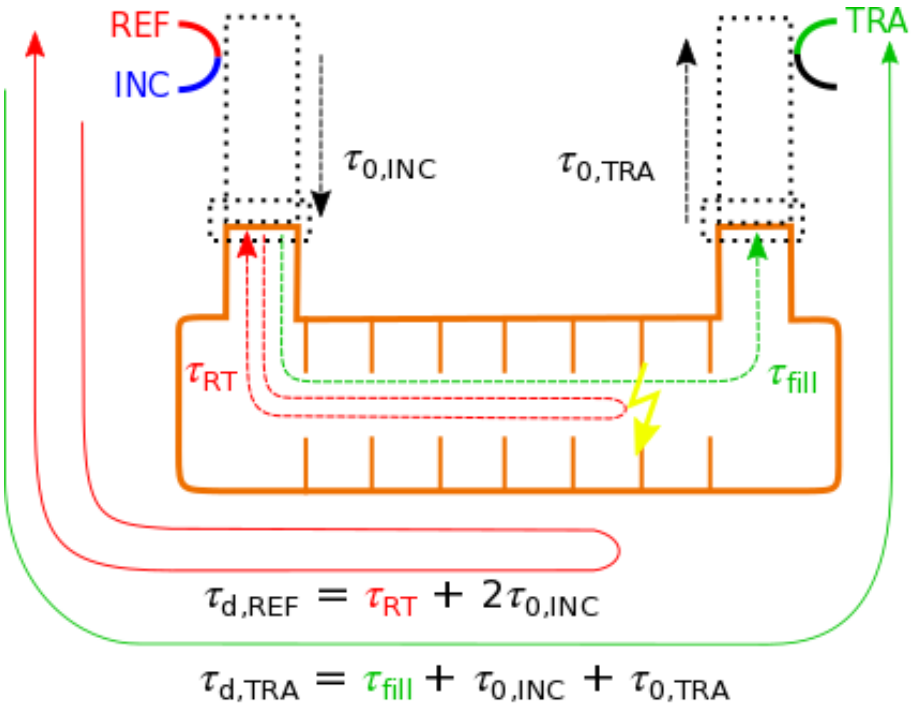

Figure 15: RF signal time delays in a traveling-wave structure. The round-trip time τ_{RT} is used to localize the breakdown. In practice, $\tau_{d,\mathrm{REF}}$ is first estimated using the TDOA approach on REF and TRA or REF and INC.

The high-frequency content of the RF pulse envelope is the main source of reflections during non-breakdown pulses. During a breakdown, the incident power is almost completely reflected. Multiple reflections are also observed in both the reflected and incident signals. The time delay between these reflections roughly corresponds to the round-trip time between the structure and the klystron. The

klystron and breakdown plasma act as a short circuit [6], reflecting the RF power back and forth until it is fully attenuated or the arc is extinguished.

Also other RF power based localization methods exist. In [52], using the unique spectral fingerprints of standing wave cavities is suggested. The fingerprint depends on the number of RF cavities connected in series, which is determined by the breakdown iris, where the structure is electrically decoupled into two parts for the duration of the discharge. Another approach is to probe the RF-network in a higher passband. For example, in [53] the authors propose to deduce the breakdown position from a frequency dependent reflection coefficient measurement.

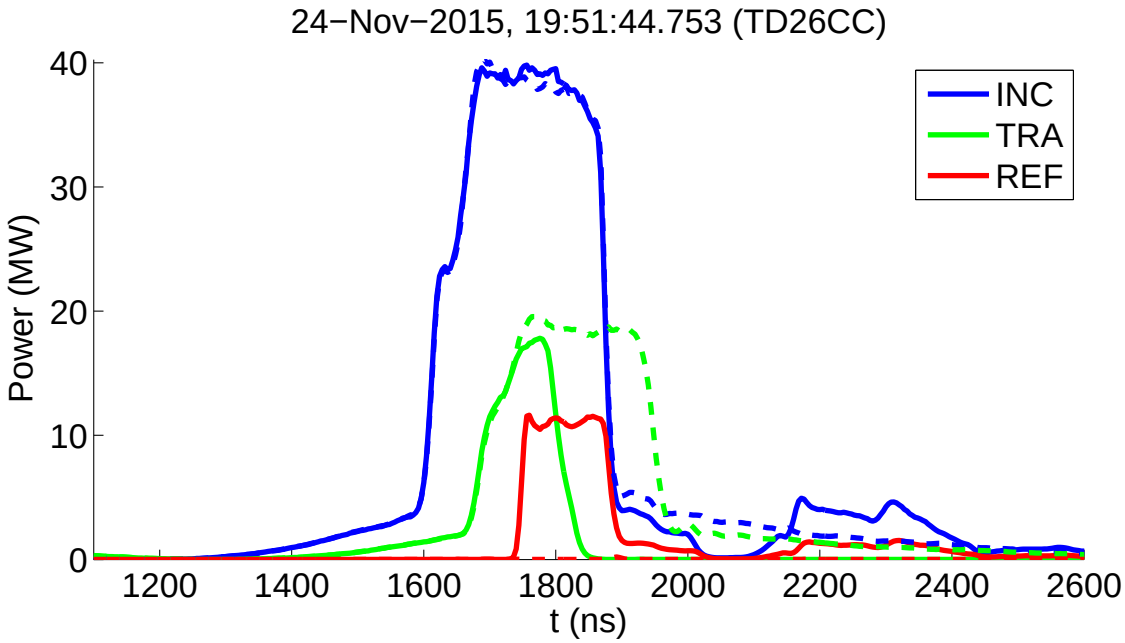

Figure 16: RF power signals. Solid lines show breakdown pulse, dashed lines show previous pulse. Breakdown is characterized by an abrupt drop in transmitted power and rise in reflected power.

5.2.1 Edge method

The TDOA of the falling edge of TRA and the rising edge of REF provide a first method for breakdown localization. Assuming that the vacuum arc starts absorbing and reflecting RF power instantaneously as the breakdown is ignited, the delay between the two edges should correspond to a unique longitudinal position. A simple approach is to define the falling edge as the time $t_{\mathrm{TRA},p}$, when TRA has fallen to a fraction p of its maximum value (Fig. 17). Similarly, the rising edge is the instant $t_{\mathrm{REF},1-p}$, when REF has risen to $1-p$ of its maximum value. Hence,

$$\hat{\tau}_{d,\mathrm{edge}} = t_{\mathrm{REF},1-p} - (t_{\mathrm{TRA},p} - \tau_{\mathrm{fill}}) \tag{29}$$

is an estimator for the round-trip time that assumes values between zero and twice the filling time, $2\tau_{\mathrm{fill}}$.

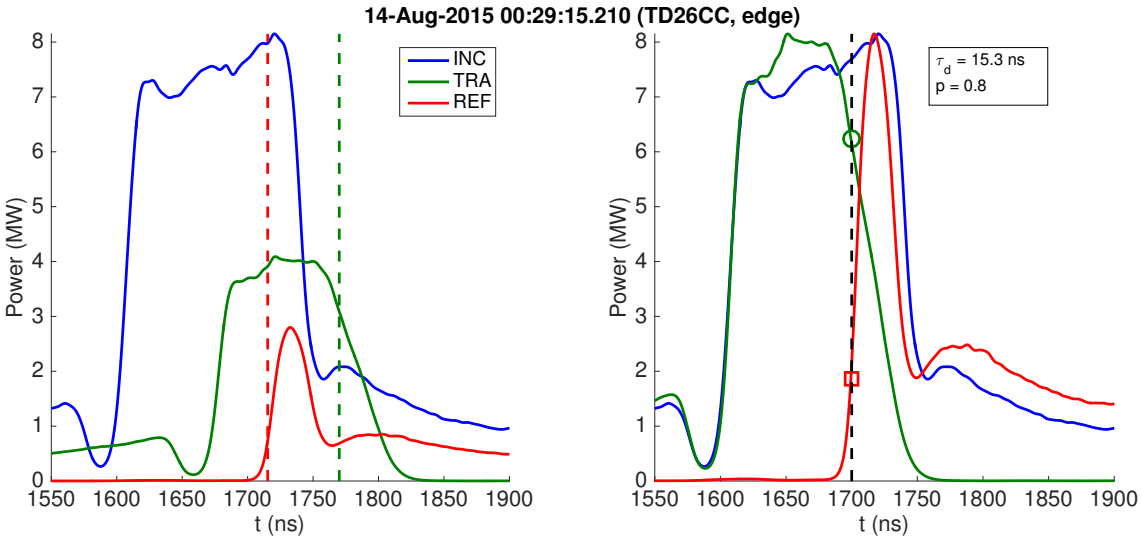

Figure 17: Edge method. Left: Acquired signals. Dashed vertical lines show detected edges. Right: TRA and REF rescaled and delayed so that the edge markers fall on the same vertical line.

In the absence of noise, the variable p can be chosen arbitrarily, provided that the slopes of the rising and falling edges are equal. If the slopes are not equal, p should be 1. Otherwise the estimator of Eq. 29 is biased. The situation is illustrated in Fig. 18, which depicts the edges of the transmitted and reflected RF power during a breakdown. Assuming that the start of the falling edge, t_{TRA}, and rising edge, t_{REF}, can be traced back to the same time instant (the ignition of the arc), the delay corresponding to the true breakdown position is given by $\tau_{d,\mathrm{edge}}$. Because $t_{\mathrm{REF},0}$ and $t_{\mathrm{TRA},1}$ are difficult to determine due to non-linear slopes (and noise), a linearization of the problem is useful. The linear slope approximation yields

$$\tau_{d,\mathrm{edge}} = t_{\mathrm{REF}} - t_{\mathrm{TRA}} + \tau_{\mathrm{fill}} \approx t_{\mathrm{REF},0} - t_{\mathrm{TRA},1} + \tau_{\mathrm{fill}}. \tag{30}$$

Using basic trigonometry, one can rewrite Eq. 29 using the fall time $T_{\mathrm{F},p}$, rise time $T_{\mathrm{R},p}$ and Eq. 30:

$$\hat{\tau}_{d,\mathrm{edge}} = \tau_{d,\mathrm{edge}} + \frac{1-p}{2p-1}(T_{\mathrm{R},p} - T_{\mathrm{F},p}). \tag{31}$$

The second term in Eq. 31 represents the estimator bias. The bias term is an estimator itself, firstly because it is based on an approximation and secondly because $T_{\mathrm{F},p}$ and $T_{\mathrm{R},p}$ have to be estimated as well. Therefore

$$\hat{\mathrm{Bias}}(\hat{\tau}_{d,\mathrm{edge}}) = \frac{1-p}{2p-1}(\hat{T}_{\mathrm{R},p} - \hat{T}_{\mathrm{F},p}) = \mathrm{Bias}(\hat{\tau}_{d,\mathrm{edge}}) + \epsilon, \tag{32}$$

where ϵ contains any random estimation and deterministic modeling errors of Eq. 30 - 31. While Eq. 32 is useful for illustrating some of the basic assumptions and limitations of the edge method, it was found unsatisfactory in correcting for the bias in Eq. 29 (see Appendix A).

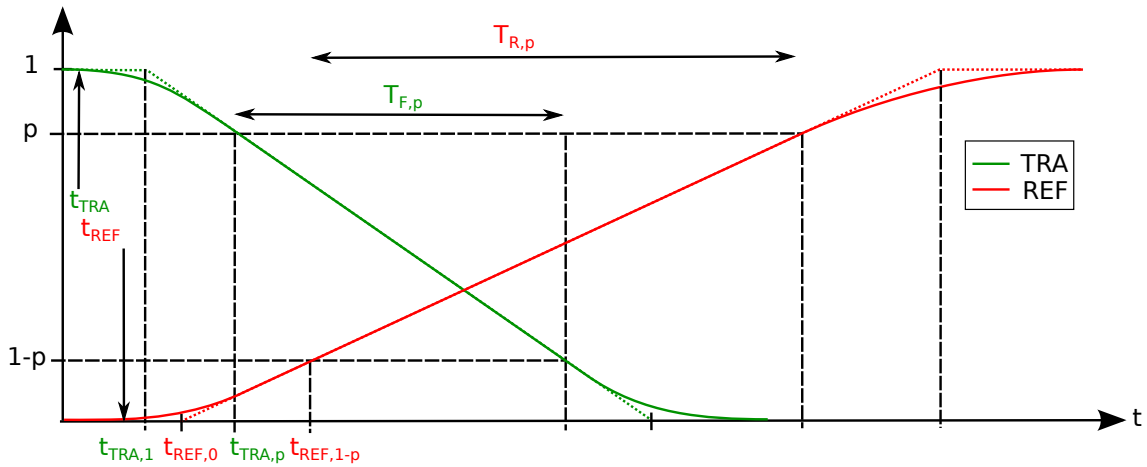

Figure 18: Linear slope model illustrating the effect of edge parameter p on estimation bias.

5.2.2 Correlation method

The high degree of similarity between the tails of the incident and reflected signals (Fig. 16) allows for a robust time delay estimation method. The TDOA may be estimated by minimizing a cost function C (here: the MSE) in the signal tails using a 2D-grid search [6]:

$$(\hat{\tau}_{d,\mathrm{corr2d}}, \hat{a}) = \underset{\tau_d, a}{\operatorname{argmin}}\, C = \underset{\tau_d, a}{\operatorname{argmin}}\, \frac{1}{T} \int_{t_0}^{t_0+T} (\mathrm{INC}(t) - a \cdot \mathrm{REF}(t + \tau_d))^2 \,\mathrm{d}t \qquad (33)$$

Eq. 33 can be visualized as a 2D surface, whose minimum is the point of maximum correlation (Fig. 19). Eq. 33 becomes practical when a and τ_d are discretized and limited to physically feasible values. If the time resolution is considered fixed, the method has five free parameters:

1. The delay search range ($\tau_{d,\min}$ and $\tau_{d,\max}$)
2. The scale search range ($a_{\min}$ and $a_{\max}$)
3. The scale resolution (Δa, i.e. increment of a)
4. The start of the correlation window (t_0)
5. The length of the correlation window (T)

A procedure for selecting the above parameters is given in Appendix B.

Some simple quantities that give an indication of the estimation error of Eq. 33 can be derived. The most obvious one is the minimum value of the cost function:

$$m_\varepsilon = \min C. \qquad (34)$$

A second quantity is the peakedness of the minimum, defined

$$m_{\text{peak}} = 1 - \frac{m_\varepsilon}{\tilde{C}}, \tag{35}$$

where $\tilde{C}$ is the mean cost function of the 2D search grid. Eq. 35 assumes values close to one when the peak is strong with respect to the background, and values close to zero when the peak is weak. A drawback is that the quantity depends on the search grid size.

Another quantity is the relative error of the fit:

$$m_{\varepsilon_\text{r}} = 1 - \frac{\int_{t_0}^{t_0+T} |\text{INC}(t) - \hat{a} \cdot \text{REF}(t + \hat{\tau}_{d,\text{corr2d}})| \, \text{d}t}{\int_{t_0}^{t_0+T} \text{INC}(t) \, \text{d}t} \tag{36}$$

Eq. 36 is a goodness-of-fit measure of the estimate pair $\{\hat{\tau}_{d,\text{corr2d}},\ \hat{a}\}$ that assumes values close to one for good fits.

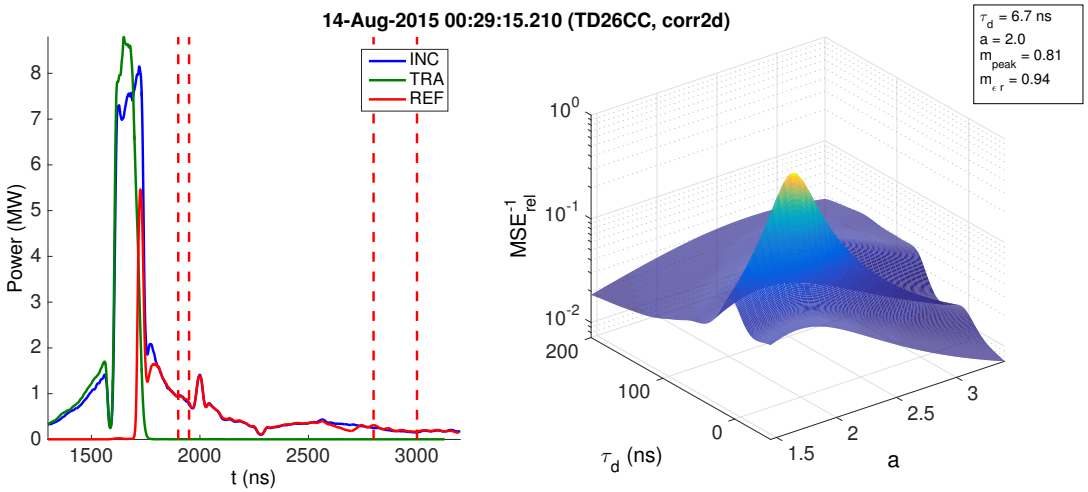

Figure 19: Correlation method. Left: Rescaled and delayed REF and TRA. Dashed vertical lines show correlation windows. Right: Inverse cost function (normalized MSE). MSE is minimized at peak of surface.

It was found that standard cross-correlation (Eq. 12) is sensitive to spurious peaks appearing in one of the signals being correlated, but not the other. The proposed method based on the MSE criterion (Eq. 33) was less sensitive to such peaks. Since the computational load of the method could be kept acceptable, alternatives were not further explored.

5.2.3 Phase

Once the delay between INC and REF has been estimated, the phase difference between the two can be evaluated. The resulting signal represents the phase shift that the RF occurs when traveling through the structure and the waveguide network to the breakdown cell and back (Fig. 15). The phase provides additional information

that can be used to validate position estimates and correct uncertain estimates to within a few neighboring cells.

For a structure with a phase advance per cell of φ, the phase difference $\Delta\theta$ should assume discrete values for breakdowns in regular cells. If a structure has K regular cells and a phase offset θ_0 determined by the RF network between the directional coupler and the first regular cell of the structure, then

$$\Delta\theta = \theta_{\mathrm{REF}} - \theta_{\mathrm{INC}} = 2k\varphi + \theta_0, \;\; k = 1...K. \tag{37}$$

Eq. 37 assumes three different values (when wrapped around 2π) for $\varphi = 2\pi/3$.

Fig. 20 shows the phases of INC and REF aligned with the power signals. After the breakdown onset, the phase difference $\Delta\theta$ drifts towards a stable value $\Delta\theta_{\mathrm{s}}$, which is straightforward to estimate by the windowed sample mean:

$$\Delta\hat{\theta}_{\mathrm{s}} = \frac{1}{N}\sum_{n=n_0}^{n_0+N-1}\Delta\theta(n). \tag{38}$$

In Eq. 38, N is the length of the averaging window starting at sample n_0. A rough measure of the phase difference stability within the window is provided by the unbiased sample standard deviation

$$m_{\mathrm{phase}} = \hat{\sigma}_{\Delta\theta_{\mathrm{s}}} = \sqrt{\frac{1}{N-1}\sum_{n=n_0}^{n_0+N-1}(\Delta\theta(n) - \Delta\theta_{\mathrm{s}})^2}. \tag{39}$$

Eq. 39 is used to discard unstable and thus uncertain estimates of $\Delta\theta_{\mathrm{s}}$ during post-processing.

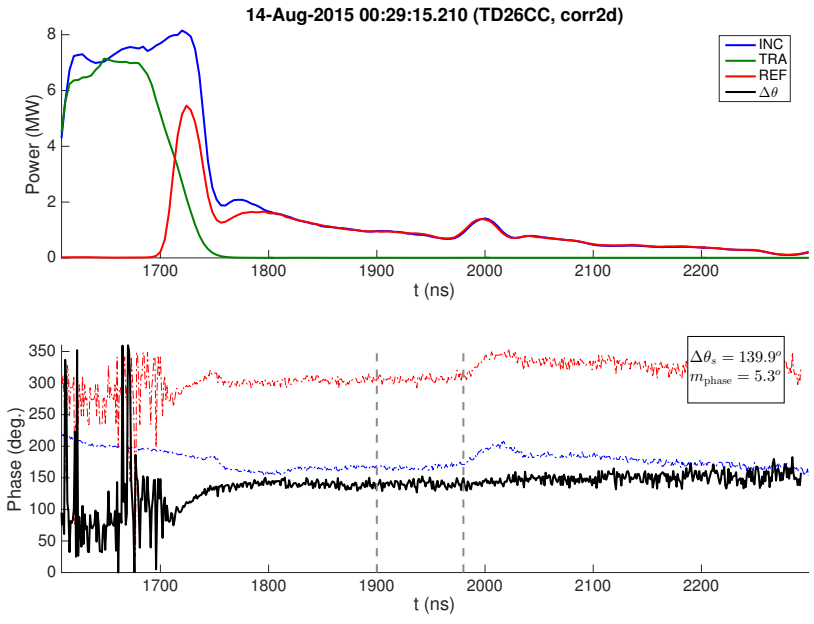

Figure 20: RF power and phase during a typical breakdown. The stable phase difference $\Delta\theta_{\mathrm{s}}$ (in black) is estimated in the window marked by dashed vertical lines.

5.3 Pre-processing

Pre-processing refers to the data manipulation before breakdown position and phase estimation. Depending on the test stand and structure, pre-processing may be necessary for obtaining decent estimation accuracy. The most common pre-processing steps include:

- Cleaning the data of non-breakdown events
- Filtering reflections interfering with the breakdown positioning
- Interpolating the data for improved time resolution.

5.3.1 Discarding non-breakdown events

Breakdown detection needs to be done on a pulse by pulse basis, in order to trigger RF interlocks on breakdowns and limit the amount of data stored. However, due to soft thresholds and various glitches during data acquisition, some non-breakdown events are always saved. Therefore, discarding non-breakdown events before final processing is necessary.

A typical data record of the RF power signals is shown in Fig. 22. The periods of full transmission and zero reflection correspond to non-breakdown pulses. These events can be discarded by applying a threshold on signal energy (U) based criteria

$$m_{\mathrm{TRA}} = \frac{U_{\mathrm{INC}} - U_{\mathrm{TRA}}}{U_{\mathrm{INC}} + U_{\mathrm{TRA}}} \tag{40}$$

$$m_{\mathrm{REF}} = \frac{U_{\mathrm{INC}} + U_{\mathrm{REF}}}{U_{\mathrm{INC}} - U_{\mathrm{REF}}} - 1. \tag{41}$$

The energy of signal P is evaluated over the complete acquisition window of length T, i.e.

$$U_P = \int_0^T P(t)\,\mathrm{d}t. \tag{42}$$

Eq. 40 and 41 approach 0 for non-breakdown events, when the signals are correctly calibrated. Fig. 21 shows the filtering criteria applied to a part of the data in Fig. 22. Fig. 21 shows two distinct data groups, where the group with the smaller variance contains the non-breakdown events. Because the separation between the two data classes is clear in most cases, the filtering thresholds may be set manually. In future work, the classification could be automated using e.g. k-means clustering [54].

Fig. 23 shows the data record after discarding non-breakdown events. The jagged profile of the TRA data record and the non-zero REF suggest that most non-breakdown events were discarded.

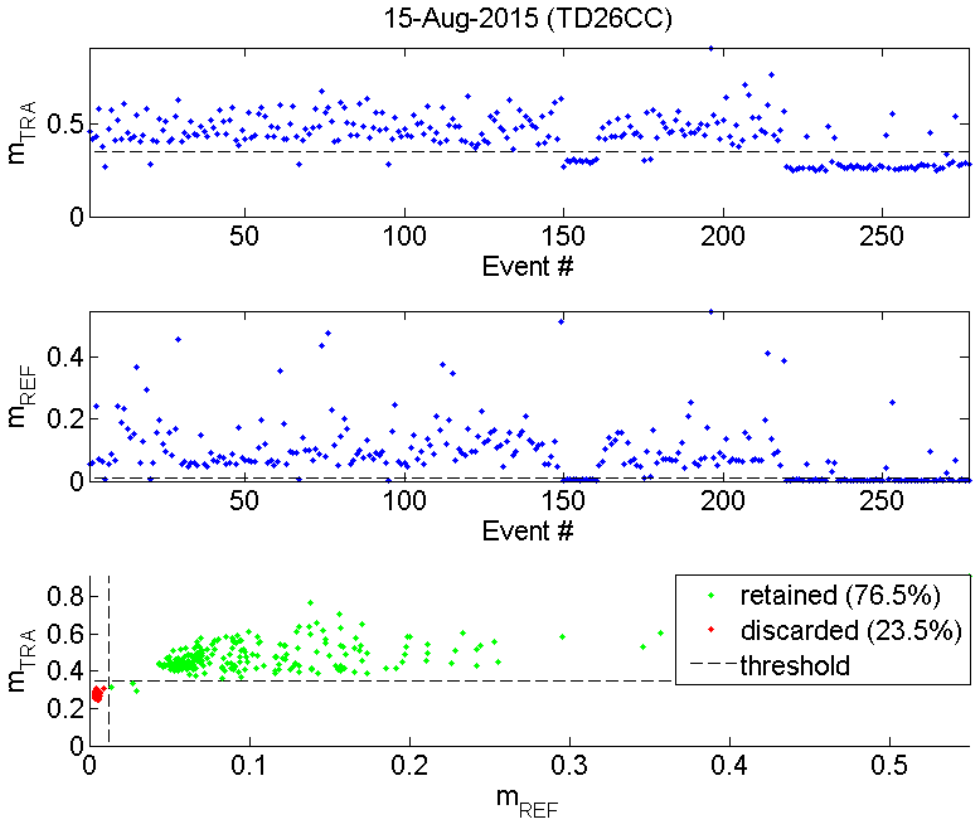

Figure 21: Event classification into breakdown and non-breakdown events (non-breakdown IF $m_{\mathrm{TRA}} \leq 0.35$ AND $m_{\mathrm{REF}} \leq 0.01$). The separation between the two classes is clear.

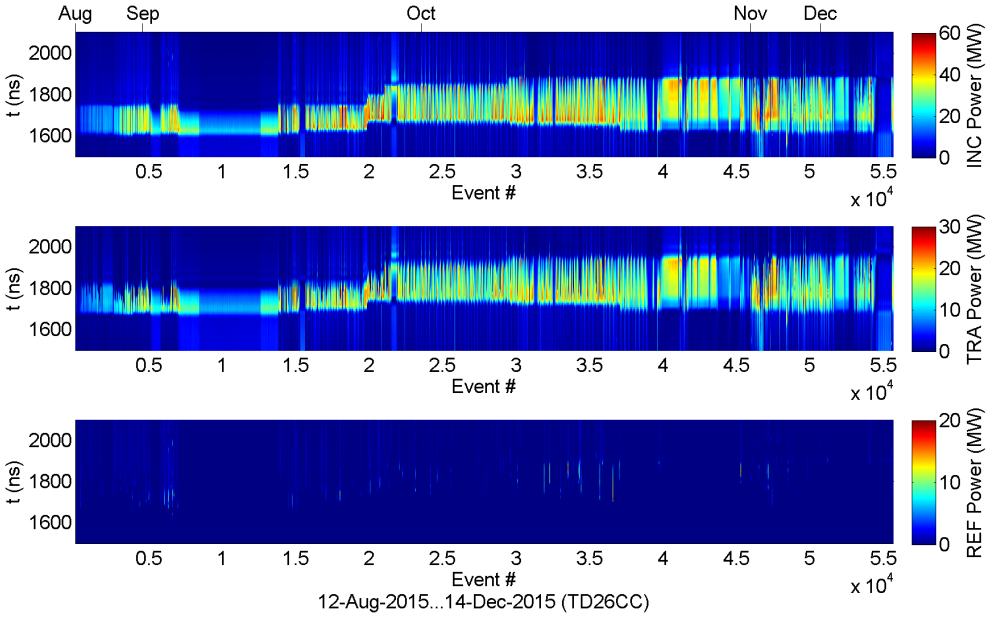

Figure 22: RF power signal record before discarding non-breakdown events. Periods of full transmission and no reflection reveal that the record contains non-breakdown events.

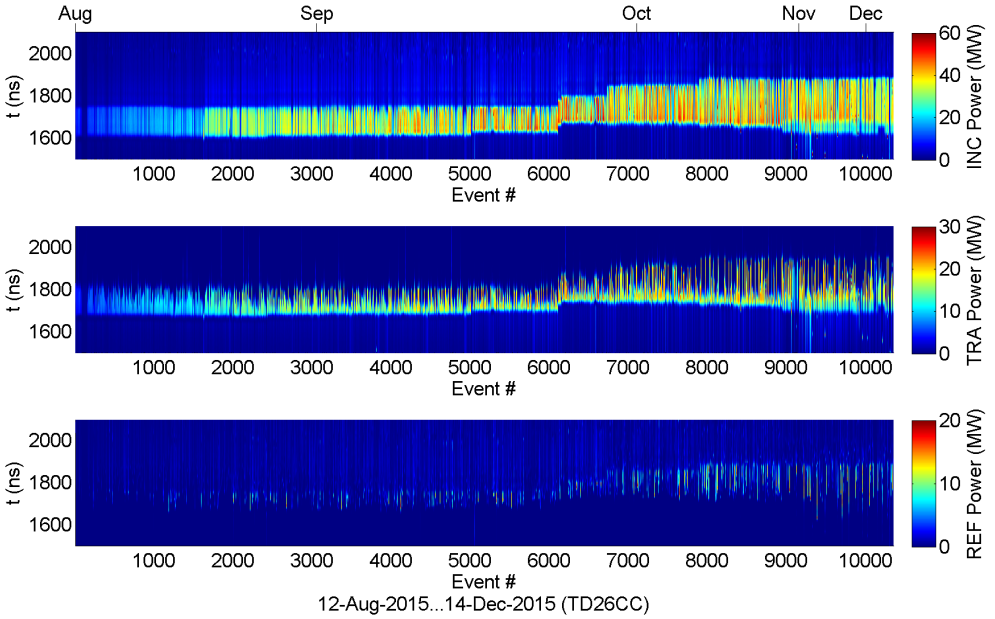

Figure 23: RF power signal record after discarding non-breakdown events. The absence of periods of full transmission and no reflection suggest that most non-breakdown events were successfully discarded.

5.3.2 Filtering interfering reflections

Reflections in the RF network due to impedance mismatches (unrelated to breakdowns) may complicate vacuum arc localization. Usually, if the rising or falling edge of the RF pulse is too fast with respect to the structure's bandwidth, incident RF power is reflected. If the reflection is large enough, it may interfere with finding the rising edge of REF. This is problematic for the edge method. Fortunately, the reflection is mostly is deterministic, provided that the input power remains more or less constant between consecutive pulses. Since the RF signals of the pulse previous to the breakdown are recorded, the deterministic reflections can be filtered by subtraction in the time-domain (Fig. 24). Due to inter-pulse jitter, the breakdown and previous pulse have to be aligned before subtraction. The jitter is estimated by cross-correlating (Eq. 9) the pulse compressor charging pulse of subsequent signals (seen between 100 and 600 ns in Fig. 24). Without pre-alignment, sharp transients at misaligned edges may dominate the filtered signal.

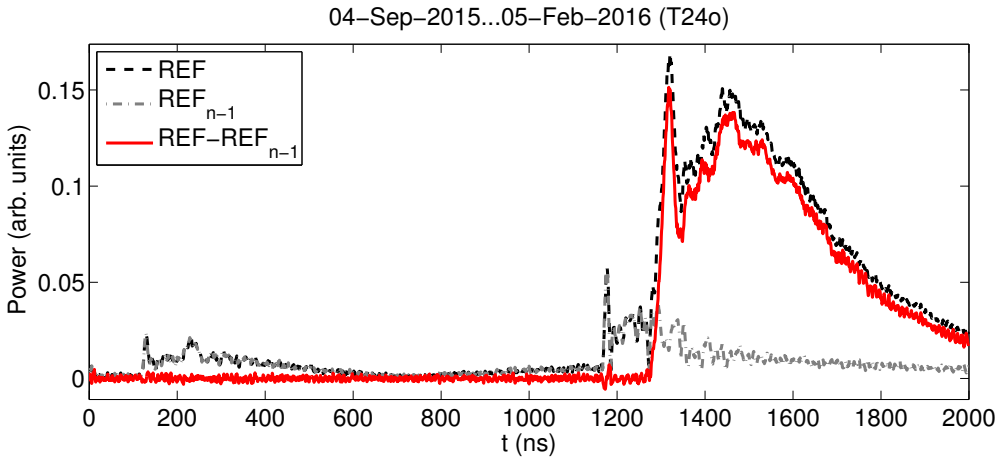

Figure 24: Reflected RF power before (REF) and after (REF–REF$_{n-1}$) subtracting the previous pulse (REF$_{n-1}$). Non-breakdown related reflections are successfully removed.

5.3.3 Upsampling

In order to improve the time resolution of the localization methods, the log-detector signals are upsampled by a factor 6. This increases the nominal time resolution from 4 to 0.67 ns, which is close to the 0.63 ns of the IQ signals.

5.4 Post-processing

Post-processing refers to the non-destructive operations applied to estimate data after the pre-processing and estimation steps. Typical post-processing steps are e.g. discarding uncertain estimates and converting the estimated time delays into longitudinal positions or cell numbers.

5.4.1 Discarding uncertain estimates

Uncertain breakdown position and phase estimates can be discarded by imposing thresholds on the filtering criteria defined in Eq. 35, 36 and 39. An estimate is considered uncertain if the distance of a filtering criterion to the ideal value of an error free estimate is large. The criteria of Eq. 35, 36 and 39 obtain values 1, 1 and 0 for ideal estimates. In this thesis, the thresholds were found by trial and error, so that a predetermined percentage (typically 40-60 %) of the data was retained after filtering. In future work, the filtering process could be made more systematic by first specifying a percentile of the data to be retained and then automatically calculating the threshold, based on the distribution of the filtering criterion in question.

Fig. 25 shows an example of values assumed by the criteria for a typical set of time delay and phase estimates. The retained and discarded estimates are shown in Fig. 26. An event is retained if it passes all of the imposed thresholds (AND operation). Fig. 26 is less cluttered when uncertain events are not included, although obviously not all unphysical estimates are caught by the filtering process. Unphysical estimates are outside of the expected range of time delay or phase values, i.e. $\tau_d \notin [0 \ldots 2\tau_{\text{fill}}]$ or $\Delta\theta_s \notin [0,\ 2\pi/3,\ 4\pi/3] + \theta_0$. By setting tighter thresholds, one may reduce unphysical estimates at the risk of biasing the distribution of the retained events (Fig. 26 (b)).

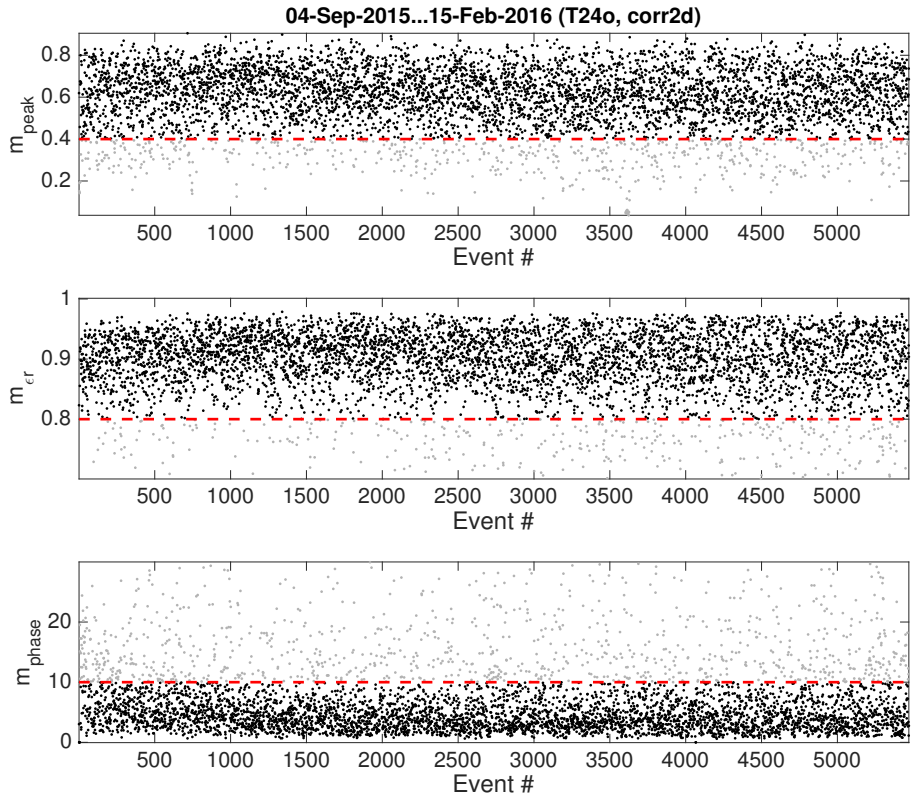

Figure 25: Example of discarding uncertain estimates (retained events in dark). An event is retained IF $m_{\text{peak}} \geq 0.4$ AND $m_{\epsilon_r} \geq 0.8$ AND $m_{\text{phase}} \leq 10^o$.

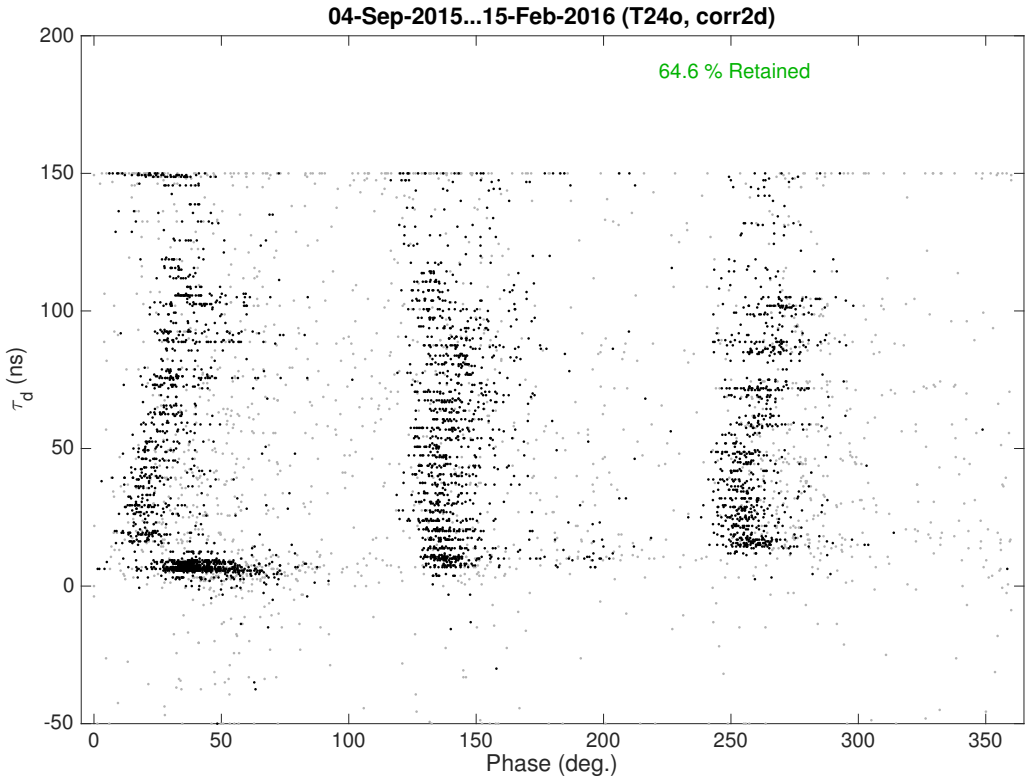

(a) Relaxed thresholds ($m_{\text{peak}} \geq 0.4,\ \ m_{\epsilon_r} \geq 0.8,\ \ m_{\text{phase}} \leq 10^o$).

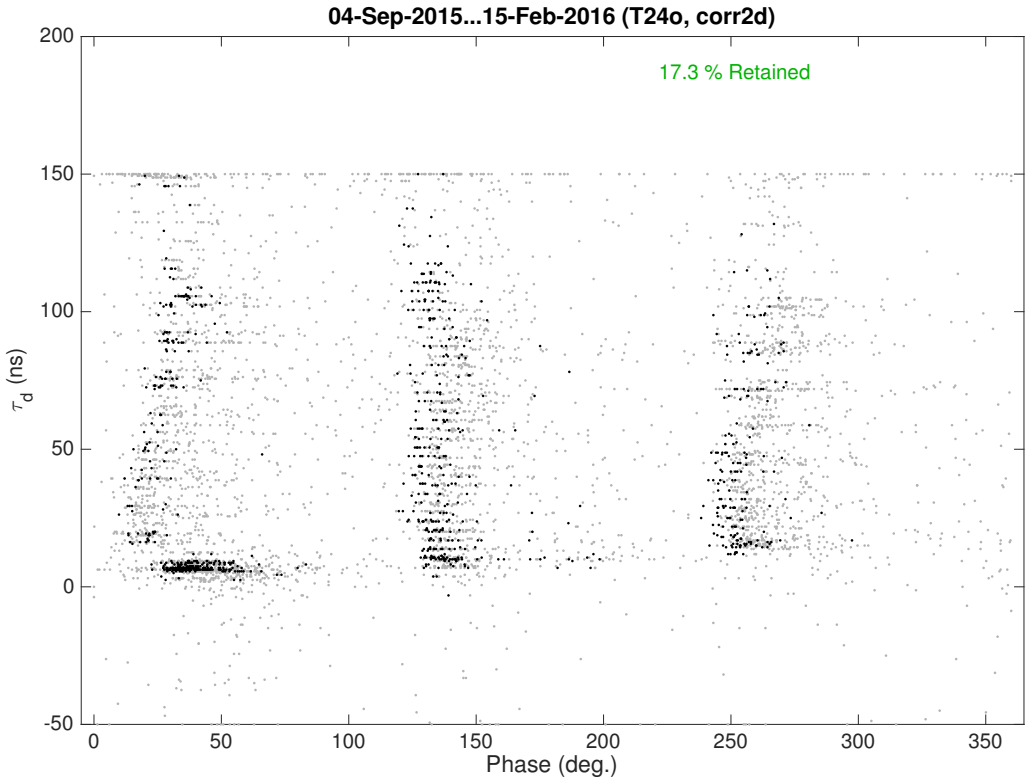

(b) Tight thresholds ($m_{\text{peak}} \geq 0.7,\ \ m_{\epsilon_r} \geq 0.9,\ \ m_{\text{phase}} \leq 5^o$).

Figure 26: Breakdown position and phase scatter plot using (a) relaxed and (b) tight filtering thresholds for discarding uncertain events (retained events in dark). Tight thresholds may bias the distribution.

5.4.2 Time delay to position conversion

The relationship between breakdown position and time delay is illustrated in Fig. 27. Given the round-trip time τ_{RT} and the group velocity profile of the structure $v_g(z)$, the longitudinal breakdown position z_{BD} can be solved from

$$\tau_{\mathrm{RT}} = 2\int_0^{z_{\mathrm{BD}}} \frac{1}{v_g(z)}\,\mathrm{d}z. \tag{43}$$

Time delay and position are used interchangeably in this work, although strictly speaking Eq. 43 states that $\tau_{\mathrm{RT}} \propto z_{\mathrm{BD}}$ only when v_g is constant (i.e. does not depend on z). However, it is reasonable to refrain from time-delay-to-position (or cell) conversion, when time resolution is inadequate for distinguishing between breakdowns in the coupling and normal cells. This is very much the case here, since v_g transitions between $\mathcal{O}(c)$ in the waveguide network to $\mathcal{O}(0.01c)$ in the structure. Furthermore, the interpretation of the breakdown cell becomes sensitive to any uncertainty in the time offset τ_0 (see Fig. 15), which contains non-breakdown related delays due to signal propagation, acquisition and estimator bias.

The time delay, estimated using Eq. 30 or Eq. 33, should fulfill $\tau_d \in [0\ 2\tau_{\mathrm{fill}}] + \tau_0$. For a typical constant gradient structure with uniform longitudinal breakdown position distribution, half the number of breakdowns are expected at $\tau_d \approx 2\tau_{\mathrm{fill}}$ compared to $\tau_d \approx 0$ (see Appendix C).

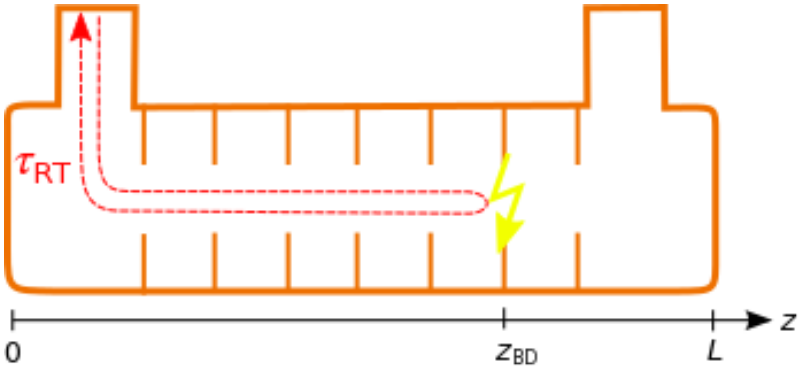

Figure 27: Relationship between breakdown position z_{BD} and measured round-trip time τ_{RT}.

6 Results

In this section, the breakdown localization results during the high-power tests of the T24, T24 open, TD26CC and CLIC Crab Cavity are presented. All four structures went through a similar conditioning process, where power and pulse length were gradually increased, while keeping a constant or decreasing BDR of $\mathcal{O}(10^{-5})$ breakdowns/pulse. In general, CLIC accelerating structures are conditioned until they reach the nominal accelerating gradient of 100 MV/m.

Vacuum arc localization in the structures under such high-power tests has two main applications:

1. Structure diagnostics
2. Vacuum arc studies.

In section 6.1, the breakdown position history of the tested structures is presented and the obtained position distributions are qualitatively compared to the theoretically expected distributions. In section 6.2, the breakdown positioning accuracy of the correlation and edge methods is estimated. In the concluding section 6.3, new evidence of two vacuum arc phenomena is presented: breakdown migration and spatio-temporal correlation of consecutive breakdowns.

6.1 Structure diagnostics

The spatial breakdown distribution can provide valuable information about the condition of a structure. Usually, the distribution is constantly monitored, so that decisions regarding future operation can be made immediately. This allows fast adaptation to changing conditions in case of any operational issues.

A central concern during high-power testing is the formation of a *hot cell* [4, 5]. A hot cell is a concentrated accumulation of breakdowns in a small area (usually an iris). Repeated breakdowns in the same spot degrades the structure and causes local field enhancement, which leads to further spatial breakdown clustering. A hot cell could also occur due to contamination, as was the case in [5], where an aluminum sliver found its way into a structure.

The spatial breakdown distribution has been observed to have an approximately linear field dependence [38], although the overall breakdown probability of a structure follows a power law (Eq. 27). Breakdown localization is essential for understanding this discrepancy, which is one of the important motivations for this work.

6.1.1 TD26CC

Fig. 28 shows the breakdown time delay evolution and distribution in the TD26CC from August to December 2015. For visualization purposes, position estimates are displayed in order of occurrence along an index number abscissa. During August, breakdowns were concentrated towards the end of the structure. The accumulation seems to have disappeared during conditioning. As a consequence, the distribution after August is in agreement with the uniform spatial distribution assumed of an

unloaded constant-gradient structure (see Appendix C). High-power testing of the structure was scheduled to resume in February 2016.

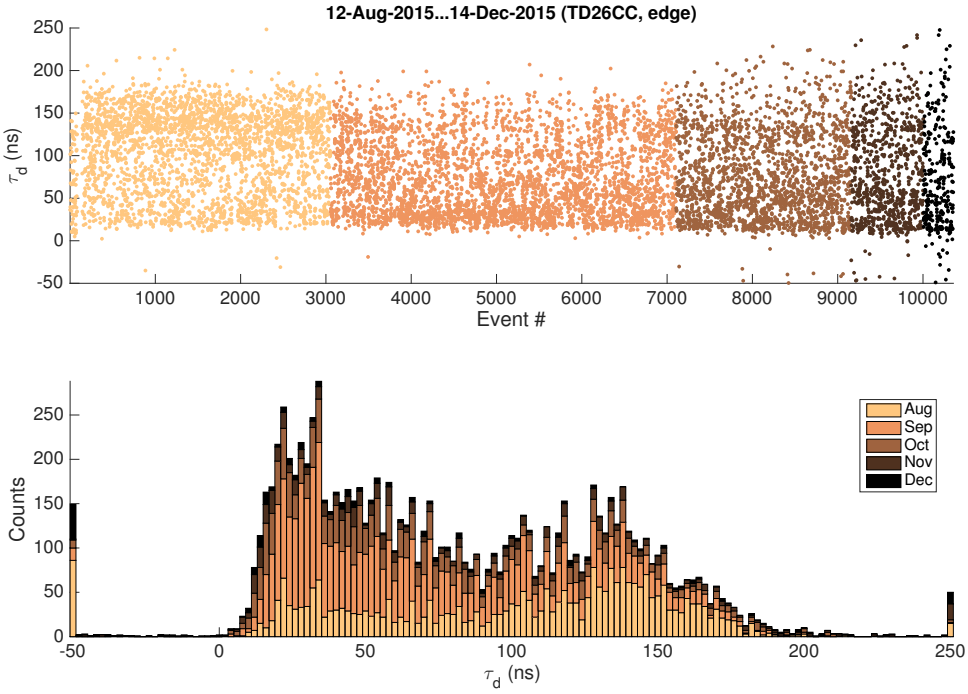

Figure 28: Breakdown time delay distribution (TD26CC, edge method). The uniformity of the distribution indicates normal constant gradient structure behavior.

Fig. 29 shows a density plot of the phase difference trajectories calculated using Eq. 37. The plot is essentially a sliding-window histogram, obtained by overlaying the phase trajectories (black curve in Fig. 20) of all breakdowns between August and December 2015. Fig. 29 displays three distinct phases separated by 120^o, as is expected of a $2\pi/3$ phase advance structure. Based on Fig. 29, the stable phase window of Eq. 38 is selected between 1600 and 1680 ns.

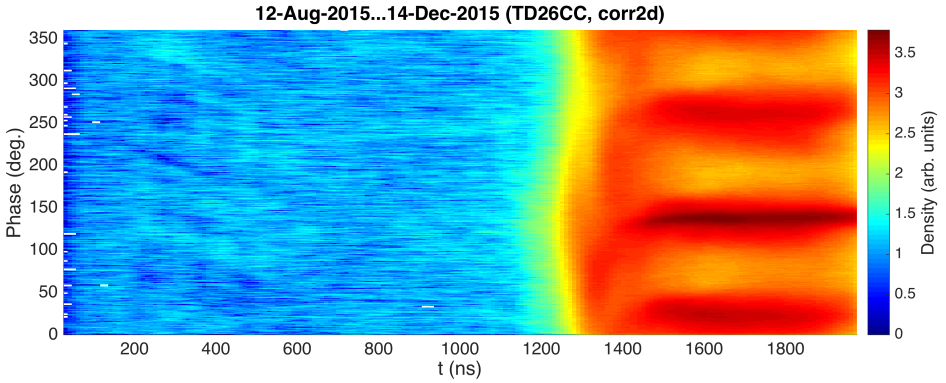

Figure 29: Density plot of phase difference trajectories (TD26CC, correlation method). Three distinct phases are expected of a $2\pi/3$ phase advance structure.

Fig. 30 shows the breakdown phase difference plotted against time delay. The green rectangles represent the cell edges calculated from the group velocity profile in Fig. 62. After adjusting the vertical and horizontal offset of the cell grid and discarding uncertain estimates, the results show agreement with expected results, as most of the estimates fall within the cell boundaries. Fig. 30 does however display two unexpected features. Firstly, the three phase trajectories are not vertical, but slightly tilted. This may be due to cell detuning and the consequent accumulation of phase error in *downstream* breakdowns, i.e. breakdowns towards the output of the structure. Secondly, estimates are better clustered *upstream* (towards the input) than downstream, even if the cell group delay (height of the green rectangles) grows downstream. The effect is unlikely a consequence of attenuation, as log-detectors have a wide dynamical range. Although the exact cause remains to be confirmed, a reasonable explanation is structure related signal dispersion. Dispersion would, similarly to the phase error, accumulate and distort the reflected signal the more, the further downstream the breakdown occurred.

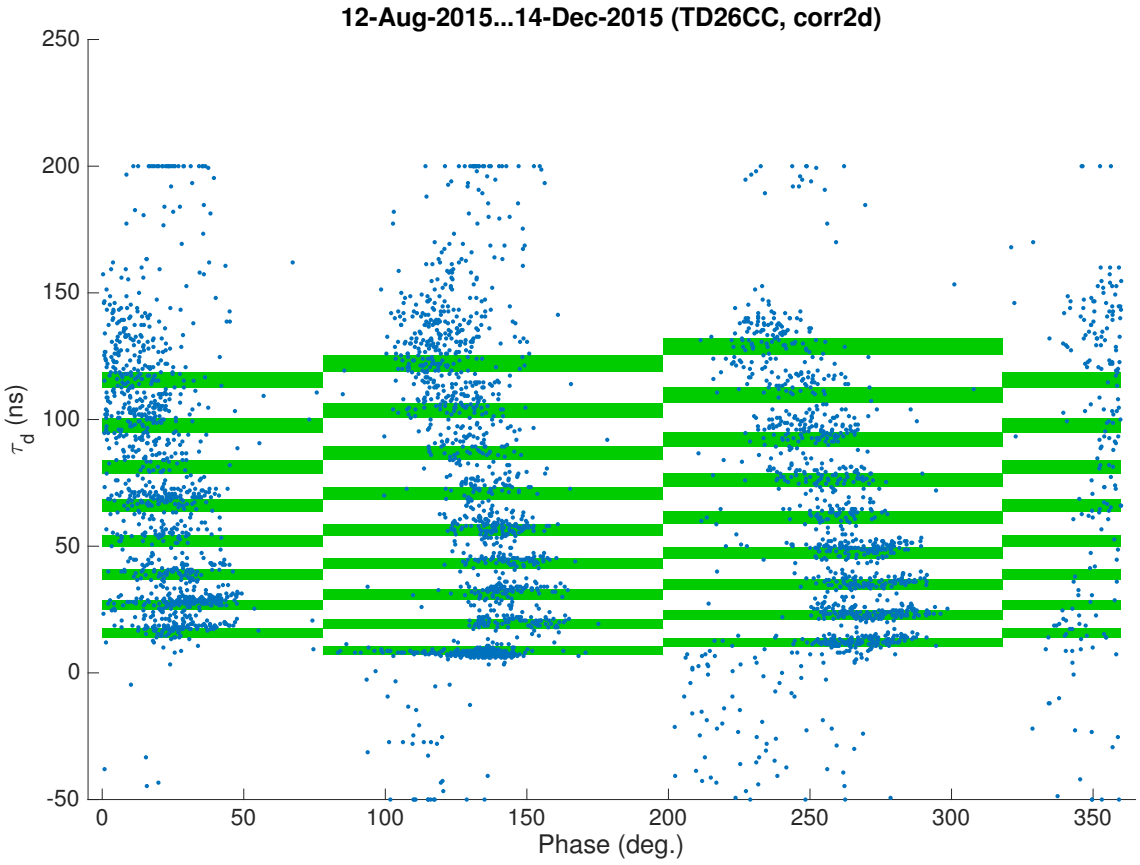

Figure 30: Breakdown phase difference vs. time delay (TD26CC, correlation method). Events are mostly clustered in the cell bins (green rectangles), as expected. 42% of events retained after filtering ($m_{\text{phase}} \leq 10^o$, $m_{\text{peak}} \geq 0.6$, $m_{\epsilon_r} \geq 0.8$).

6.1.2 CLIC Crab Cavity

The time delay distribution of breakdowns in the CLIC Crab Cavity (high-power tested from October 2014 to June 2015) is shown in Fig. 31. Practically all the breakdowns are clustered in the beginning of the structure, which according to Eq. 22 is expected of a constant impedance structure. The phase difference distribution in Fig. 31 shows a single strong peak, which confirms that most of the breakdowns indeed occur in a single cell. Additionally, a post-mortem analysis of the Crab Cavity (Fig. 33) showed that the number of breakdown craters rapidly decrease after the coupling and first normal cell on the RF input side [51]. The abrupt shift of the distribution in Fig. 32 is due to an offset in the calibration of one of the phase channels.

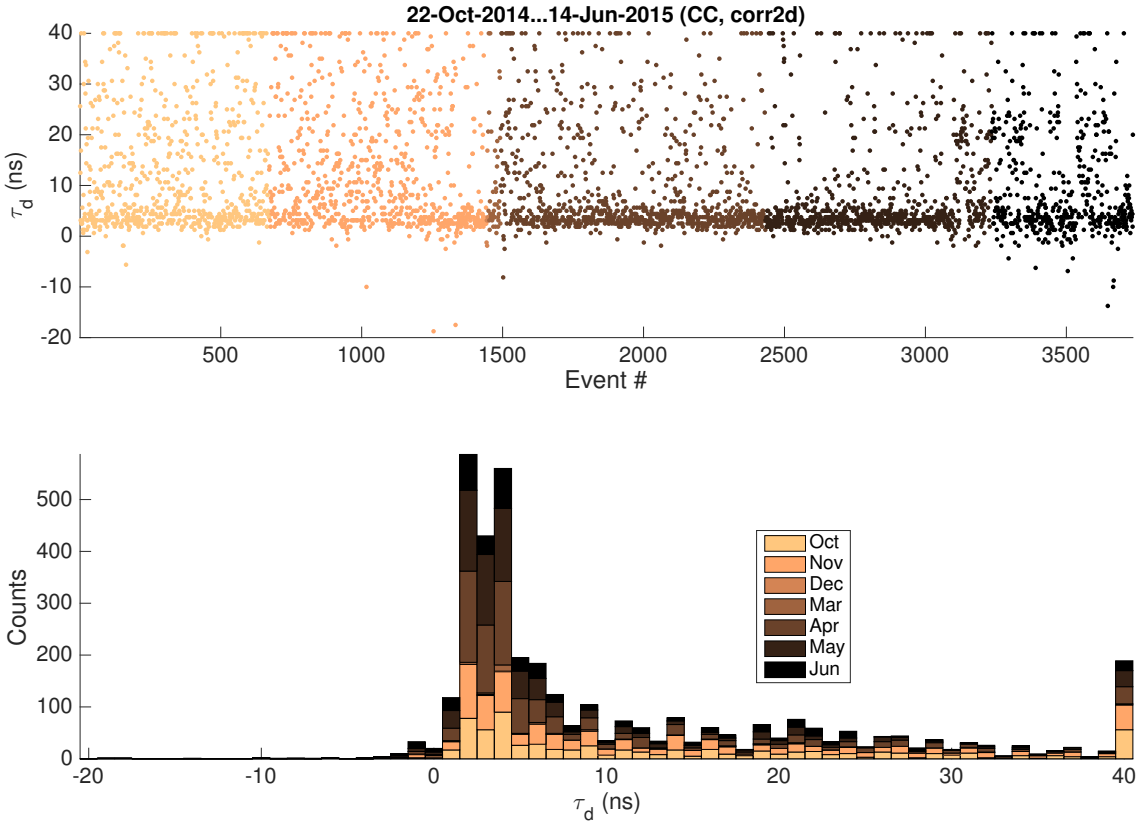

Figure 31: Breakdown time delay distribution (CLIC Crab Cavity, correlation method). The skewness of the distribution towards the RF input indicates normal constant impedance structure behavior. 60% of events retained after filtering ($m_{\text{peak}} \geq 0.4$, $m_{\epsilon_r} \geq 0.9$).

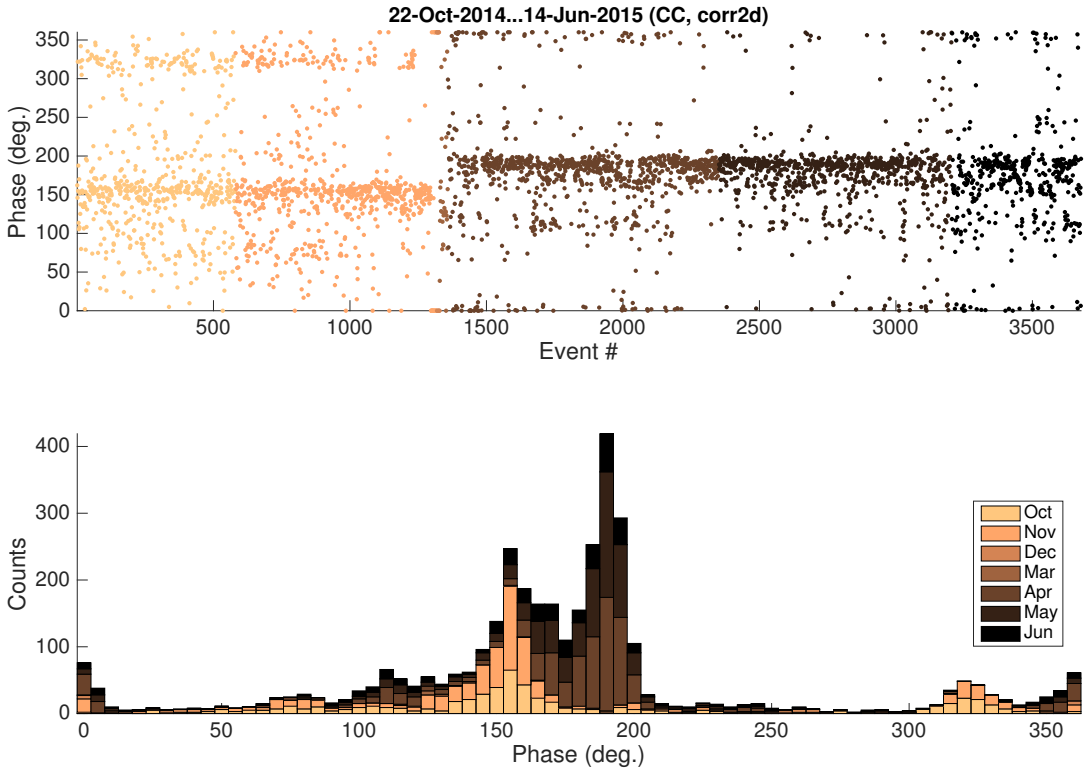

Figure 32: Breakdown phase difference distribution (CLIC Crab cavity, correlation method). The single strong phase component suggests that most breakdowns indeed occur in one cell. 59 % of the events retained after filtering ($m_{\text{phase}} \leq 3^o$).

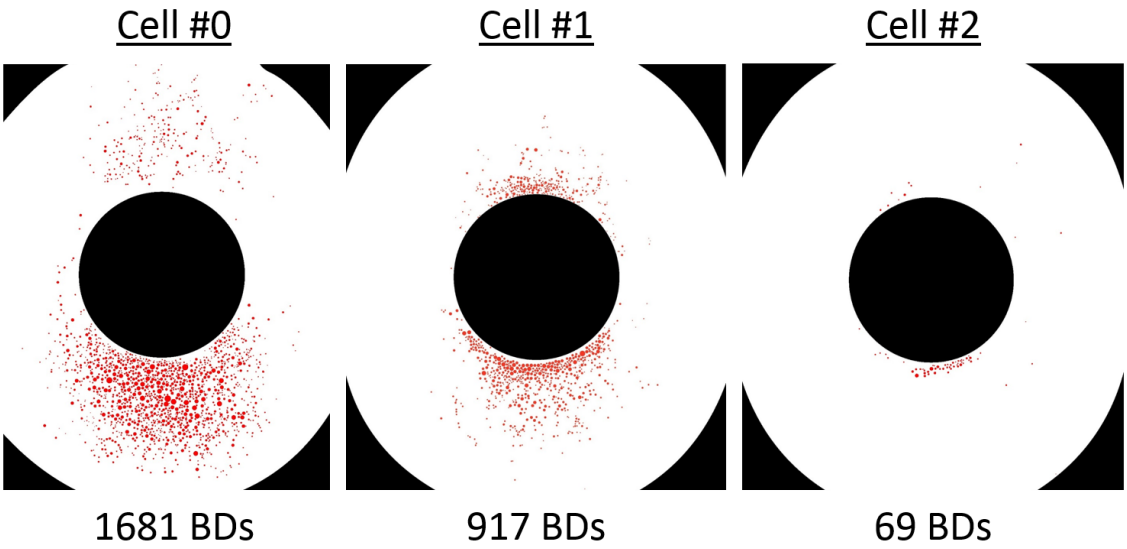

Figure 33: CLIC Crab cavity crater distribution from post-mortem analysis of the the first three RF input side cell walls [51]. The abruptly decaying number of craters is consistent with Fig. 31 and 32.

6.1.3 T24

Fig. 34 shows the evolution of the breakdown time delay distribution in the T24 from July 2014 to May 2015. The distribution is fairly uniform, until a hot cell develops in September 2014. This coincides with the onset of beam loading, which appears to have damaged the structure. The hot cell is confirmed by the evolution of the phase difference shown in Fig. 35. Furthermore, Fig. 36 shows the BDR and BDR* (Eq. 28) wildly oscillating and ultimately increasing after the appearance of the hot cell. This suggests that the structure had indeed been degraded by the beam. Because a flat spatial breakdown distribution under unloaded conditions is essential for the Dogleg experiment, the structure had to be changed for the experiment to continue as planned. In May 2015 the T24 was replaced by the TD26CC, which had gone through conditioning in an earlier test in 2013 [28].

The breakdowns towards the end of the structure in March 2015 were due to a brief *anti-loading* period. During anti-loading, the beam is injected in decelerating phase. This causes power to be deposited to the traveling RF wave along the whole length of the structure, which increases the likelihood of downstream breakdowns.

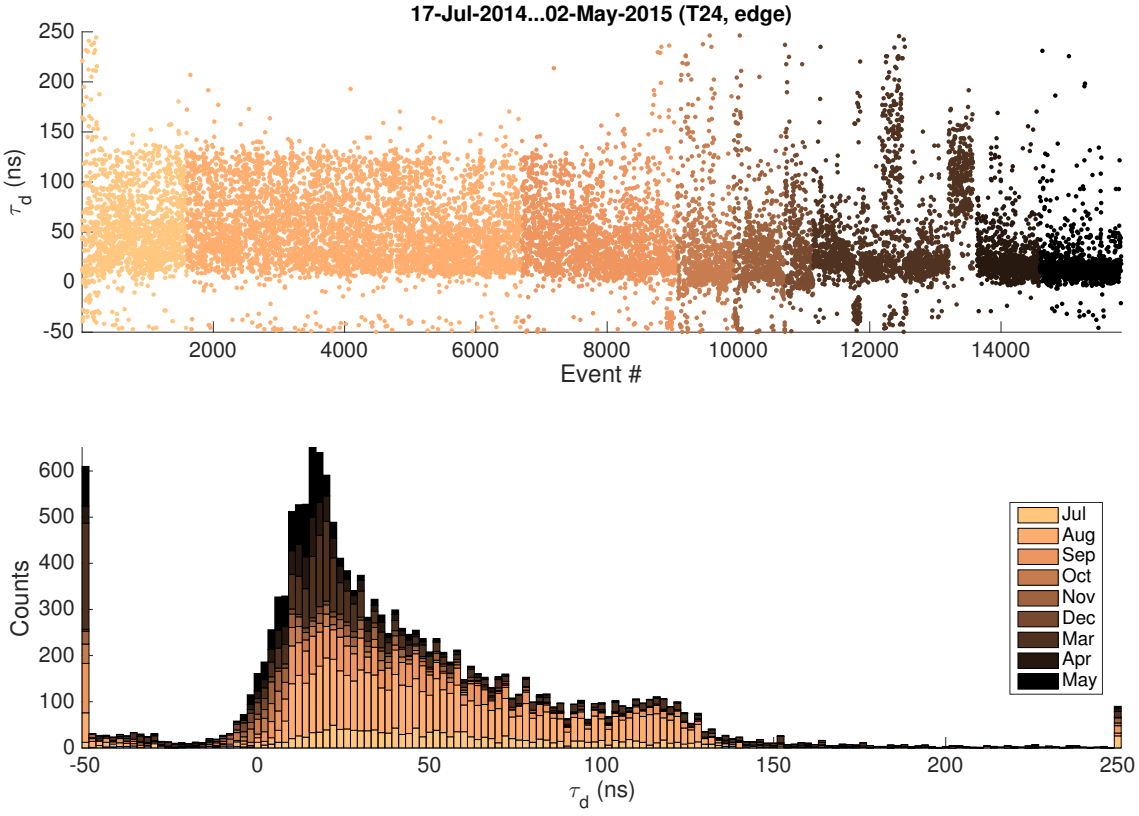

Figure 34: Breakdown time delay distribution (T24, edge method). A hot cell unexpectedly started developing during September.

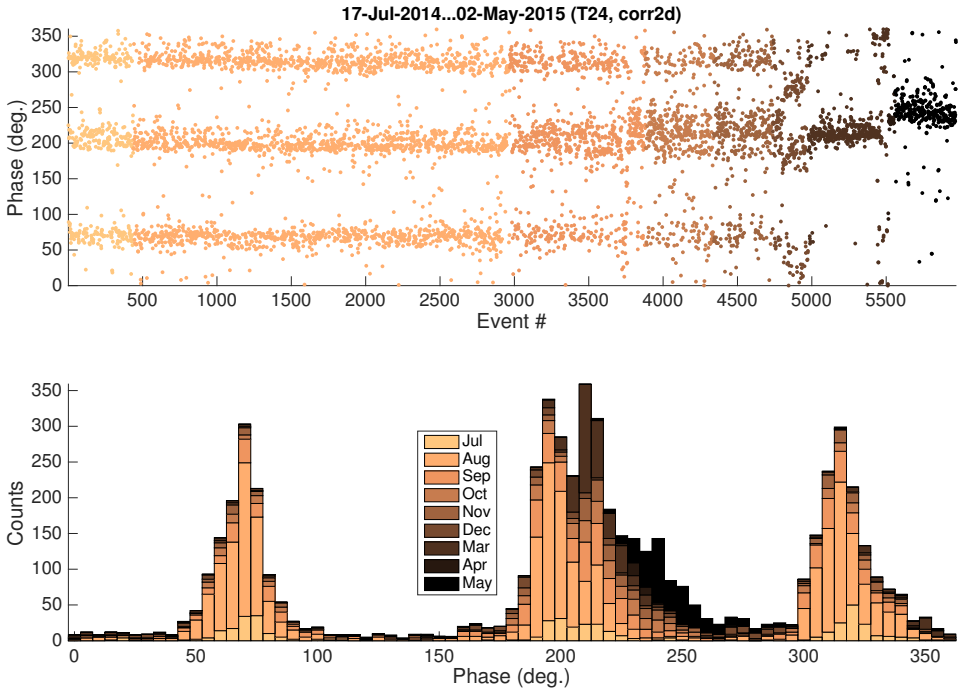

Figure 35: Breakdown phase difference distribution (T24, correlation method). The hot cell is confirmed by the shift from three phase trajectories (normal operation) to one (hot cell). 38 % of the events retained after filtering ($m_{\text{phase}} \leq 10^o$).

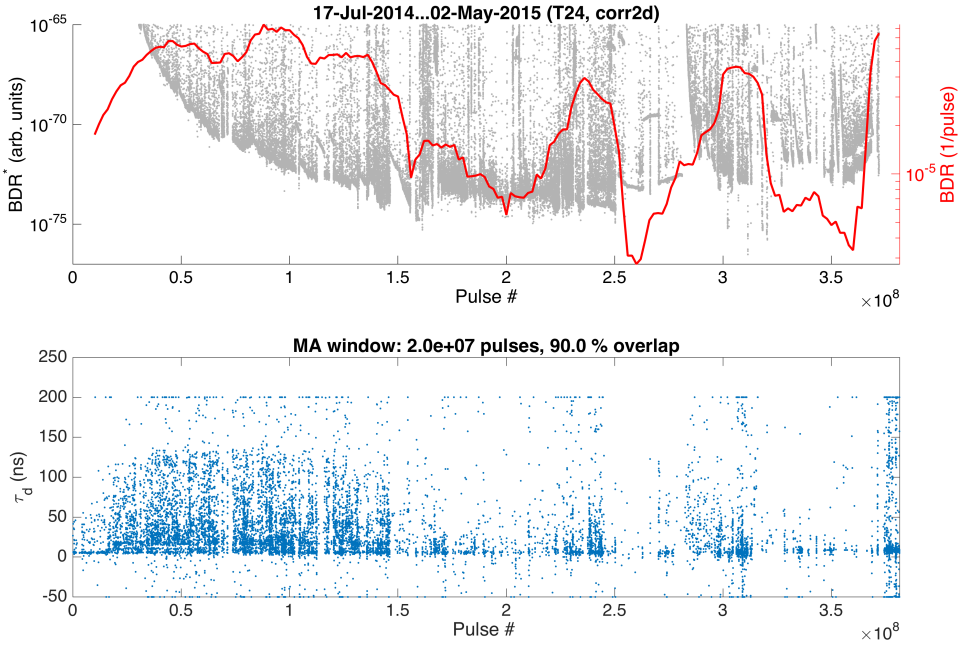

Figure 36: Breakdown rate and time delay estimates (T24, correlation method). The oscillating BDR during the hot cell period indicates structure degradation.

6.1.4 T24 open

Fig. 37 shows the T24 open breakdown time delay evolution from September 2015 to February 2016. The structure operated as expected until mid-November, when a hot cell developed. The hot cell is also apparent in the phase distribution, shown in Fig. 38. Fig. 39 reveals that the hot cell appeared when the pulse length was increased from 90 to 160 ns. The decreasing BDR and BDR*, shown in Fig. 40, suggest that the structure was still conditioning despite the hot cell.

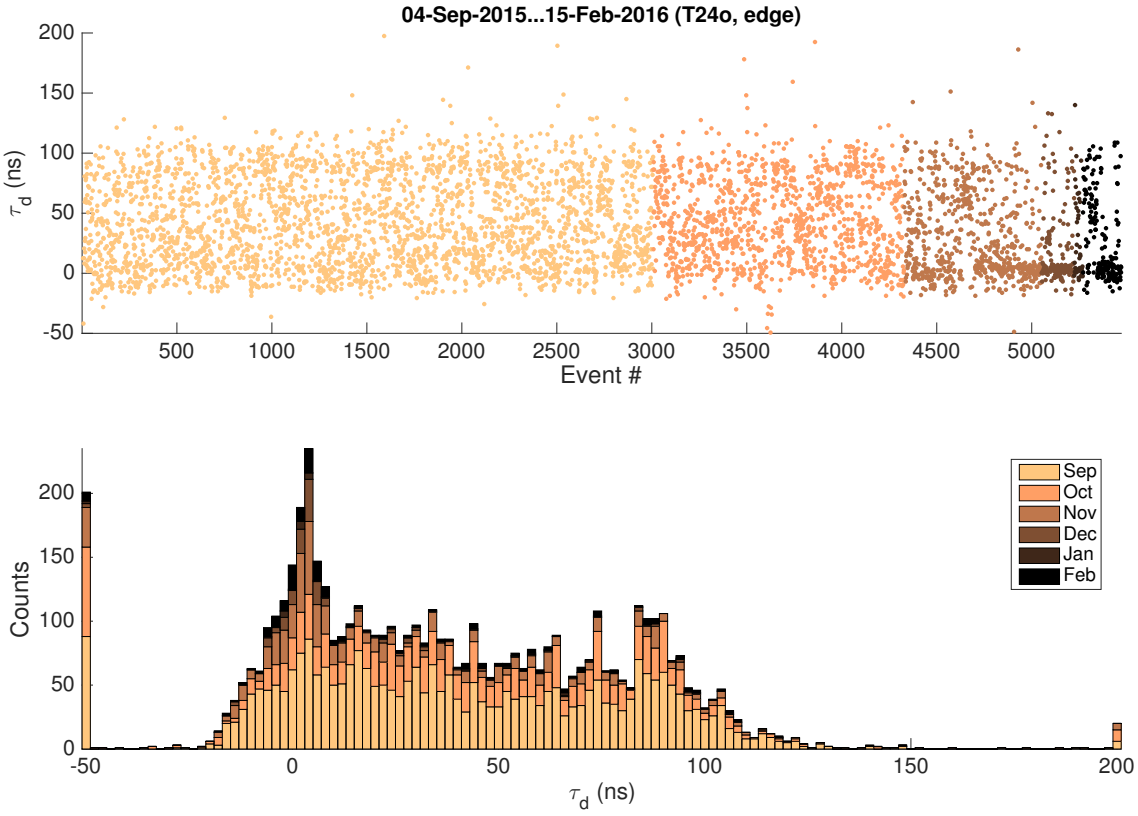

Figure 37: Breakdown time delay distribution (T24 open, edge method). A hot cell unexpectedly started developing during November.

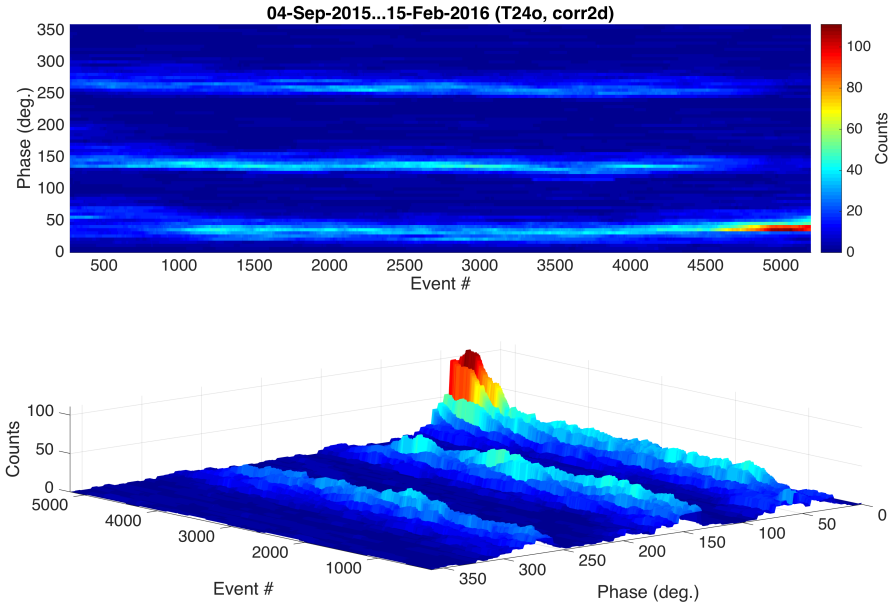

Figure 38: Breakdown phase difference distribution (T24 open, correlation method). The hot cell is confirmed by the shift from three phase trajectories to one.

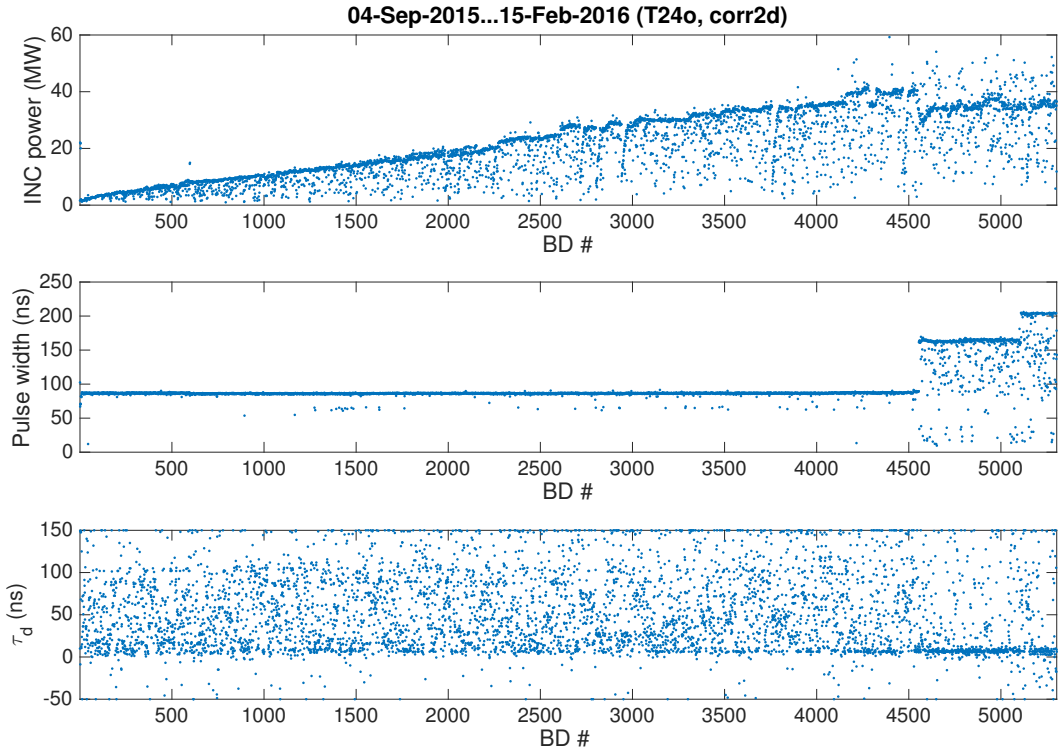

Figure 39: Power, pulse length and breakdown time delay estimates (T24 open, correlation method). The hot cell coincides with a change in pulse length.

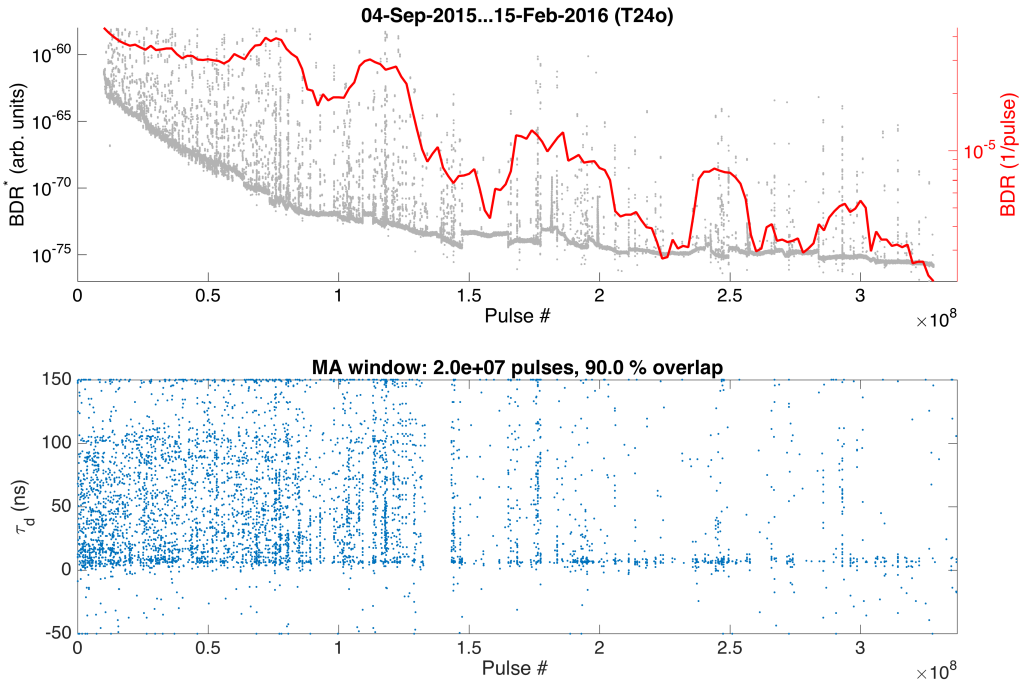

Figure 40: Breakdown rate and time delay estimates (T24 open, correlation method). The decreasing BDR means that the structure is conditioning despite the hot cell.

6.1.5 Summary

In conclusion, the TD26CC and CLIC Crab Cavity performed as anticipated during the whole observation period, whereas the T24 and T24 open eventually developed hot cells in the front of the structures, albeit for different reasons. The hot cell in the T24 coincided with the onset of beam loading experiments, whereas the trigger for the T24 open seemed to be a change in RF pulse length. The conditioning behavior of the two hot structures was also somewhat different. In the T24, the BDR fluctuated wildly compared to the T24 open, which still seemed to be conditioning at the time of writing.

6.2 Localization precision

Assuming that breakdowns during a hot cell period occur in the same position, the precision of the localization methods can be roughly estimated. Fig. 41 and 42 show empirical probability density functions and *cumulative distribution functions* (CDFs) of the edge and correlation methods during hot periods in Xbox-1 and 2 (see Fig. 34 and 37). It is not obvious whether the PDFs fit any widely known distribution. More specifically, neither seem to be adequately described by Gaussian statistics.

In order to robustly measure the spread of the estimates, a precision quantity ς

is defined

$$\varsigma = x_p - x_{p-1}, \tag{44}$$

where x_p and x_{1-p} are the p^{th} and $1-p^{\text{th}}$ data percentiles. If $p = 0.84$, then

$$\Pr(X \leq x_p) - \Pr(X \leq x_{1-p}) = \Pr(X \leq x_{0.84}) - \Pr(X \leq x_{0.16}) = 0.68. \tag{45}$$

The value of p in Eq. 45 is chosen such that if x is normally distributed, its standard deviation $\sigma = \frac{\varsigma}{2}$ according to Eq. 44. In other words, 68 % of the data lie within in a region of length ς. In the case of a normally distributed random variable, this corresponds to a distance of 2σ ($\pm 1\sigma$ from the mean).

Using the definitions of Eq. 44 and 45, the spread of the correlation method is found to be $3-4$ ns. The corresponding value for the edge method is $10-13$ ns. Comparing these values to the cell group delays calculated in Table 1, one may conclude that the spatial resolution of the correlation method close to the RF input is roughly one cell. In the case of the edge method, the corresponding precision is $3-4$ cells. This is in agreement with Fig. 30, which displays a clear grouping of events in the upstream cells. On the other hand, Fig. 30 suggests that the precision is actually worse downstream, although the relative time resolution per cell is better (see section 6.1.1). Therefore, the estimates of the positioning precision might only be valid for upstream breakdowns. It should also be mentioned that the failure of the edge method in the case of the CLIC Crab Cavity (Fig. 43) is due to the the poor resolution of the method, combined with the short group delay of the structure ($5-6$ cells spatial resolution in a 10 cell structure).

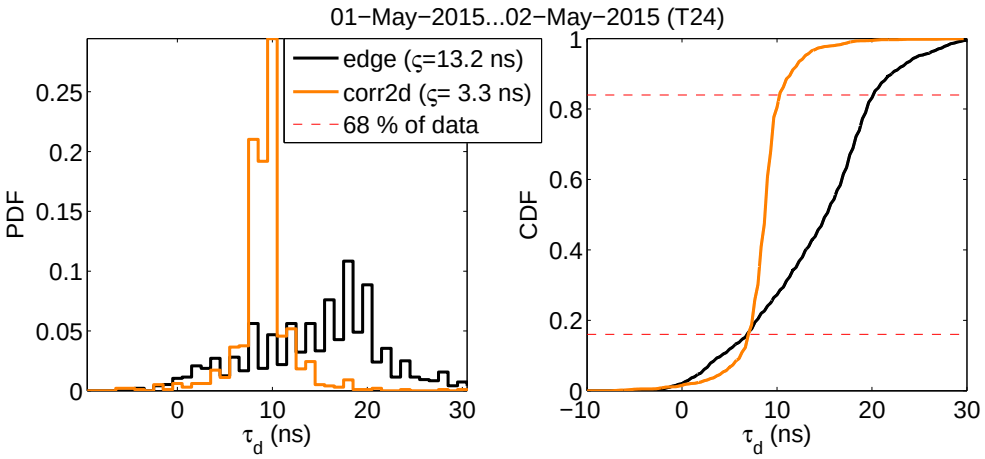

Figure 41: Empirical time delay PDF and CDF during a hot-cell period in Xbox-1 ($\approx$ 970 breakdowns). The precision estimated from the CDF is $\approx$ 3 ns for the correlation and $\approx$ 13 ns for the edge method.

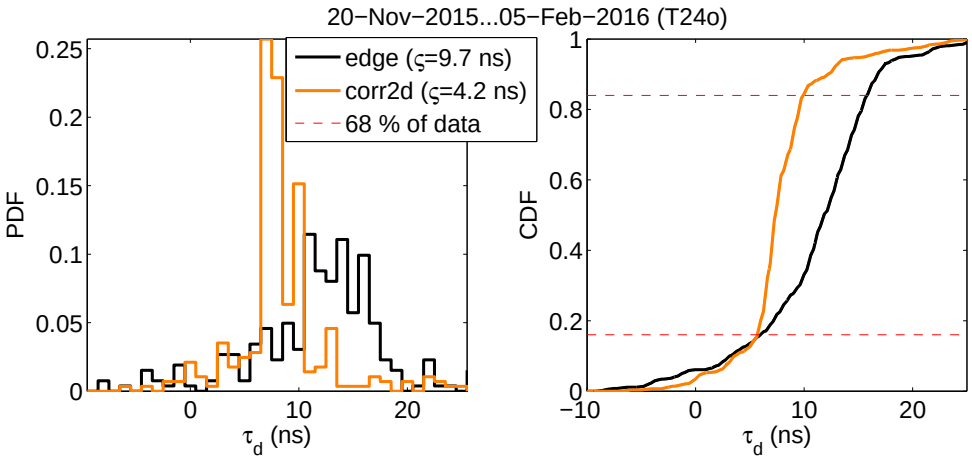

Figure 42: Empirical PDF and CDF during a hot-cell period in Xbox-2 ($\approx$ 280 breakdowns). The precision estimated from the CDF is $\approx$ 4 ns for the correlation and $\approx$ 10 ns for the edge method.

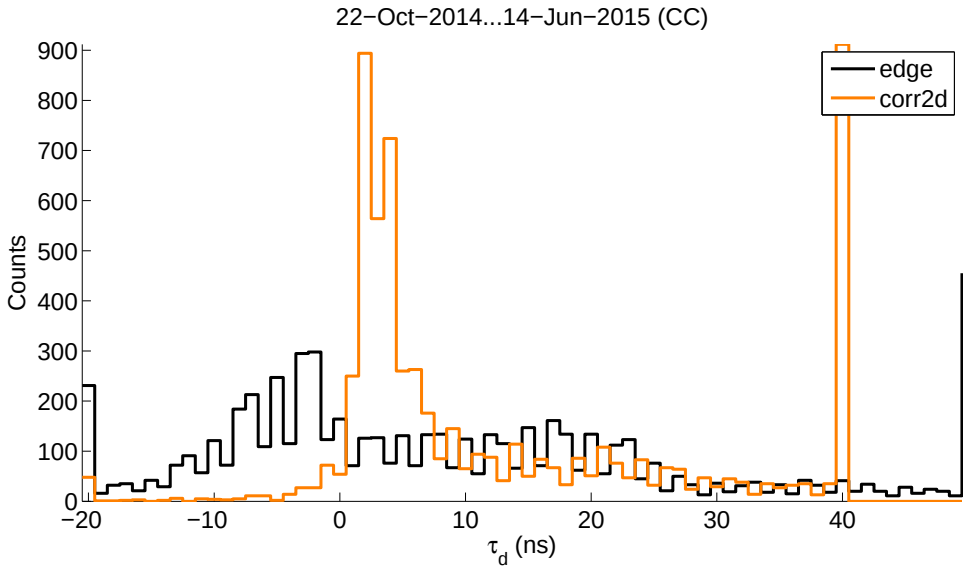

Figure 43: Breakdown position histograms (CLIC Crab Cavity). The edge method performs poorly because of the short group delay of the structure and the low precision of the method.

6.3 Vacuum arc studies

It should be pointed out that only one breakdown position distribution per structure was shown in section 6.1. In other words, results obtained solely by either the edge or the correlation method were given and any minor differences between the two methods were not discussed. From the point of view of structure diagnostics, a qualitative agreement between the methods is enough, since the general shape of

the position distribution is of main interest. However, a more careful comparison of the methods reveals details that are intriguing from a physics point of view. Section 6.3.1 explores a discrepancy between the edge and correlation methods, which is hypothesized to be a manifestation of breakdown migration.

In the section 6.3.2, another vacuum arc phenomenon is studied. It is shown that the breakdown inter-arrival time and position are correlated, which demonstrates the memory effect of the breakdown process.

6.3.1 Breakdown migration

Fig. 44 shows a scatter plot of edge and correlation method time delay estimates. Generally, the methods are in good agreement and estimates fall on a diagonal line, as expected. Nevertheless, the correlation method is more likely to yield estimates further upstream than the edge method, as can be seen from the non-symmetric distribution in Fig. 45. In particular, the very front of the structure is more populated by the correlation method (Fig. 46).

The bias of the edge method is likely to explain the offset, but not the assymetry of the distribution in Fig. 45. Furthermore, Fig. 47 shows that in many cases the discrepancy between the methods persists although both estimates seem reasonable. An explanation fitting these observations is *breakdown migration* [32, 48, 55]. If the onset of a breakdown is found by the edge method and the final steady-state position by the correlation method, then Fig. 44 is consistent with breakdowns migrating upstream in the structure. The edge and correlation methods detect features in the data separated by $\mathcal{O}(100$ ns), which is a plausible timescale for migration, given breakdown turn-on times of $\mathcal{O}(10$ ns) measured in [29, 44]. Downstream breakdown migration is unlikely, as little or no power is available downstream after an arc starts reflecting incident RF power. Conversely, migration upstream is possible because power and fields are still present there. Furthermore, constructive interference between incident and reflected RF power might cause local field enhancement upstream of the breakdown.

A final observation supporting the migration hypothesis is provided by the RF phase. After the onset of some breakdowns (Fig. 48), the phase difference fluctuates for $\mathcal{O}(10$ ns) before reaching a stable value. The reflected power also sometimes oscillates together with the phase difference during the breakdown onset. A possible explanation is sketched in Fig. 49. The hypothesis proposed in [55] is that the arc absorbs, but does not reflect incident power temporarily while migrating. The absorption causes a dip in reflection, right before the arc re-establishes itself at a new location.

Although the evidence in support of the breakdown migration hypothesis presented in this section was obtained from the TD26CC, similar features were also observed in the data of the T24 and T24 open.

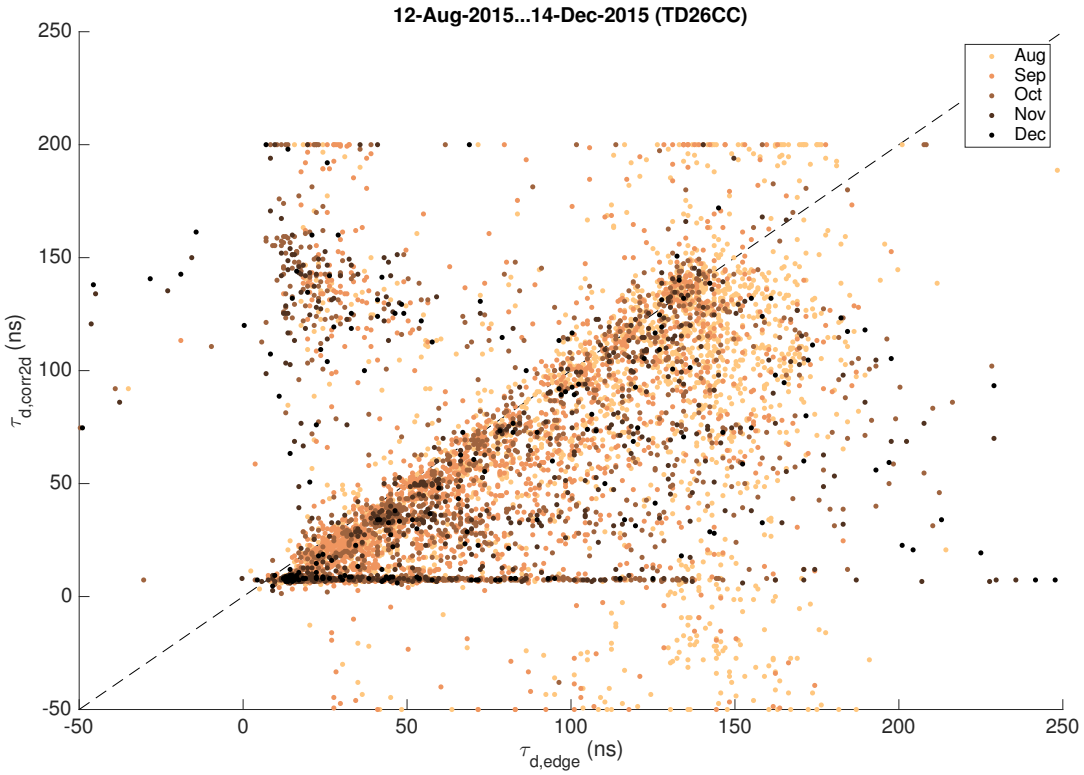

Figure 44: Scatter plot of edge and correlation method breakdown time delay estimates (TD26CC). Although the two estimators often agree (estimates on the diagonal line) the edge method has a tendency to yield estimates further downstream than the correlation method (heavily populated lower right triangle). 59 % of events retained after filtering ($m_{\text{peak}} \geq 0.6$, $m_{\epsilon_r} \geq 0.8$).

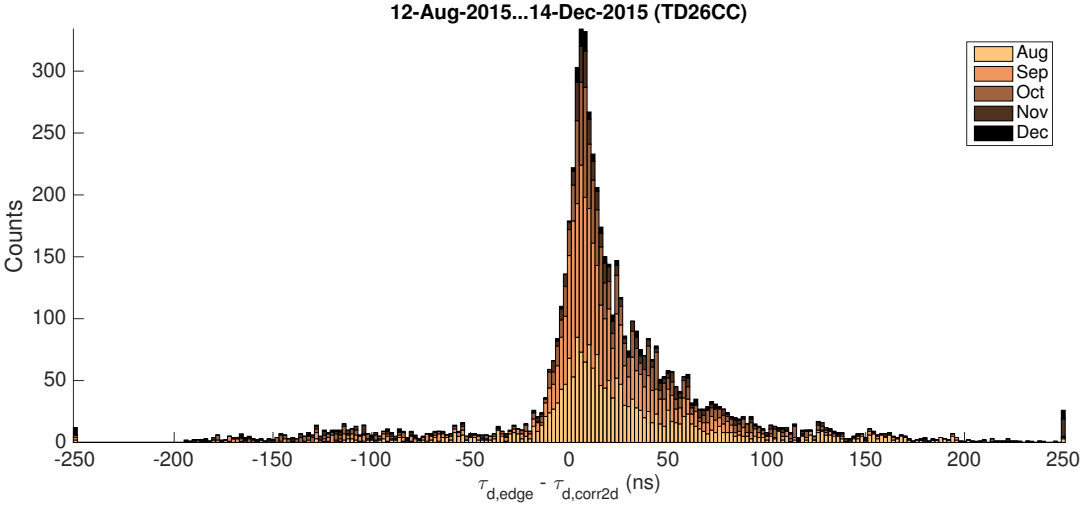

Figure 45: Distribution of time delay estimate difference between edge and correlation method (TD26CC). The skewness is consistent with upstream breakdown migration. 59 % of events retained after filtering ($m_{\text{peak}} \geq 0.6$, $m_{\epsilon_r} \geq 0.8$).

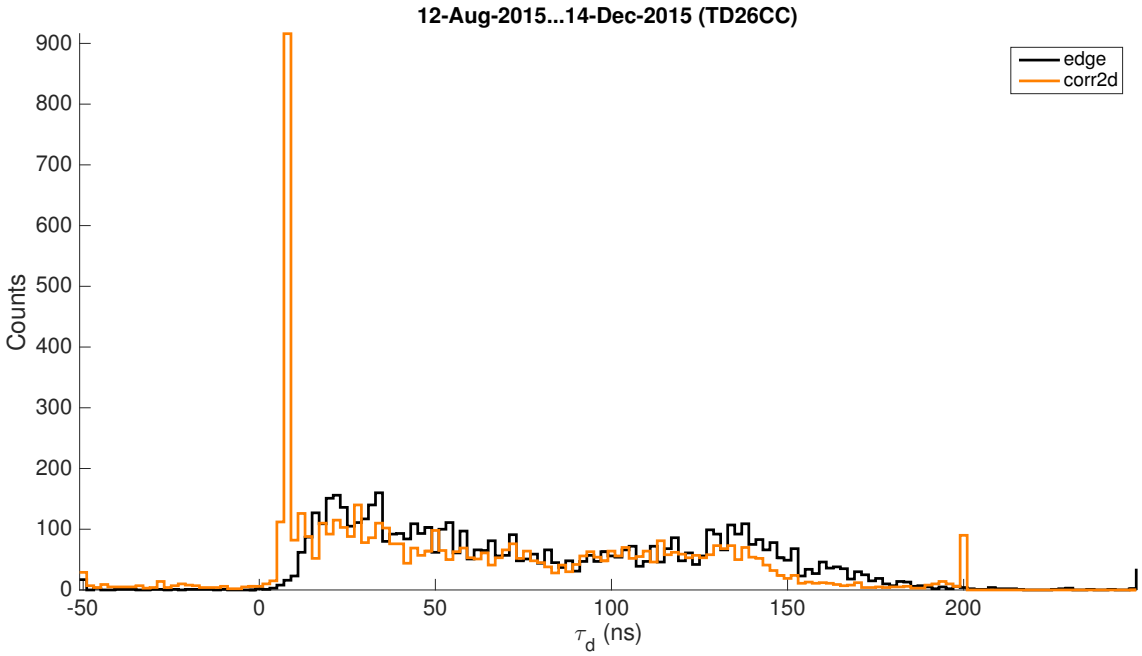

Figure 46: Breakdown time delay distributions of the two methods (TD26CC). The distributions are in good agreement, apart from the peak of the correlation method, which suggests that most breakdowns migrate to the RF input. 59 % of the events retained after filtering ($m_{\text{peak}} \geq 0.6$, $m_{\epsilon_r} \geq 0.8$).

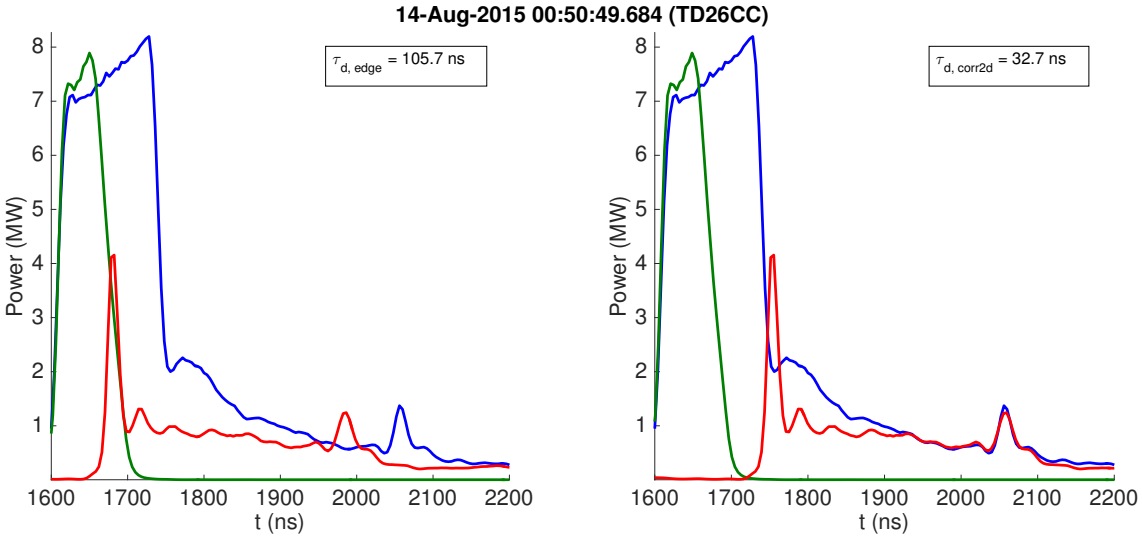

Figure 47: Discrepancy in time delay estimates of the two methods (TD26CC). This could be explained by the breakdown migrating upstream after its onset (found by the edge method) to its final position (found by correlation method). Left: edge method. Right: correlation method.

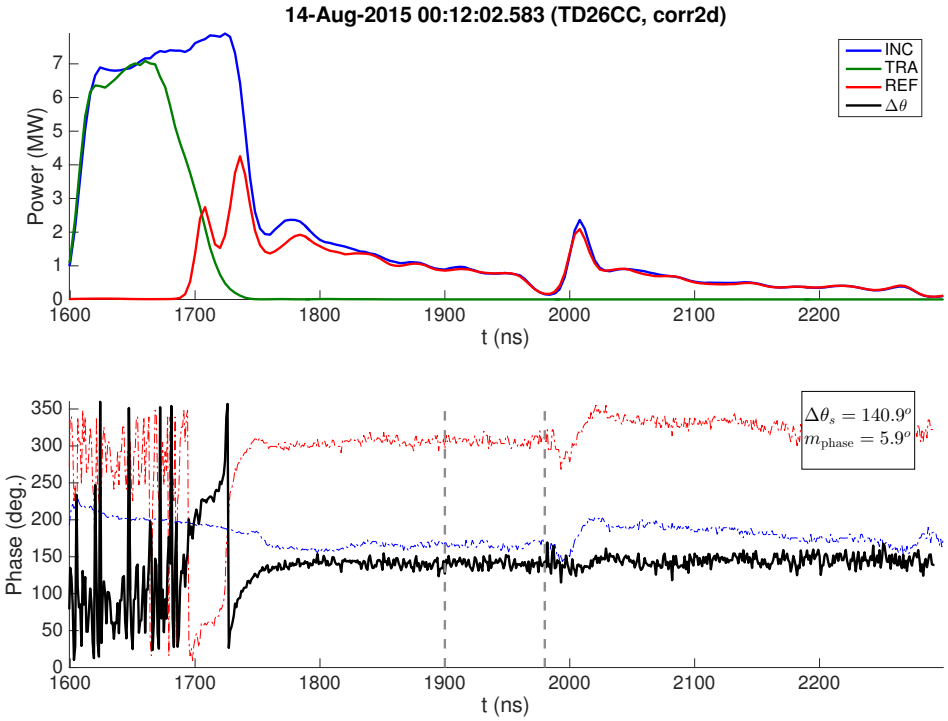

Figure 48: Breakdown with unstable onset (TD26CC, correlation method). Fluctuations in the phase difference and REF power that occasionally occur together are be explained by migration (see Fig. 49).

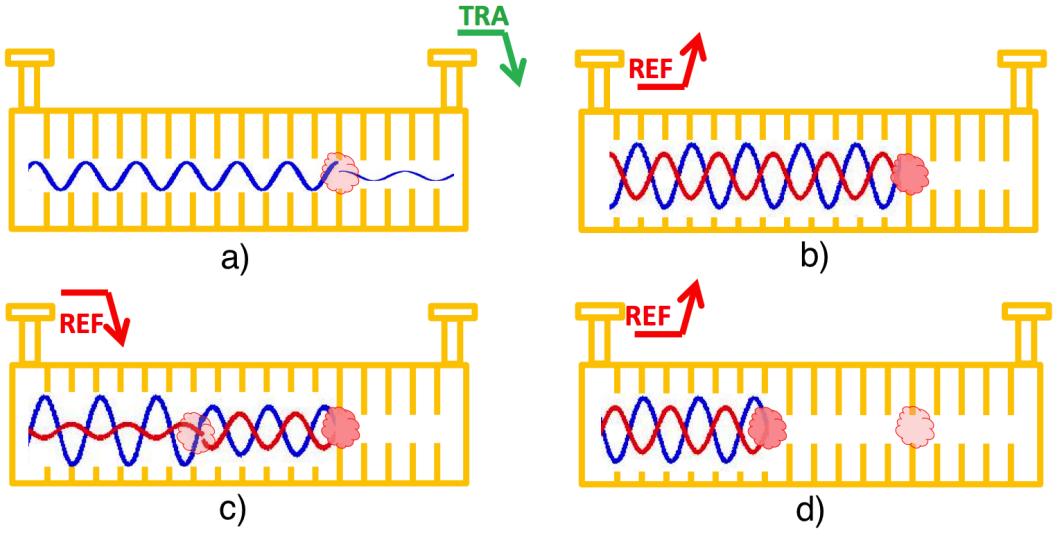

Figure 49: Breakdown migration scenario [55]. a) An arc establishes itself in the structure and starts absorbing incident RF power. b) After the arc has developed it reflects all incident power. c) Constructive interference between the incident and reflected waves causes another arc to form upstream. d) As the second arc develops, any remaining power downstream is drained and the first arc is extinguished.

6.3.2 Spatio-temporal correlation of breakdowns

Recent RF and DC experiments have revealed that conditioning is a non-Poissonian process [31]. In particular, it has been observed that breakdown inter-arrival times are not exponentially distributed. Rather, the inter-arrival time distribution, shown in Fig. 50, seems to be better described by two superimposed exponential distributions. This could be explained by two different underlying breakdown rates, where the tail distribution corresponds to a base rate of primary breakdowns and the early distribution corresponds to follow-up, or clustered breakdowns [31]. Furthermore, the breakdown process displays self-similarity at different time scales, which is seen in e.g. non-Poissonian internet packet traffic [56]. These facts suggest that accelerating structures exhibit a memory of the surface modifications caused by normal RF pulses and breakdowns.

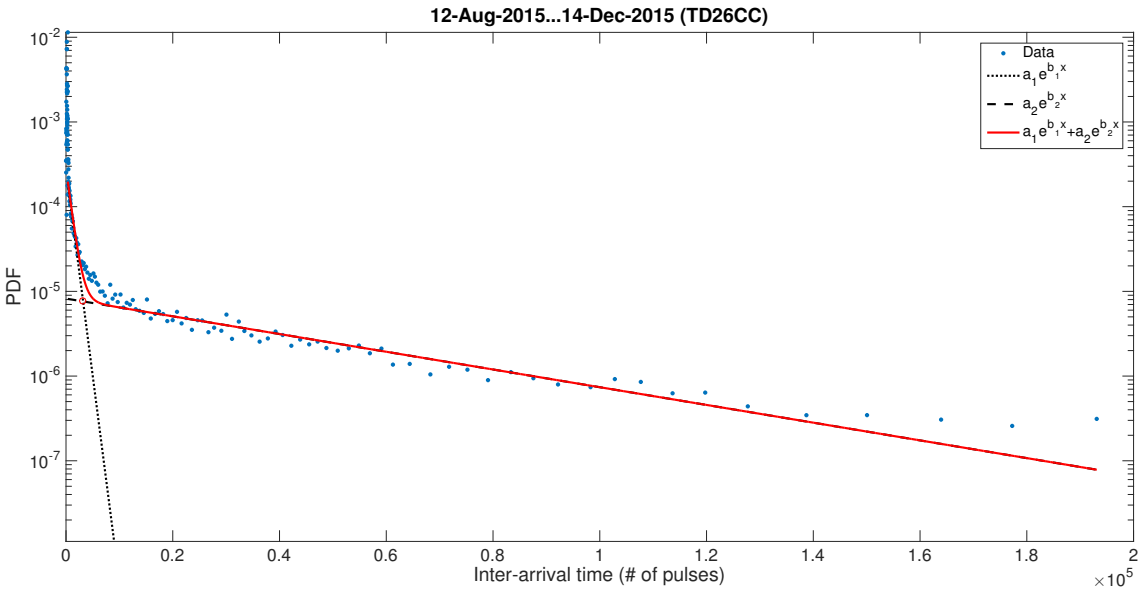

Figure 50: Breakdown inter-arrival time distribution (TD26CC). The PDF can be explained by a mixture of two exponential distributions: one for primary and one for follow-up breakdowns.

If the breakdown process has a memory, it is reasonable to assume that breakdowns clustered in time are also clustered in space. A first indication of this is given by the time delay difference of consecutive breakdowns, which for clarity is referred to as *spatial displacement* from here on (see section 5.4.2). If the time delay of breakdown number i is given by $\tau_d^{(i)}$, then the spatial displacement is

$$\Delta\tau_d^{(i)} = \tau_d^{(i)} - \tau_d^{(i-1)}. \tag{46}$$

Fig. 51 shows the spatial displacement distribution of consecutive breakdowns a) after and b) before randomly permuting their order of occurrence (i.e. shuffling index i before evaluating Eq. 46). The former distribution has a distinctly triangular

shape, which is expected for uncorrelated events (convolution of the approximately uniform PDFs of two independent random variables). The latter, strongly peaked distribution demonstrates that there indeed is a temporal correlation between position estimates. This is further illustrated by Fig. 52 and 53, which show breakdown inter-arrival times plotted against spatial displacement in two different structures (the TD26CC and the T24 before the hot cell). The solid red line shows median and dashed lines indicate percentiles that contain 50% and 90% of the data. It can be seen that the shorter the inter-arrival time between consecutive breakdowns is, the likelier they are to be close to each other in space. As the time between breakdowns increases, the correlation weakens. The discrete vertical lines and spaces at inter-arrival times < 350 pulses in Fig. 52 are artifacts of the conditioning algorithm used to ramp up the RF power after a breakdown.

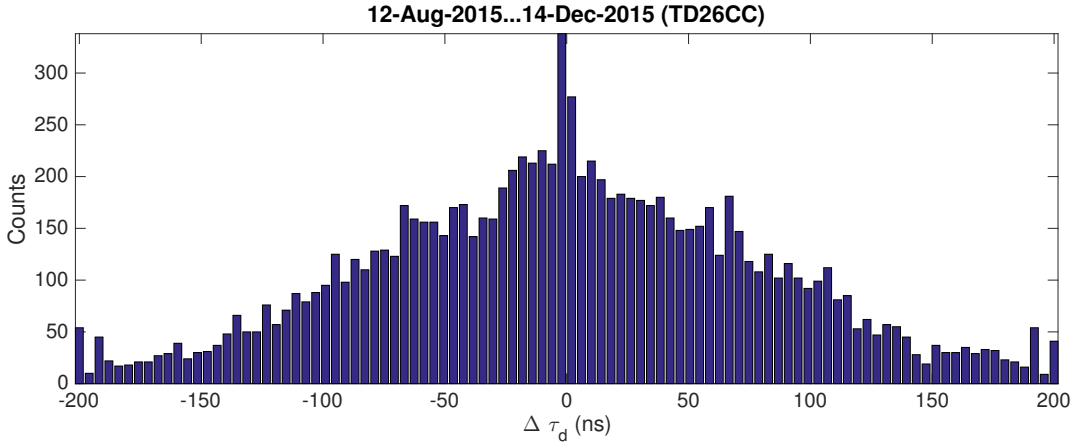

(a) Permuted breakdown order

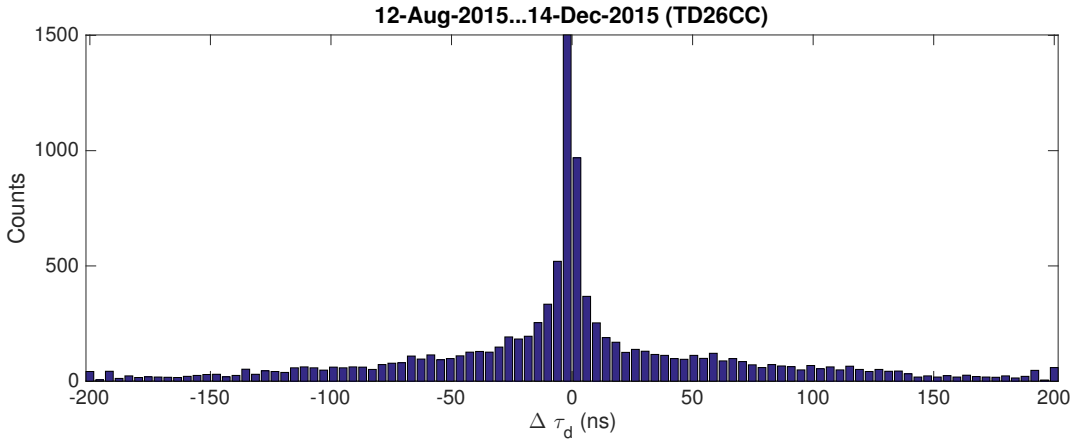

(b) Original breakdown order

Figure 51: Spatial displacement distribution of consecutive breakdowns (TD26CC, correlation method). Distribution (b) is significantly peaked towards zero and sufficiently different from (a), suggesting that consecutive breakdowns consistently occur close-by in space.

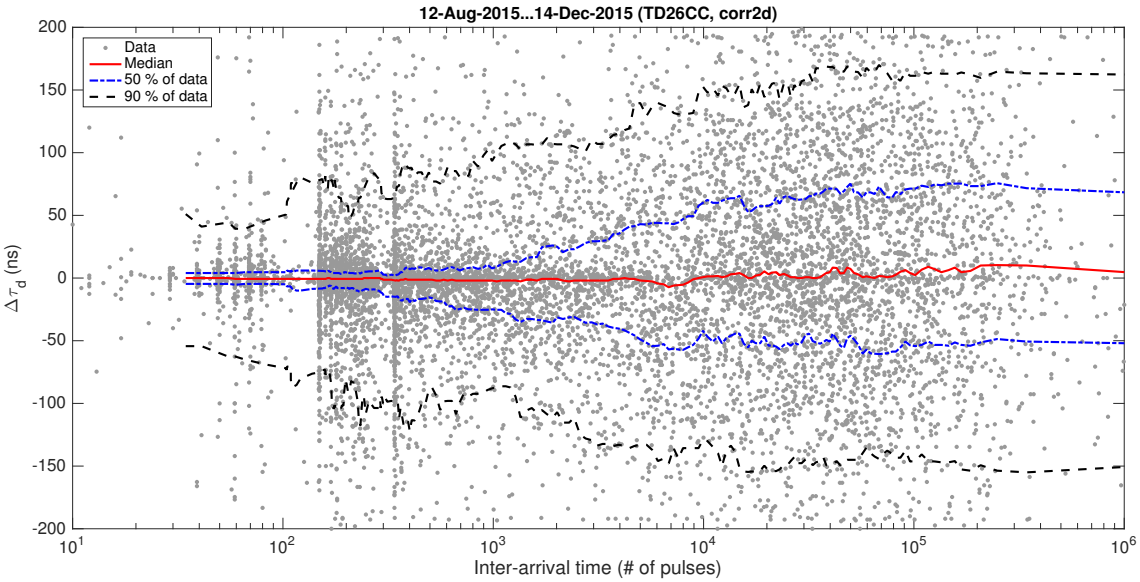

Figure 52: Scatter plot of breakdown inter-arrival time and spatial displacement (TD26CC, correlation method). The increasing spread of the data towards large inter-arrival times demonstrates that breakdowns occurring shortly after each other are more likely to be clustered in space.

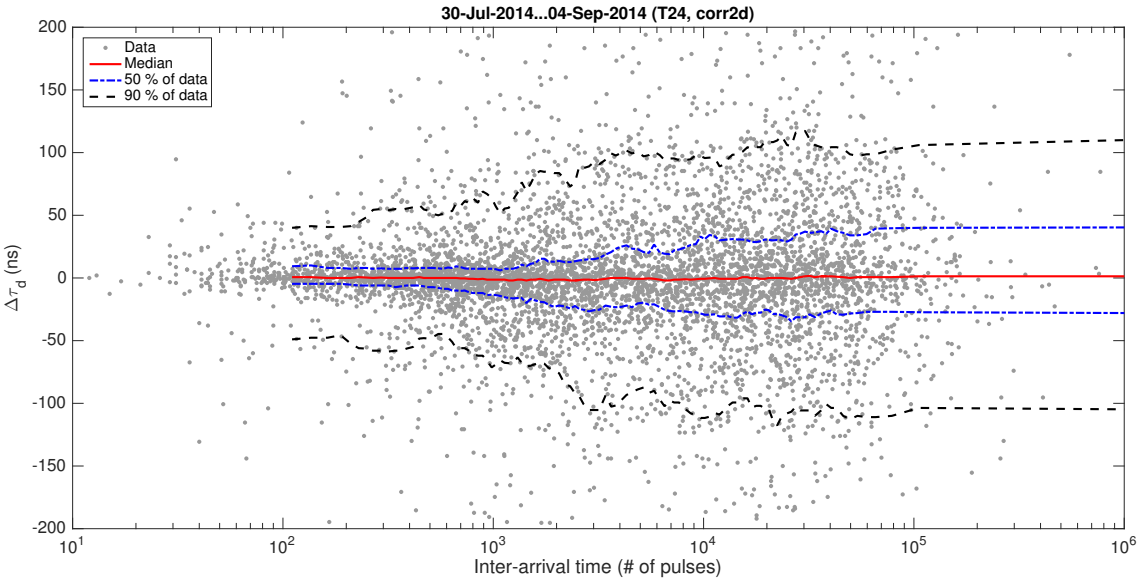

Figure 53: Scatter plot of breakdown inter-arrival time and spatial displacement (T24, correlation method). The spatio-temporal correlation observed in the TD26CC (Fig. 52) is reproduced in the data of the T24 before the hot cell period.

7 Conclusions

In this chapter, the main findings of the work are summarized and future outlooks in breakdown positioning is discussed.

7.1 Summary

In this work, methods used for vacuum arc localization in CLIC prototype RF accelerating structures were presented. In particular, two existing RF power and phase based techniques, the edge and correlation method, were examined in detail and extended. Additionally, a brief overview of other localization methods used in the field was given. As novel contributions, the edge and correlation methods were parametrized and an expression for the bias of the edge method was derived.

The edge and correlation methods were applied to data gathered from two klystron based high-power test stands at CERN: Xbox-1 and 2. Altogether, four different CLIC prototype RF structures were analyzed. Three of these were constant gradient accelerating structures (the T24, T24 open and TD26CC) and one was a constant impedance deflecting structure (the CLIC Crab Cavity). One of the constant gradient structures (the T24 open) was fabricated from two milled copper halves, instead of a bonded stack of copper disks, which is typically the case.

The breakdown position history of all four structures was analyzed. The position distribution of the TD26CC was approximately uniform, as expected of a constant gradient structure. The distribution of the CLIC Crab Cavity was peaked towards the first couple of upstream cells, which is consistent with the expected behavior of a constant impedance structure. The distribution was also in good agreement with a post-mortem analysis, in which breakdown craters were counted. The two remaining constant gradient structures (the T24 and T24 open) displayed expected uniform position distributions during early stages of conditioning, but later both developed hot cells in the front of the structures. Consequently, the high-power test of the T24 was aborted and the structure was replaced. At the time of writing, high-power tests of the TD26CC and the T24 open had not yet finished. The T24 open was still conditioning in spite of the hot cell.

The precision of the correlation and edge methods was estimated during hot cell periods in the T24 and T24 open. The time delay estimates of the correlation method were found to achieve a precision of roughly 3-4 ns. The corresponding precision of the edge method was 10-13 ns. In the case of the correlation method, the estimated precision was consistent with the observed precision of one cell in the upstream cells of the TD26CC.

When comparing the two localization methods, evidence supporting the breakdown migration hypothesis was found. Specifically, it was observed that the correlation method was more likely to yield position estimates closer to the structure input than the edge method. This could be explained by migration, if the onset of the breakdown is assumed to be found by the edge method and the final position by the correlation method. Furthermore, the phase difference between REF and INC was often unstable during the onset of the breakdown, which is suggestive of a moving

arc and therefore consistent with the migration hypothesis.

A correlation analysis of the inter-arrival time and position of consecutive breakdowns was also performed. It was demonstrated for the first time that when the inter-arrival time of consecutive breakdowns is small, the breakdown positions are highly correlated. Conversely, when the inter-arrival time is large, the positions are uncorrelated. This discovery confirms the intuitive idea that breakdowns clustered in time tend to occur in the same region of the accelerating structure.

7.2 Future work

7.2.1 RF power and phase methods

From the results presented in section 6.1.1, one of the central unanswered questions is: what is limiting the localization precision for downstream breakdowns? Dispersion is a likely candidate, but further investigation is required to be sure.

The edge method still has plenty of room for development. The most obvious improvement, which was not explored in this work, but has been used by others [6], is replacing the TRA falling edge by a Faraday cup signal. In the case of relativistic electrons and a structure length around 20 cm, the propagation delay from the vacuum arc to the Faraday cup can be neglected. Therefore, one is left with a transient at the breakdown onset in the RF pulse. This transient is generally faster than the falling edge of TRA and should therefore improve the accuracy of the edge method.

For estimating the edge method bias (Eq. 32) accurately, the falling/rising slope model needs to be refined. As a first step, one could fit a line to the slope using several points, instead of only the two (at p and $1 - p$ of the maximum) currently used. The error of the fit would serve as a filtering criteria for discarding uncertain estimates. As a second step, one might try a non-linear fit. E.g. the error function has been found to fit the data quite well [29, 57].

For a complete characterization of the correlation method, a systematic study of the influence of the up-sampling factor and Δa on the relative error should be performed. Also, the correlation method could be made more robust by applying a deterministic amplitude modulation to an analysis signal propagating in a higher pass band of the structure, as suggested in e.g. [58].

7.2.2 Other localization methods

During the course of this work, accelerometers were partially incorporated into breakdown positioning in the Xbox test stands. Several of the results in [5, 43] were reproduced and acoustic breakdown positioning was found to be consistent with RF power based positioning [58]. In particular, an RSS based acoustic method was in good agreement with the correlation method. Based on this observation, it was postulated that the breakdown generally deposits most of its energy in the final position that the arc has migrated to. When considering that the recorded acoustic signals had a rise time of $\mathcal{O}(1\ \mu\text{s})$, it is clear that only a weighted average of the breakdown position during the RF pulse could be detected.

Accelerometers open up several interesting avenues for future work related to vacuum arc localization. For example, transverse breakdown positioning and modal analysis of breakdown versus pulsed surface heating induced structural vibrations are interesting topics demanding further study. Preliminary attempts of the former were unsuccessful on the CLIC Crab Cavity, since the transverse localization was complicated by awkwardly placed structure cooling blocks. An attempt on the modal analysis was also made, both experimentally and using finite-element based simulations. A clear difference between pulsed surface heating and breakdown induced acoustical signals was observed in both [58]. However, it was concluded that the bandwidth of the accelerometers needs to be increased to $> \mathcal{O}(100$ kHz), since very little mechanical energy is deposited at frequencies below $\mathcal{O}(10$ kHz) during pulsed surface heating or breakdown. Laser interferometry could be used to characterize the frequency response of the accelerometers or alternatively, to replace them altogether.

7.2.3 Vacuum arc studies

The timing of the breakdown within the RF pulse is an interesting topic closely related to breakdown localization. It has long been known that breakdowns usually occur rather uniformly within the flat-top part of the RF pulse, although breakdowns after the main pulse are also regularly observed (see e.g. [59]). These events are curious, since one would no longer expect vacuum arcs to develop after the fields have decayed to a fraction of their maximum value. From the multitude of possible correlation analyses between breakdown position in space and timing in pulse, one proposed by F. Tecker (private communications, 2015) is especially intriguing: Comparing the timing of the breakdown with migration distance. This could offer evidence in support of or against the migration hypothesis. If the hypothesis is true, one would in general expect late breakdowns to migrate shorter distances than early breakdowns.

Regarding breakdown migration, there also exists a complementary explanation to the evidence presented in section 6.3.1. The migration hypothesis hinges on the assumption that the breakdown onset is instantaneous, i.e. the rising edge of REF is synchronized with the falling edge of TRA. However, Fig. 54 suggest that this assumption might not be entirely accurate. In the right plot, when REF is aligned with INC using the correlation method, the falling edge of the first peak coincides with the falling edge of INC and a sizable gap is left between TRA and REF. This prompts the question: what if there is a period during the onset of a breakdown, when the arc only absorbs power (similarly to what was suggested in Fig. 49)? In other words, a time dependent modulation of the breakdown reflection coefficient could explain many of the phenomena observed in section 6.3.1. Using this point of view, Fig. 45 may be interpreted as the distribution of the time it takes for an arc build up from ignition to full reflection. As a side note, Fig. 54 also revives interest in the question of *missing energy*, which here refers to the energy difference between INC and REF+TRA not accounted for by resistive losses in the structure. In particular, a modulating or amplitude dependent reflection coefficient

could explain part of the missing energy seen in Fig. 54.

The formation of a hot cell in two of the three tested constant gradient structure grabs one's attention. Especially the fact that the hot cells appear in the beginning of the structures is curious. Although purely design and manufacturing related causes cannot be excluded, an alternative explanation is presented next. Based on results from DC breakdown experiments, it was recently suggested by A. Korsbäck (private communications, 2016) that RF structures might condition non-uniformly. This would manifest itself as a position dependent BDR (conditioning state), or more importantly, a position depended first time derivative of the BDR (conditioning rate). If the conditioning rate varies along the structure (e.g. from cell to cell), one would expect the segment with the worst conditioning state to eventually start dominating the overall structure BDR. However, the central realization is that if and when conditioning saturates, the differing conditioning states might once again converge and the breakdown position distribution could regain its original shape. This would be an example of a *benign hot cell*. On the other hand, a *malignant hot cell* ceases to condition, or rather, starts deconditioning. These two scenarios are illustrated in Fig. 55 for the structure arbitrarily divided down the middle into an upstream and a downstream part. Based on Fig. 36 and 40, the hot cell in the T24 appears malignant, whereas the one in the T24 open seems benign. If the hot cell in the T24 open were to disappear after further conditioning, it would provide convincing evidence in support of the non-uniform conditioning hypothesis.

Ultimately, it is the author's opinion that alternative breakdown localization methods need to be implemented in order to fully address many of the questions posed in this chapter.

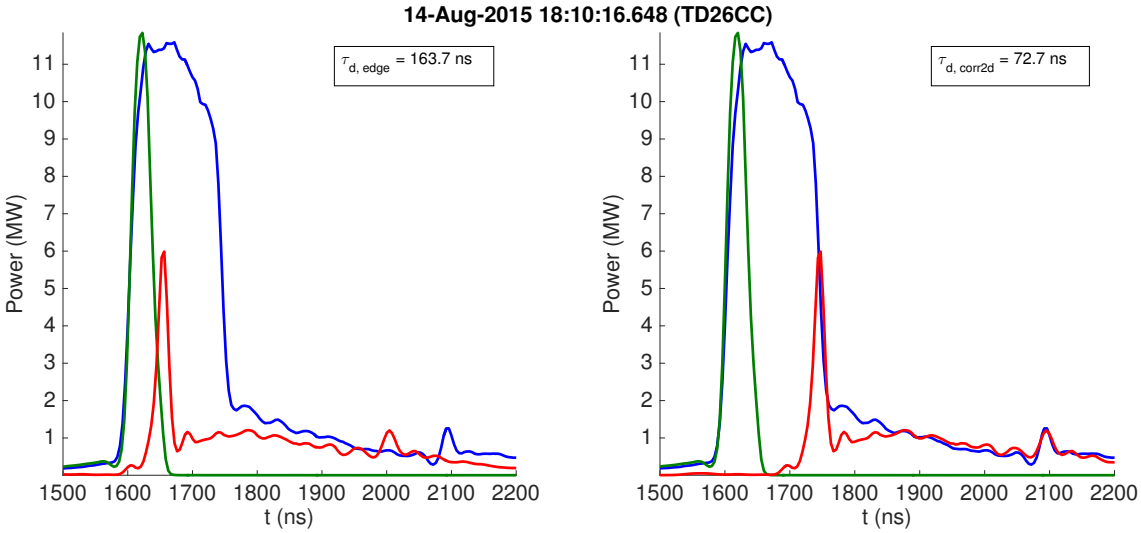

Figure 54: Breakdown migration or missing energy due to a time-varying reflection coefficient?

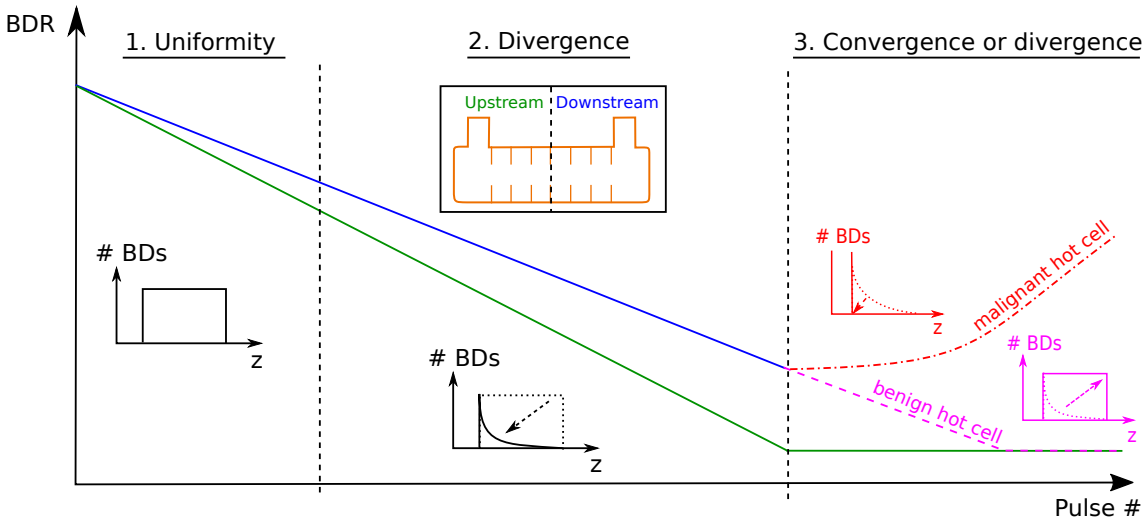

Figure 55: Different stages of non-uniform conditioning. The mechanism predicts that hot cells could sometimes disappear through conditioning.

References

[1] M. Aicheler, P. Burrows, M. Draper, T. Garvey, P. Lebrun, K. Peach, N. Phinney, H. Schmickler, D. Schulte, N. Toge, et al. A multi-tev linear collider based on clic technology: Clic conceptual design report. Technical Report CERN-2012-007, CERN, 2012.

[2] W. Wuensch. Advances in the understanding of the physical processes of vacuum breakdown. CERN-OPEN-2014-028; CLIC-Note-1025, 2013. URL https://cds.cern.ch/record/1694664. Accessed: 2016-03-07.

[3] A. Degiovanni, W. Wuensch, and J. Giner Navarro. Comparison of the conditioning of high gradient accelerating structures. CERN-ACC-2015-0139 ; CLIC-Note-1056, 2015. URL https://cds.cern.ch/record/2065711?ln=en. Accessed: 2016-03-07.

[4] F. Wang. Breakdown characteristics study on an 18 cell x-band structure. In *American Institute of Physics (AIP) Conference Proceedings, Santa Cruz, California, USA*, number 1086, 1, pages 373–379, 2008.

[5] J. Nelson, M. Ross, J. Frisch, E. Le Pimpec, K. Jobe, D. McCormick, and T. Smith. Use of acoustic emission to diagnose breakdown in accelerator rf structures. In *Proceedings of the Particle Accelerator Conference 2003 (PAC2003), Portland, Oregon, USA*, volume 2, pages 1279–1281. IEEE, 2003.

[6] A. Degiovanni, S. Dobert, W. Farabolini, I. Syratchev, W. Wuensch, J. Giner Navarro, J. Tagg, and B. Woolley. Diagnostics and analysis techniques for high power x-band accelerating structures. In *Proceedings of the Linear Accelerator Conference 2014 (LINAC14), Geneva, Switzerland*, pages 490–492, 2014. ISBN 978-3-95450-142-7.

[7] T. Higo, M. Akemoto, A. Enomoto, S. Fukuda, H. Hayano, N. Kudo, S. Matsumoto, T. Saeki, N. Terunuma, N. Toge, K. Watanabe, and T. Suehara. High gradient study at kek on x-band accelerator structure for linear collider. In *Proceedings of the Particle Accelerator Conference 2005 (PAC2005)*, pages 1162–1164, May 2005. doi: 10.1109/PAC.2005.1590694.

[8] S. M. Kay. *Fundamentals of Statistical Signal Processing: Estimation theory*, pages 1–2, 15, 34. Prentice-Hall PTR, 1st edition, 1993. ISBN 9780133457117.

[9] S. Gezici, Zhi Tian, G. B. Giannakis, H. Kobayashi, A. F. Molisch, H. V. Poor, and Z. Sahinoglu. Localization via ultra-wideband radios: a look at positioning aspects for future sensor networks. *IEEE Signal Processing Magazine*, 22(4): 70–84, July 2005. ISSN 1053-5888. doi: 10.1109/MSP.2005.1458289.

[10] C. H. Knapp and G. C. Carter. The generalized correlation method for estimation of time delay. *IEEE Transactions on Acoustics, Speech and Signal Processing*, 24(4):320–327, 1976.

[11] Circuit Cellar staff. Triangulation, trilateration, or multilateration? (ee tip #125). Online article, 2014. URL http://circuitcellar.com/ee-tips/triangulation-trilateration-or-multilateration-ee-tip-125/. Accessed: 2016-03-06.

[12] D. M. Pozar. *Microwave engineering*, page 1. John Wiley & Sons, 4th edition, 2012. ISBN 978-0-470-63155-3.

[13] Rolf Wideröe. Über ein neues prinzip zur herstellung hoher spannungen. *Archiv für Elektrotechnik*, 21(4):387–406, 1928.

[14] T. P. Wangler. *RF Linear accelerators*, pages 3, 20–21,55, 58, 72–76. John Wiley & Sons, 2nd edition, 2008. ISBN 978-3-527-40680-7.

[15] CERN Bulletin. The invention that is shaping linac4. Online article, 2010. URL https://cds.cern.ch/journal/CERNBulletin/2010/31/News%20Articles/1281668?ln=en. Accessed: 2016-01-22.

[16] J. C. Maxwell. A dynamical theory of the electromagnetic field. *Philosophical Transactions of the Royal Society of London*, pages 459–512, 1865.

[17] D. J. Griffiths. *Introduction to electrodynamics*, pages 321, 409. Prentice Hall Upper Saddle River, NJ, 3rd edition, 1999. ISBN 0-13-805326-X.

[18] M. Weiss. Introduction to rf linear accelerators. CERN Accelerator School 1992 (CAS92), 5th General Accelerator Physics Course, Jyväskylä, Finland, 1994. URL https://cds.cern.ch/record/261732?ln=en. Accessed: 2016-03-07.

[19] HFSS. *version 15.0.3*. ANSYS Inc., Cecil Township, Pennsylvania, 2013.

[20] A. Streun. Experimental methods of particle physics - particle accelerators. Lecture slides, October 2014. URL https://ados.web.psi.ch/empp-streun/empp.pdf. Accessed: 2015-27-09.

[21] A. Palaia, M. Jacewicz, R. Ruber, V. Ziemann, and W. Farabolini. Effects of rf breakdown on the beam in the compact linear collider prototype accelerator structure. *Physical Review Special Topics-Accelerators and Beams*, 16(8): 081004, 2013.

[22] S. Döbert, C. Adolphsen, G. Bowden, D. Burke, J. Chan, V. Dolgashev, J. Frisch, K. Jobe, R. Jones, J. Lewandowski, et al. High gradient performance of nlc/glc x-band accelerating structures. In *Proceedings of the Particle Accelerator Conference 2005 (PAC2015)*, pages 372–374. IEEE, 2005.

[23] H. Timko. *Modelling vacuum arcs: from plasma initiation to surface interactions*. PhD thesis, University of Helsinki, 2011.

[24] A. Palaia. *Beam Momentum Changes due to Discharges in High-gradient Accelerator Structures*. PhD thesis, Uppsala Universitet, 2013.

[25] R. H. Fowler and L. Nordheim. Electron emission in intense electric fields. In *Proceedings of the Royal Society of London A: Mathematical, Physical and Engineering Sciences*, volume 119, 781, pages 173–181. The Royal Society, 1928.

[26] A. Grudiev, S. Calatroni, and W. Wuensch. New local field quantity describing the high gradient limit of accelerating structures. *Physical Review Special Topics-Accelerators and Beams*, 12(10):102001, 2009.

[27] S. Döbert. Gradient limitations for high-frequency accelerators. In *Proceedings of the International Linear Accelerator Conference 2003 (LINAC03), Lübeck, Germany*, number WE101; SLAC-PUB-10690, pages 513–517, August 2004.

[28] A. Degiovanni, S. Dobert, W. Farabolini, A. Grudiev, J. Kovermann, E. Montesinos, G. Riddone, I. Syratchev, R. Wegner, W. Wuensch, et al. High-gradient test results from a clic prototype accelerating structure: Td26cc. In *Proceedings of the International Particle Accelerator Conference 2014 (IPAC2014), Dresden, Germany*, pages 2285–2287, 2014. ISBN 978-3-95450-132-8.

[29] N. C. Shipman. *Experimental study of DC vacuum breakdown and application to high-gradient accelerating structures for CLIC*. PhD thesis, The University of Manchester, 2014.

[30] A. Descoeudres, Y. Levinsen, S. Calatroni, M. Taborelli, and W. Wuensch. Investigation of the dc vacuum breakdown mechanism. *Physical Review Special Topics-Accelerators and Beams*, 12(9):092001, 2009.

[31] A. Korsbäck, W. Wuensch, J. Giner Navarro, and R. Rajamäki. Statistics of vacuum electrical breakdown occurrence. *Manuscript in preparation for Physical Review Special Topics - Accelerators and Beams*, 2016.

[32] B. Woolley. *High Power X-band RF Test Stand Development and High Power Testing of the CLIC Crab Cavity*. PhD thesis, Lancaster university, 2015.

[33] J. Giner Navarro. High-gradient structure performances: Ongoing tests and summary. Presentation, CLIC workshop 2016 (CLWS2016), Geneva, Switzerland, January 2016. URL https://indico.cern.ch/event/449801/session/0/contribution/14. Accessed: 2016-02-16.

[34] Scandinova. K2-3 solid state modulator datasheet, 2015. URL http://www.scandinovasystems.com/assets/upload/files/K2-3-web.pdf. Accessed: 2015-12-05.

[35] CPI Communication & Power Industries. Vkx-8311a pulsed klystron datasheet, 2015. URL http://www.cpii.com/docs/datasheets/154/VKX-8311A%20Datasheet.pdf. Accessed: 2015-12-05.

[36] J. Kovermann, K. Schirm, N. Catalan-Lasheras, E. Paju, G. McMonagle, D. Sprehn, M. Naon, F. F. Peauger, J. Eichner, S. Doebert, et al. Commissioning of the first klystron-based x-band power source at cern. In *Proceedings of the*

International Particle Accelerator Conference 2012 (IPAC2012), New Orleans, Louisiana, USA, number 1205201, IPAC-2012-THPPC060; SLAC-PUB-15805, pages 3428–3430, 2012.

[37] N. Catalan-Lasheras, A. Degiovanni, S. Dobert, W. Farabolini, J. Kovermann, G. McMonagle, S. Rey, I. Syratchev, L. Timeo, W. Wuensch, et al. Experience operating an x-band high-power test stand at cern. In *Proceedings of the International Particle Accelerator Conference 2014 (IPAC2014), Dresden, Germany*, pages 2288–2290, 2014. ISBN 978-3-95450-132-8.

[38] F. Tecker, J. Navarro Quirante, R. Corsini, M. Kelisani, S. Doebert, I. Syratchev, S. Lebet, W. Wuensch, O. Kononenko, A. Solodko, et al. Experimental study of the effect of beam loading on rf breakdown rate in clic high-gradient accelerating structures. In *Proceedings of the International Particle Accelerator Conference 2013 (IPAC2013), Shanghai, China*, pages 1691–1693, 2013. ISBN 978-3-95450-122-9.

[39] R. Zennaro, A. Grudiev, G. Riddone, A. Samoshkin, W. Wuensch, and S. Tantawi. Design and fabrication of clic test structures. In *Proceedings of the Linear Accelerator Conference 2008 (LINAC08), Victoria, BC, Canada*, pages 533–535, 2008.

[40] V. Dolgashev, J. Haase, A. Lewandowski, G. Bowden, Z. Hao, and A. Grudiev. Building open traveling wave accelerating structure. Presentation slides, International Workshop on Breakdown Science and High Gradient Technology (HG2015), Tsinghua University, Beijing, China, 2015. URL https://indico.cern.ch/event/358352/session/4/contribution/24/attachments/1142231/1636482/CLIC-G-OPEN_HG2015_V1947_11Jun2015.pdf. Accessed: 2015-12-05.

[41] A. Grudiev and W. Wuensch. Design of the clic main linac accelerating structure for clic conceptual design report. In *Proceedings of the Linear Accelerator Conference 2010 (LINAC10), Tsukuba, Japan*, pages 211–213, 2010.

[42] B. Woolley, P. Ambattu, R. Apsimon, G. Burt, A. Dexter, A. Grudiev, I. Syratchev, R. Wegner, and W. Wuensch. High gradient testing of an x-band crab cavity at xbox2. In *Proceedings of the International Particle Accelerator Conference 2015 (IPAC2015), Richmond, Virginia, USA*, pages 3242–3245, 2015. ISBN 978-3-95450-168-7.

[43] F. Le Pimpec, J. Frisch, K. Jobe, D. McCormick, J. Nelson, M. Ross, and T. Smith. An acoustic sensor system for localizing rf breakdown in warm copper accelerating structures. *Nuclear Instruments and Methods in Physics Research Section A: Accelerators, Spectrometers, Detectors and Associated Equipment*, 582(2):345–355, 2007.

[44] N. Shipman, S. Calatroni, R. M. Jones, and W. Wuensch. Measurement of the dynamic response of the cern dc spark system and preliminary estimates

of the breakdown turn-on time. In *Proceedings of the International Particle Accelerator Conference 2012 (IPAC2012), New Orleans, Lousiana, USA*, pages 3338–3340, 2012.

[45] N. Vogel. X-ray radiation from cathode spot fragments in low voltage vacuum arcs. In *Proceedings of the XVIIIth International Symposium on Discharges and Electrical Insulation in Vacuum 1998 (ISDEIV98)*, volume 1, pages 202–206. IEEE, 1998.

[46] T. Abe, T. Kageyama, H. Sakai, Y. Takeuchi, and K. Yoshino. Breakdown study based on the direct in-situ observation of inner surfaces of an rf accelerating cavity during a high-gradient test. KEK Preprint 2015-25, August 2015. URL http://ccdb5fs.kek.jp/tiff/2015/1527/1527025.pdf. Accessed: 2016-03-07.

[47] W. Farabolini. Comparison of breakdown behavior between klystron and beam driven structures. Presentation slides, International Workshop on Breakdown Science and High Gradient Technology (HG2013), ICTP, Trieste, Italy, June 2013. URL https://indico.cern.ch/event/231116/contribution/35. Accessed: 2016-02-24.

[48] M. Jacewicz. Breakdown tomography with emitted electrons. Presentation, CLIC Workshop 2016 (CLWS2016), Geneva, Switzerland, January 2016. URL https://indico.cern.ch/event/449801/session/0/contribution/28. Accessed: 2016-01-25.

[49] M. Jacewicz, Ch. Borgmann, J. Ögren, R. Ruber, and V. Ziemann. General-purpose spectrometer for vacuum breakdown diagnostics for the 12 ghz test stand at cern. In *Proceedings of the International Particle Accelerator Conference 2014 (IPAC2014), Dresden, Germany*, pages 3668–3670, 2014.

[50] A. P. Fontenla. Post-mortem analysis: Sem imaging review. Presentation, MeVArc - 5th international workshop on mechanisms of vacuum arcs, Saariselkä, Finland, September 2015. URL https://indico.cern.ch/event/354854/session/9/contribution/24/attachments/1148696/1647914/Post_mortem_SEM_images_review_MeVarc15_Anite_Perez_Fontenla.pdf. Accessed: 2015-10-10.

[51] E. Rodriguez Castro. Clic crab cavity post-mortem analysis. Presentation, CLIC Workshop 2016 (CLWS2016), Geneva, Switzerland, January 2016. URL https://indico.cern.ch/event/449801/session/0/contribution/29. Accessed: 2016-01-25.

[52] F. Wang. Processing and breakdown localization results for an l-band standing-wave cavity. In *Proceedings of the Particle Accelerator Conference 2009 (PAC2009), Vancouver, British Columbia, Canada*, number WE5PFP017, SLAC-PUB-13739, pages 2024–2026, 2009.

[53] R. H. Goulding, T. S. Bigelow, and D. W. Swain. Investigation of high voltage breakdown and arc localization in rf structures. In *AIP Conference Proceedings*, pages 425–428. IOP INSTITUTE OF PHYSICS PUBLISHING LTD, 1999.

[54] E. Alpaydin. *Introduction to Machine Learning*, pages 135–139. MIT press, 1st edition, 2004. ISBN 0-262-01211-1.

[55] A. Degiovanni, W. Farabolini, et al. Breakdown position analysis. Presentation slides, International Workshop on Breakdown Science and High Gradient Technology (HG2015), Tsinghua University, Beijing, China, 2015. URL https://indico.cern.ch/event/358352/session/0/contribution/10. Accessed: 2016-03-07.

[56] W. E. Leland, M. S. Taqqu, W. Willinger, and D. V. Wilson. On the self-similar nature of ethernet traffic. In *ACM SIGCOMM Computer Communication Review*, volume 23, 4, pages 183–193. ACM, 1993.

[57] A. Dubrovskiy. Breakdown turn-on time from tbts and kek data. Presentation slides, RF development meeting, Geneva, Switzerland, May 2012. URL http://indico.cern.ch/event/178005/. Accessed: 2016-02-24.

[58] W. Farabolini et al. Rf and acoustical methods for breakdown localization in high gradient accelerating structures. Poster, MeVArc - 5th international workshop on mechanisms of vacuum arcs, Saariselkä, Finland, 2015. URL https://indico.cern.ch/event/354854/page/5205-poster-presentations. Accessed: 2016-02-24.

[59] C. Adolphsen, W. Baumgartner, K. Jobe, F. Le Pimpec, R. Loewen, D. McCormick, M. Ross, T. Smith, J. W. Wang, and T. Higo. Processing studies of x-band accelerator structures at the nlcta. In *Proceedings of the Particle Accelerator Conference 2001 (PAC2001)*, volume 1, pages 478–480. IEEE, 2001.

Appendix A Edge method parameter

Due to the trade-off between bias and susceptibility to noise, the largest possible value that results in an acceptable error rate should be selected for the edge method parameter p. A heuristic value of $p = 0.8$ was settled upon and consequently used throughout this work.

Fig. 56 demonstrates that the choice of p does not significantly change the breakdown position distribution - at least qualitatively speaking. Curiously, the upstream part of the distribution is affected by p the most. Compensating for the bias using Eq. 32 did not mitigate the influence of p on the distribution remarkably. The most likely reason for this is inaccurately estimated fall and rise times, $\hat{T}_\mathrm{F}$ and $\hat{T}_\mathrm{R}$. If the uncertaintly related to the estimates of the two random variables is large, it is be better not to compensate for the bias in Eq. 30 at all. This was the approach ultimately adopted in this work.

The distribution of $\hat{T}_\mathrm{F}$ and $\hat{T}_\mathrm{R}$ for varying p and two different structures is shown in Fig. 57. One feature seen across all tested structures is that the fall time of TRA is systematically longer than the rise time of REF. Naively, one would expect the two to be equal, if the ignition of the breakdown is assumed to be instantaneous. Actually, if the rise/fall times are limited by the bandwidth of the structure and breakdowns are distributed uniformly in space, one would expect the quite the opposite result (i.e. $T_\mathrm{R} > T_\mathrm{F}$, since REF has to make a round-trip in the structure). Another observation is that the shapes of the distributions differ significantly between the structures installed in Xbox-1 and Xbox-2. It yet remains to be excluded that the observation is not an artefact of the differences between the two acquisition systems.

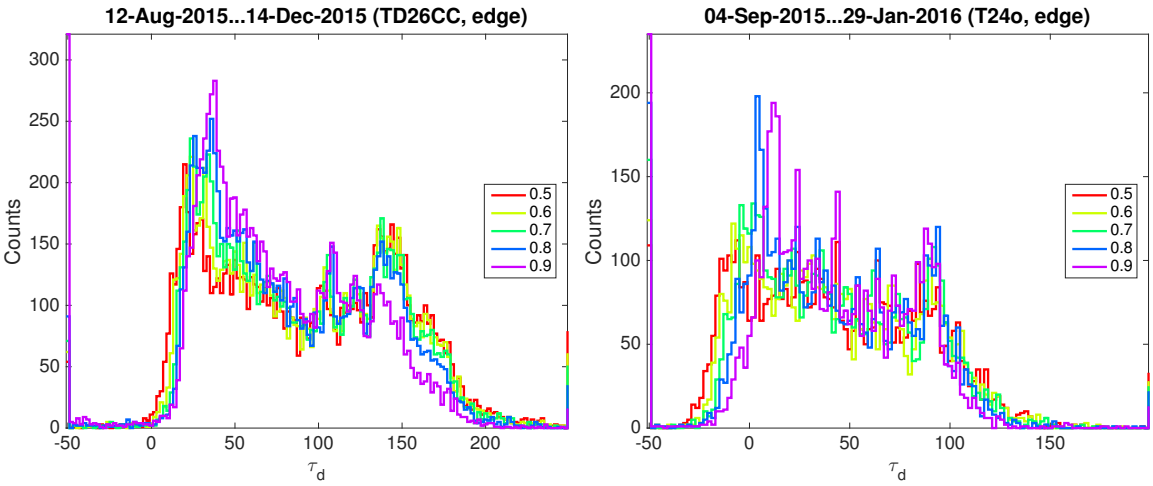

Figure 56: Breakdown time delay distribution for different p. The bulk of the distribution is relatively insensitive to the value of p in the plotted range.

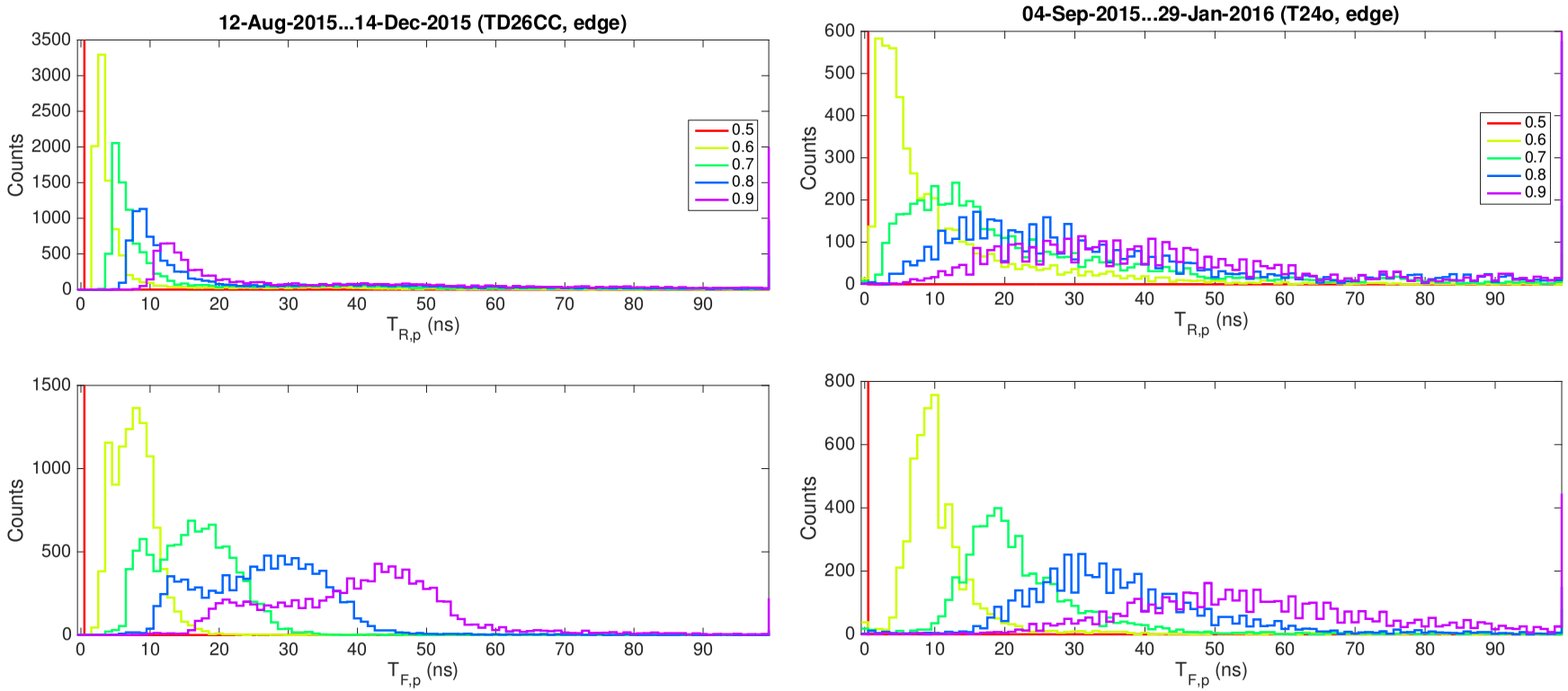

Figure 57: REF rise time ($T_{\mathrm{R},p}$) and TRA fall time ($T_{\mathrm{F},p}$) for different p and two different structures. In general, $T_{\mathrm{R},p} < T_{\mathrm{F},p}$.

Appendix B Correlation method parameters

Because REF is not a delayed copy of INC over its entire length, the signals have to be windowed before correlation. The window positions and sizes must be carefully chosen. Also, as discussed in section 2.3, it is reasonable to choose different sized windows for INC and REF. In principal, the choice of REF or INC as x or s in Eq. 12 is arbitrary. For practical reasons however, it makes sense to use a larger window for REF and a smaller one within this for INC. This way, the part of INC just after the main pulse with strong features and high SNR may be used in the correlation. The procedure for selecting the windows is illustrated in Fig. 58 and outlined next.

From the point of view of making the method robust against noise, the REF window size should be maximized. In practice, an upper bound is set by the length T of the recorded signal and by the measurement noise level. Also, including very late parts of the signal into the correlation window is a waste of computational resources, as any useful reflections have already disappeared beneath the noise floor. The beginning of the window $t_{0,b}$ should be chosen at the very end of the main pulse t_{ep}, as in most cases every feature INC beyond this point is included in REF. This is because breakdowns are most likely to occur during the main pulse, when the fields in the structure reach their peak. If a breakdown happens after the beginning of the INC window, the complete windowed INC is no longer included in the windowed REF. Because the assumptions of the signal model (Eq. 8) no longer hold, the correlation method becomes more prone to error.

The INC window is determined by the allowed minimum and maximum delay τ_d. From a physical point of view, the minimum delay should be zero (corresponding to a breakdown in the very beginning of the structure), whereas the maximum delay should be at least twice the filling time of the structure (corresponding to breakdowns in the last cell). In practice, it is useful to use a slightly higher maximum delay (e.g. $20 - 30\%$ over the nominal double filling time) and to also allow for negative (nonphysical) delays. This way one makes sure that estimates towards the beginning of the structure are not biased by the chosen minimum delay. An additional benefit is that the correlation method becomes more comparable to the edge method, whose estimates can in principle assume any value $\in [-T \dots T]$.

As discussed above, the delay τ_d must be found within the large window. This leads to the condition

$$(t_{0,b} - t_{1,b}) \leq \tau_d \leq (t_{0,e} - t_{1,e}). \tag{47}$$

Physically, the delay should lie somewhere between zero and twice the filling time of the structure, i.e.

$$\begin{cases} t_{0,b} - t_{1,b} &= 0 \\ t_{0,e} - t_{1,e} &= 2\tau_{\text{fill}}. \end{cases} \tag{48}$$

The optimal window parameters (see Fig. 58) can therefore be summarized as

$$\begin{cases} t_{0,b} &= t_{ep} \\ t_{1,b} &= t_{0,b} \\ t_{0,e} &= T \\ t_{1,e} &= t_{0,e} - 2\tau_{\text{fill}} \end{cases} \tag{49}$$

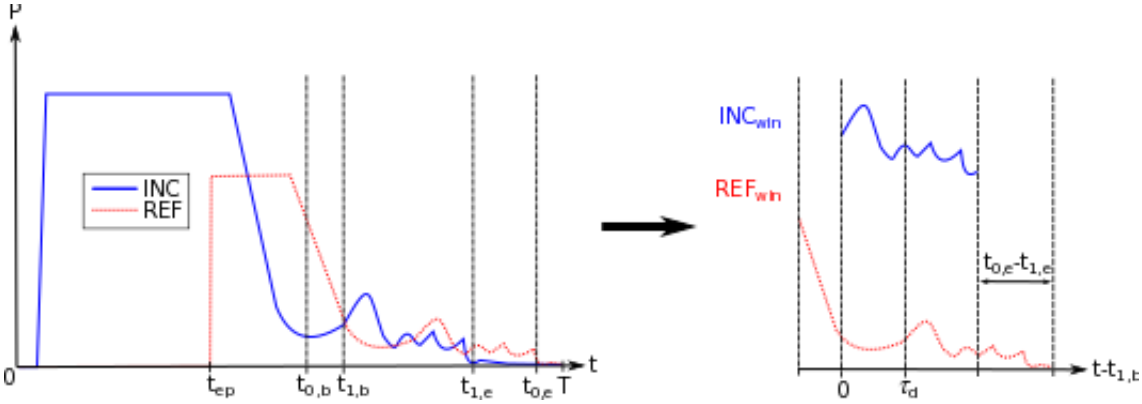

Figure 58: Selection of correlation windows. Left: acquired signals and window edges. Right: windowed signals used by the correlation method.

Physically feasible limits for scale factor a in Eq. 33, such that $a_{\min} \leq a \leq a_{\max}$, can also be determined. The lower limit is $a_{\min} = 1$, which corresponds to a breakdown in the very beginning of the structure. The upper limit is not as straightforward to fix, because it depends on the attenuation in the structure and on the amount of RF power absorbed by the breakdown, which varies between breakdowns. Therefore, the following dynamical energy ratio limit was implemented:

$$a_{max} = \frac{\int_0^{T_{\text{INC}_{\text{win}}}} \text{INC}_{\text{win}}(t)\,\mathrm{d}t}{\min \int_{t_0}^{t_0+T_{\text{INC}_{\text{win}}}} \text{REF}_{\text{win}}(t)\,\mathrm{d}t}, \; 0 \leq t_0 \leq T_{\text{REF}_{\text{win}}} - T_{\text{INC}_{\text{win}}} \tag{50}$$

where REF_{win} and INC_{win} are the reflected and incident signals windowed using the limits in Eq. 49. $T_{\text{INC}_{\text{win}}}$ and $T_{\text{REF}_{\text{win}}}$ are the respective lengths of the windowed signals. By replacing the minimum operator of the denominator in Eq. 49 with the maximum, the dynamical threshold can be extended to $a_{\min}$ as well. This reduces the search range further and relaxes the requirement for accurately calibrated signals. In order to increase robustness against noise, the limits $a_{\min}$ and $a_{\max}$ can again be extended by a few ten percent.

Unfortunately, there is no simple physical constraint for the grid density of the scale factor Δa. Therefore, an ad-hoc approach is adopted instead. First, the scale increment is set to a small reference value ($\mathcal{O}(10^{-3})$), after which it is gradually increased. The RMSE of the time delay estimates with respect to the estimates at the reference level is calculated at each step. A step size which yields a tolerable relative error is chosen. A scale factor step size of roughly $\Delta a = 0.1 - 0.5$ typically yielded around 1 ns relative RMSE across the different structures.

Appendix C Time delay distribution of a constant gradient structure

The expected time delay distribution of a constant-gradient structure is derived next. Firstly, since the group velocity of a constant-gradient structure decays linearly along its length

$$\begin{cases} v_g(z) = a + bz \\ v_g(0) = a \\ v_g(L) = a + bL. \end{cases} \tag{51}$$

Solving Eq. 43, given Eq. 51, yields

$$\tau_{\mathrm{RT}} = \frac{2L}{v_g(L) - v_g(0)} \ln(1 + \frac{v_g(L) - v_g(0)}{v_g(0)} \frac{z_{\mathrm{BD}}}{L}). \tag{52}$$

Rearranging Eq. 52 for the breakdown position z_{BD} results in

$$z_{\mathrm{BD}} = L \frac{v_g(0)}{v_g(L) - v_g(0)} (e^{\tau_{\mathrm{RT}} \frac{v_g(L) - v_g(0)}{2L}} - 1). \tag{53}$$

The expected breakdown distribution of a constant-gradient structure is uniform, i.e.

$$z_{\mathrm{BD}} \sim \mathrm{Uni}(0, L). \tag{54}$$

Therefore, the CDF of z_{BD} is

$$F(z_{\mathrm{BD}}) = \begin{cases} z_{\mathrm{BD}}/L, & 0 \leq z_{\mathrm{BD}} \leq L \\ 0, & \text{otherwise.} \end{cases} \tag{55}$$

Since the PDF is the derivative of the CDF,

$$f(x) = \frac{\mathrm{d}F(x)}{\mathrm{d}x}, \tag{56}$$

the PDF of the time delay is found by inserting Eq. 53 into Eq. 55 and taking the derivative with respect to τ_{RT}. This yields the final result

$$f(\tau_{\mathrm{RT}}) = \begin{cases} \frac{v_g(0)}{2L} e^{\tau_{\mathrm{RT}} \frac{v_g(L) - v_g(0)}{2L}}, & 0 \leq z_{\mathrm{BD}} \leq 2\tau_{\mathrm{fill}} \\ 0, & \text{otherwise.} \end{cases} \tag{57}$$

Fig. 59 shows Eq. 57 evaluated for the three tested constant gradient structures using the parameters from Tab. 1. One can see that approximately double the number of events are expected around $\tau_{\mathrm{RT}} \approx 0$ compared to $\tau_{\mathrm{RT}} \approx 2\tau_{\mathrm{fill}}$.

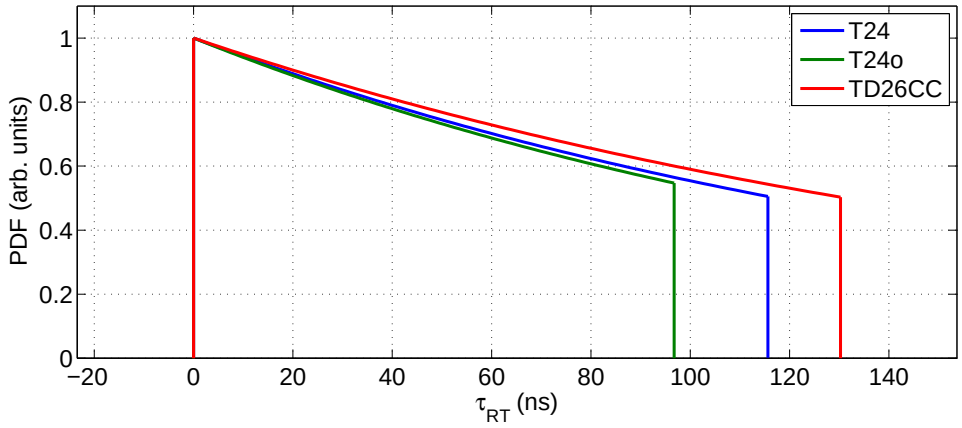

Figure 59: Expected time delay distributions of the tested constant gradient accelerating structures.

Appendix D Group velocity profiles

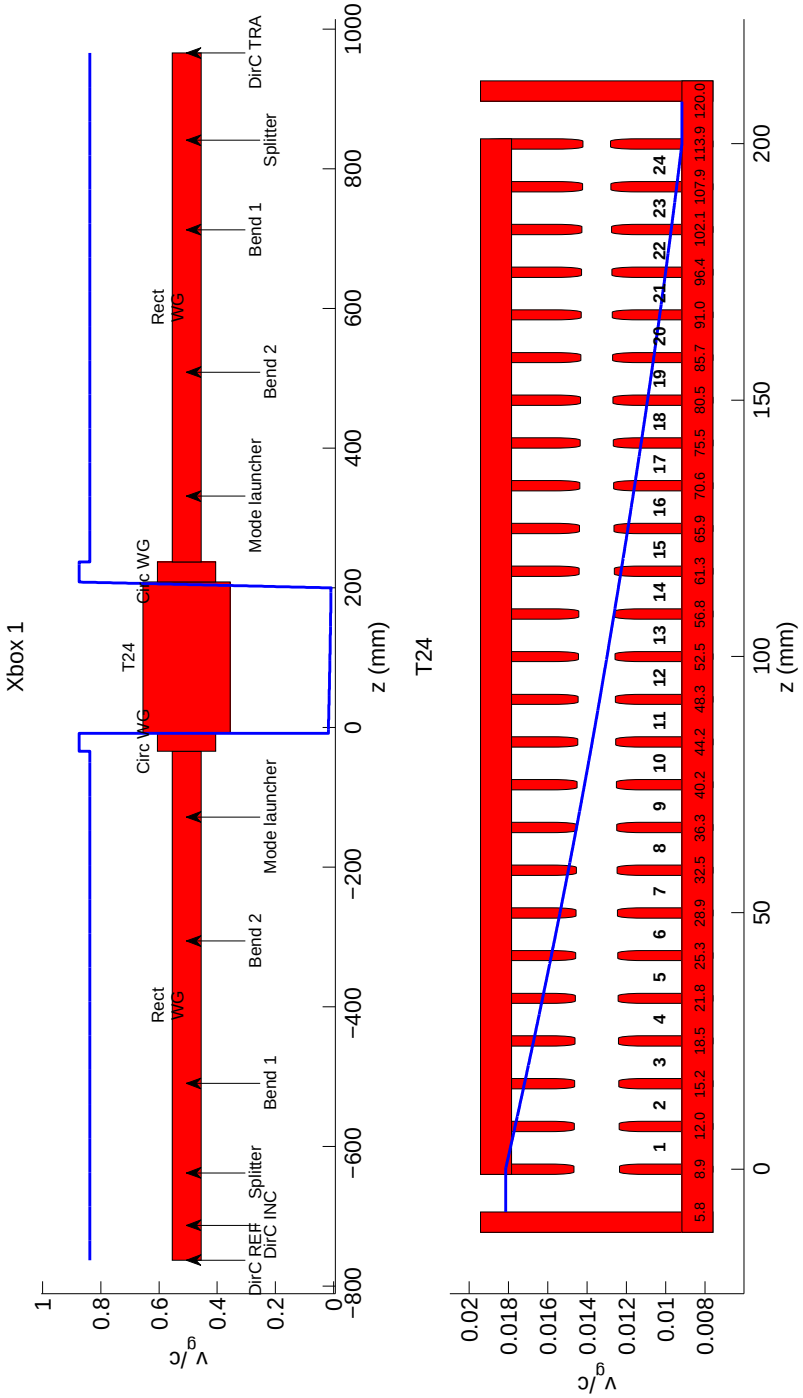

Figure 60: T24 group velocity profile.

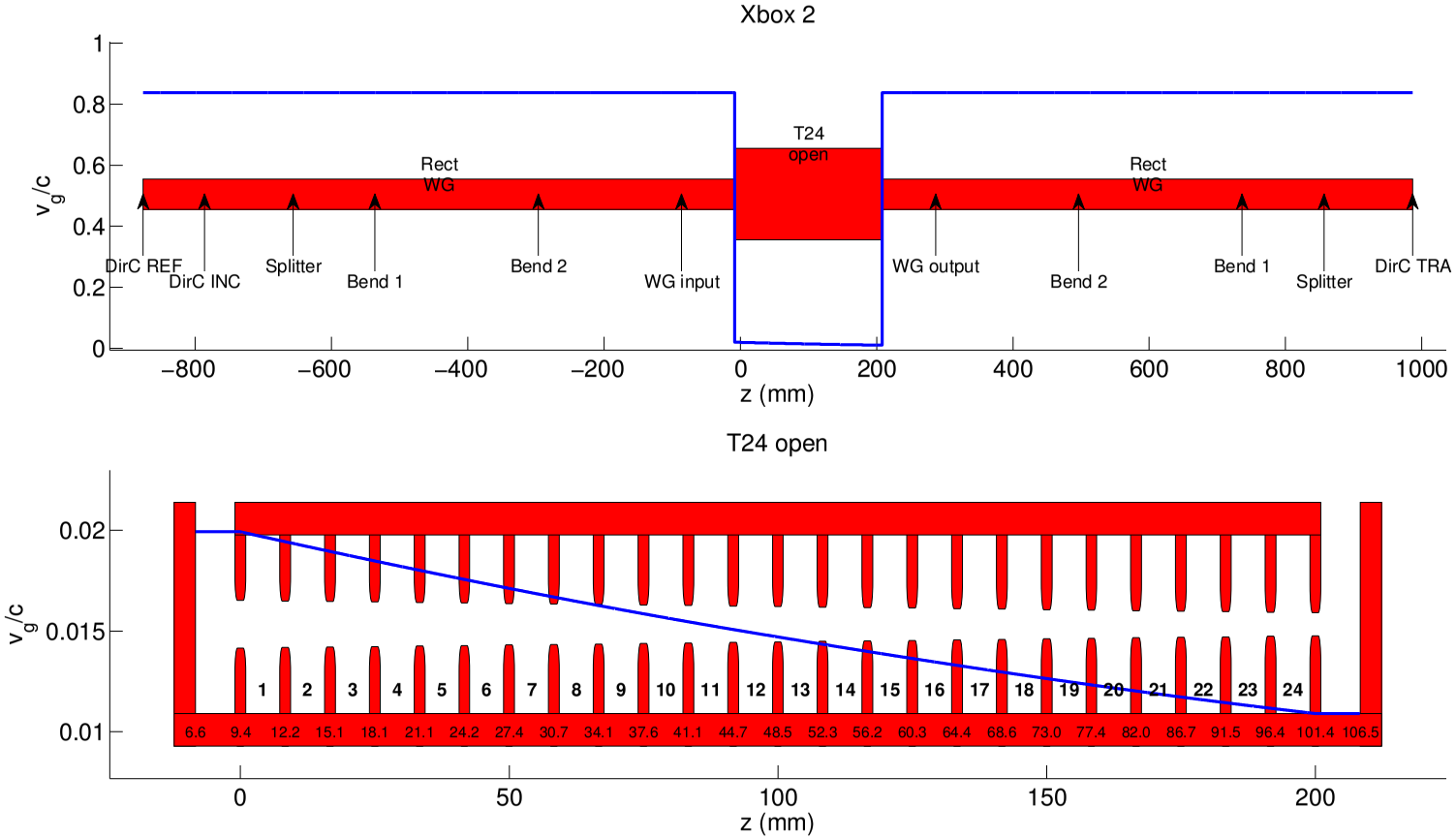

Figure 61: T24 open group velocity profile.

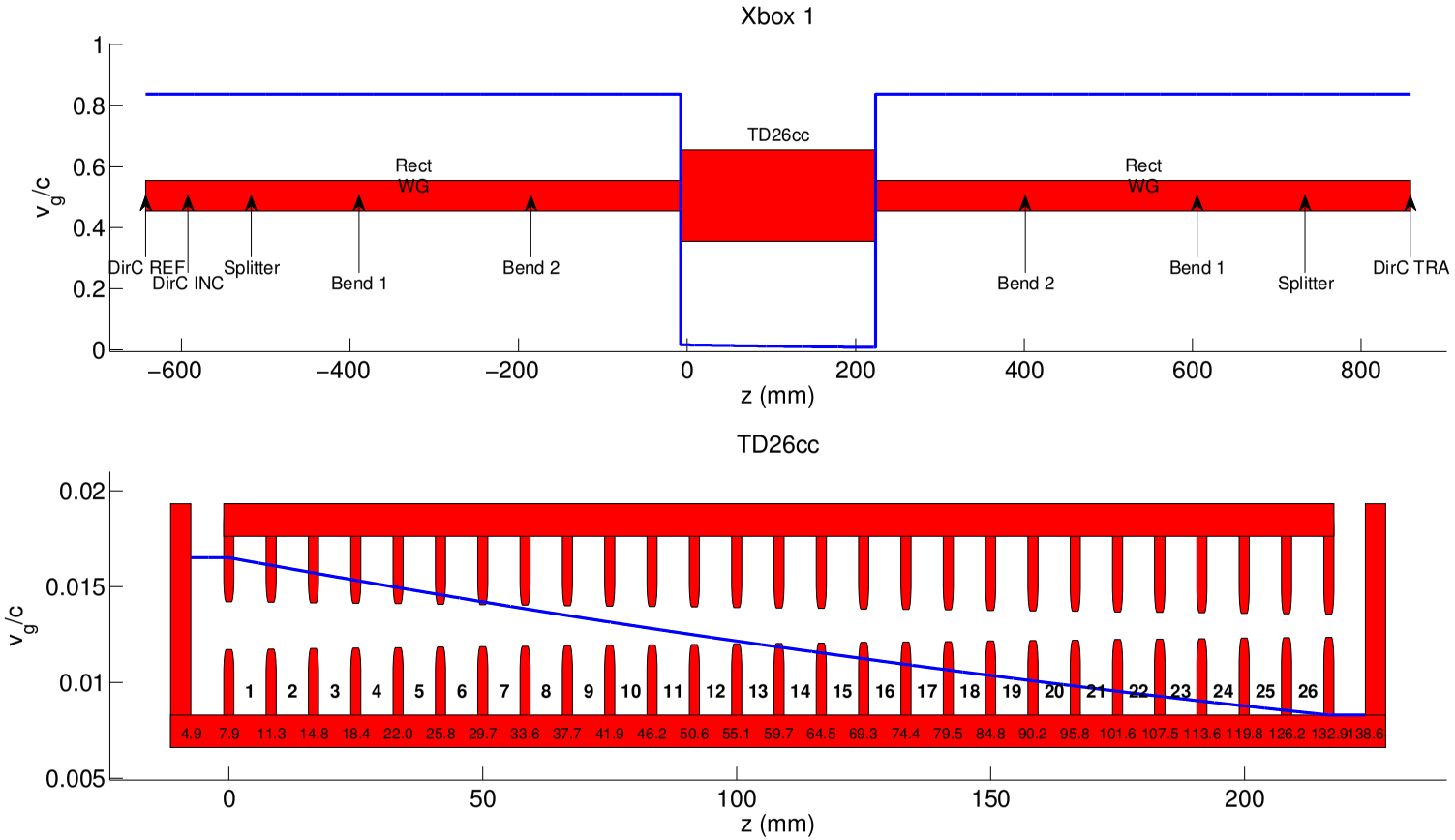

Figure 62: TD26CC group velocity profile.

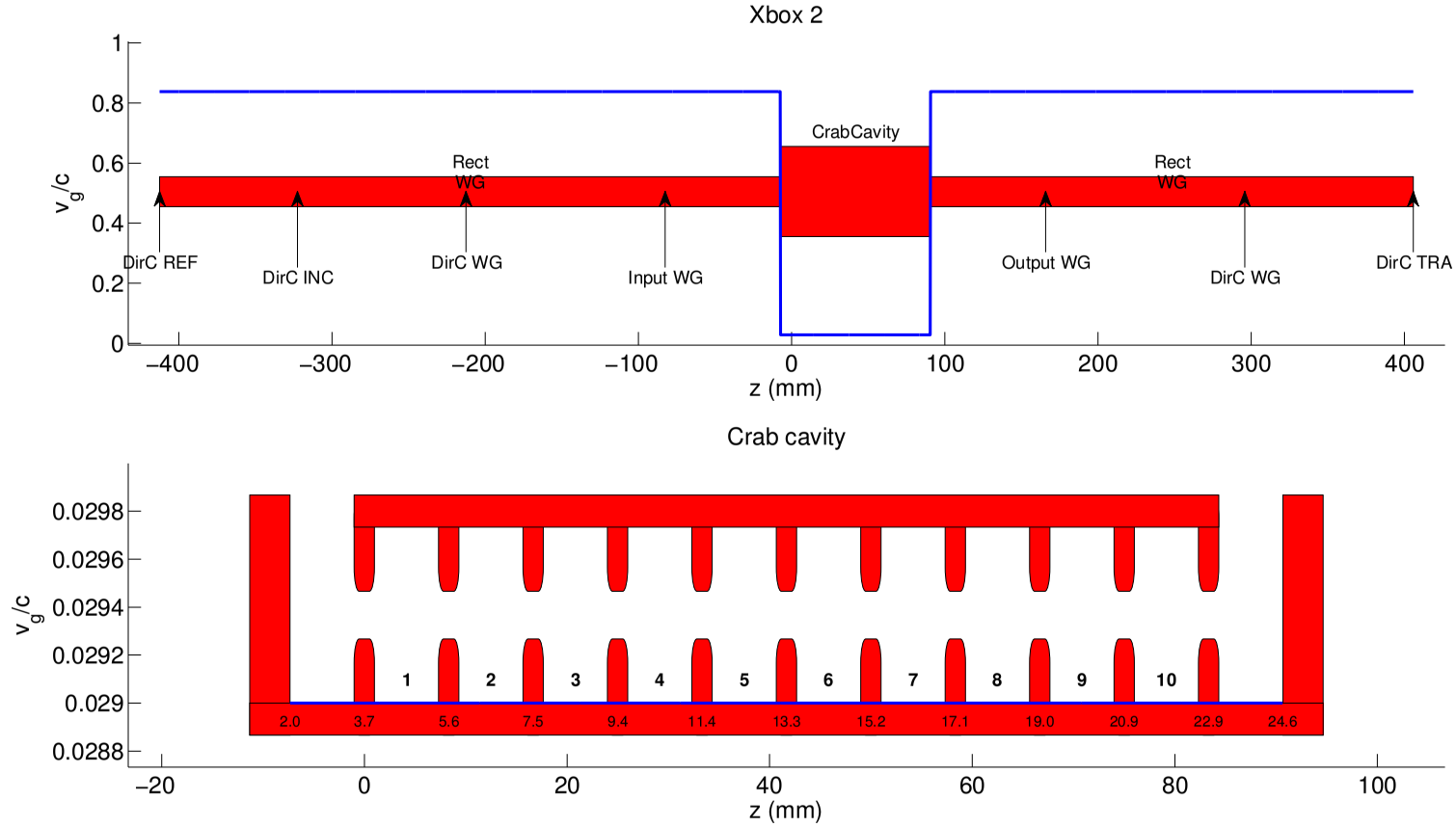

Figure 63: CLIC Crab Cavity group velocity profile.